



NRL/FR/6920--13-10,251

Functionalized Organosilicate Sorbents for Air Purification

BRANDY J. WHITE
BRIAN J. MELDE
MARTIN H. MOORE

*Laboratory for Biomolecular Dynamics
Center for Bio/Molecular Science and Engineering*

GREGORY W. PETERSON

*Edgewood Chemical Biological Center
Aberdeen Proving Grounds, MD*

December 23, 2013

Approved for public release; distribution is unlimited.

REPORT DOCUMENTATION PAGE				Form Approved OMB No. 0704-0188	
Public reporting burden for this collection of information is estimated to average 1 hour per response, including the time for reviewing instructions, searching existing data sources, gathering and maintaining the data needed, and completing and reviewing this collection of information. Send comments regarding this burden estimate or any other aspect of this collection of information, including suggestions for reducing this burden to Department of Defense, Washington Headquarters Services, Directorate for Information Operations and Reports (0704-0188), 1215 Jefferson Davis Highway, Suite 1204, Arlington, VA 22202-4302. Respondents should be aware that notwithstanding any other provision of law, no person shall be subject to any penalty for failing to comply with a collection of information if it does not display a currently valid OMB control number. PLEASE DO NOT RETURN YOUR FORM TO THE ABOVE ADDRESS.					
1. REPORT DATE (DD-MM-YYYY) 23-12-2013		2. REPORT TYPE Formal Report		3. DATES COVERED (From - To) June 1, 2009 to September 30, 2012	
4. TITLE AND SUBTITLE Functionalized Organosilicate Sorbents for Air Purification				5a. CONTRACT NUMBER	
				5b. GRANT NUMBER	
				5c. PROGRAM ELEMENT NUMBER	
6. AUTHOR(S) Brandy J. White, Brian J. Melde, Martin H. Moore, and Gregory W. Peterson*				5d. PROJECT NUMBER BA08PRO015	
				5e. TASK NUMBER	
				5f. WORK UNIT NUMBER 69-9634	
7. PERFORMING ORGANIZATION NAME(S) AND ADDRESS(ES) Naval Research Laboratory 4555 Overlook Avenue, SW Washington, DC 20375-5320 Edgewood Chemical Biological Center AMSRD-ECB-RT-PF Aberdeen Proving Grounds, MD 21010-5424				8. PERFORMING ORGANIZATION REPORT NUMBER NRL/FR/6920--13-10,251	
9. SPONSORING / MONITORING AGENCY NAME(S) AND ADDRESS(ES) Naval Research Laboratory 4555 Overlook Avenue, SW Washington, DC 20375-5320				10. SPONSOR / MONITOR'S ACRONYM(S) DTRA	
				11. SPONSOR / MONITOR'S REPORT NUMBER(S)	
12. DISTRIBUTION / AVAILABILITY STATEMENT Approved for public release; distribution is unlimited.					
13. SUPPLEMENTARY NOTES					
14. ABSTRACT A program was initiated in June 2009 to evaluate the potential of porous organosilicate sorbents in the capture or neutralization of light gas threats. Of primary interest were targets identified by the TIC/TIM Task Force as priority threats. A number of approaches were taken for increasing binding capacity and reactivity in the sorbent materials: grafting of metalloporphyrins, incorporation of sites for metal coordination, and incorporation of acidic and basic groups. In addition, the impact of morphological considerations, such as pore size and organization, were evaluated. Target capture by the sorbents was evaluated using microbreakthrough testing completed at the Edgewood Chemical Biological Center. Development of relevant sorbent morphologies was also pursued. Overall, the sorbents show promise, with several offering improvements in target capture and retention over state-of-the-art materials.					
15. SUBJECT TERMS Mesoporous Sorbent TIC TIM Reactive Catalytic Air purification Air filtration Porphyrin					
16. SECURITY CLASSIFICATION OF:			17. LIMITATION OF ABSTRACT SAR	18. NUMBER OF PAGES 67	19a. NAME OF RESPONSIBLE PERSON Brandy J. White
a. REPORT Unclassified	b. ABSTRACT Unclassified	c. THIS PAGE Unclassified			19b. TELEPHONE NUMBER (include area code) (202) 404-6100

CONTENTS

EXECUTIVE SUMMARY	E-1
INTRODUCTION	1
Background	1
Organosilicate Materials	1
Porphyrins	3
APPROACH	3
Material Synthesis and Grafting	4
Material Characterization	4
Microbreakthrough Screening	7
EXPERIMENTS	8
Phosgene	8
Simple Grafted Functionalities	15
Porphyrin Functionalized	21
Zirconium	36
Metal Incorporation	40
Physisorbed TEDA	46
Other Functionalizations	48
Scale-Up and Relevant Formats	50
CONCLUSIONS	56
ACKNOWLEDGMENTS	56
REFERENCES	56

FIGURES

Fig. 1	PMO synthesis	2
Fig. 2	Porphyrins	3
Fig. 3	Characterization of EA5	9
Fig. 4	Phosgene breakthrough on sorbent columns	10
Fig. 5	Chloride recovery	10
Fig. 6	Reusability	11
Fig. 7	Low fluorescence materials	12
Fig. 8	Fluorescence response to phosgene	12
Fig. 9	Fluorescence response to phosgene	13
Fig. 10	Lifecycle	14
Fig. 11	Material characteristics for E50, E50A, and E50I	16
Fig. 12	Ammonia breakthrough for E50 sorbents	16

Fig. 13	Water binding isotherms for E50 sorbents	17
Fig. 14	Cyanogen chloride breakthrough for E50 sorbents	18
Fig. 15	Sulfur dioxide breakthrough for E50 sorbents	19
Fig. 16	Octane breakthrough for E50 sorbents	20
Fig. 17	Chlorine breakthrough for E50 sorbents	20
Fig. 18	Fluorescence quenching	22
Fig. 19	Material characteristics for porphyrin functionalized sorbents	23
Fig. 20	Material characteristics for porphyrin functionalized sorbents	23
Fig. 21	Ammonia breakthrough for the Cu DIX materials	24
Fig. 22	Ammonia breakthrough for the Cu C ₄ TPP materials	26
Fig. 23	Ammonia breakthrough for the Cu N ₄ TPP materials	26
Fig. 24	Ammonia breakthrough for the Co C ₁ TPP material	27
Fig. 25	Fluorescence of Cu DIX sorbents	28
Fig. 26	Fluorescence of Cu C ₄ TPP sorbents	29
Fig. 27	Fluorescence of Cu N ₄ TPP sorbents	29
Fig. 28	Fluorescence of sorbents exposed to sulfur dioxide	31
Fig. 29	Fluorescence of sorbents exposed to octane	32
Fig. 30	Chlorine and nitric oxide breakthrough	32
Fig. 31	Morphological characteristics for EB and EC sorbents	33
Fig. 32	Target breakthrough for EB and EC sorbents	34
Fig. 33	Chlorine breakthrough for NiC1S3-ED13	35
Fig. 34	Target breakthrough for NiC1S3-ED13	35
Fig. 35	Target breakthrough for NiC1S3-ED13	36
Fig. 36	Morphological characteristics of Zr materials	37
Fig. 37	Target breakthrough for Zr materials	39
Fig. 38	Target breakthrough for Zr materials	39
Fig. 39	Material characteristics for EDA and AEA sorbents	41
Fig. 40	Target breakthrough for sorbents with hydroxyl associated metals	43
Fig. 41	Target breakthrough for sorbents with hydroxyl associated metals	43
Fig. 42	Ammonia breakthrough for EDA and AEA sorbents	44
Fig. 43	Cyanogen chloride breakthrough for EDA and AEA sorbents	45
Fig. 44	Sulfur dioxide breakthrough for EDA and AEA sorbents	45
Fig. 45	Target breakthrough for TEDA functionalized sorbents	47
Fig. 46	Target breakthrough for TEDA functionalized sorbents	48
Fig. 47	Chlorine breakthrough for E50 and E50-TEDA sorbents	48
Fig. 48	Morphological characteristics for ADC-10 and CAR-40	49
Fig. 49	Morphological characteristics for thin film	51
Fig. 50	Absorbance and fluorescence of thin film	51
Fig. 51	Morphological characteristics for coated fabric	52
Fig. 52	Performance of functionalized coated fabric	52
Fig. 53	Water vapor permeation through fabrics	53
Fig. 54	Target vapor permeation through fabrics	54
Fig. 55	Photographs of sorbent monoliths	54
Fig. 56	Morphological characteristics for pressed pellets	55

TABLES

Table 1	Synthesis Reagents	5
Table 2	Sorbent Materials and Morphological Characteristics.....	6
Table 3	Capture of Phosgene by DIX Sorbent Columns	9
Table 4	Calculated Target Loading Capacities – Ammonia and Cyanogen Chloride	17
Table 5	Calculated Target Loading Capacities – Sulfur Dioxide and Octane	19
Table 6	Summary of Reagent Combinations Used for Synthesis.....	22
Table 7	Calculated Ammonia Loading Capacities	25
Table 8	Calculated Target Loading Capacities – Cyanogen Chloride, Sulfur Dioxide, and Octane	30
Table 9	Calculated Target Loading Capacities – Chlorine and Nitric Oxide	33
Table 10	Target Loading Capacities for Zirconium Materials	38
Table 11	Calculated Target Loading Capacities for Metal Modified Materials	42
Table 12	Calculated Octane Loading Capacities for Metal Reflux Materials	44
Table 13	Calculated Target Loading Capacities for TEDA Functionalized Sorbents* – Ammonia and Cyanogen Chloride	46
Table 14	Calculated Target Loading Capacities for TEDA Functionalized Sorbents – Sulfur Dioxide, Octane, and Chlorine	47
Table 15	Morphological Characteristics for Sorbent Materials Pressed into Pellets	55

EXECUTIVE SUMMARY

The Center for Bio/Molecular Science and Engineering at the Naval Research Laboratory (NRL) initiated a program in December 2008 for development of porous organosilicate materials directed at providing self-decontaminating fabrics and surfaces with funding through the Defense Threat Reduction Agency (DTRA, BA08PRO015). In June 2009, the effort was expanded to include development of materials for reactive or catalytic air purification. This report details the materials developed under that effort. Material development was directed at providing sorbents for capture of phosgene, ammonia, octane, sulfur dioxide, and cyanogen chloride. In addition, the potential for application of porphyrin functionalized sorbents to sensing, especially as pertains to residual life indication, was evaluated.

The sorbents described here are based on organosilicate scaffolds that are either mesoporous or offer a hierarchical materials structure. A number of approaches were taken for increasing the binding capacity and reactivity in the sorbent materials: grafting of metalloporphyrins, incorporation of sites for metal coordination, and incorporation of acidic and basic groups. In addition, the impact of morphological considerations, such as pore size and organization, was also evaluated. Target capture by the sorbents was evaluated using microbreakthrough testing completed by the CBR filtration branch of Edgewood Chemical Biological Center, Aberdeen Proving Grounds, MD. Development of relevant sorbent morphologies for applications was also pursued. Solid surface and fabric modification methods are described. The generation of larger pellets of the powdered sorbents is also discussed. Overall, the sorbents show promise with several offering improvements in target capture and retention over state-of-the-art materials.

FUNCTIONALIZED ORGANOSILICATE SORBENTS FOR AIR PURIFICATION

INTRODUCTION

The Center for Biomolecular Science and Engineering at the Naval Research Laboratory (NRL) initiated a program in December 2008 for development of porous organosilicate materials directed at providing self-decontaminating fabrics and surfaces. In June 2009, the effort was expanded to include development of materials for reactive or catalytic air purification. The effort detailed here describes materials development directed at providing sorbents for capture of phosgene, ammonia, octane, sulfur dioxide, and cyanogen chloride. In addition, the potential for application of porphyrin functionalized sorbents to sensing, especially as pertains to residual life indication, is detailed.

The sorbents described here are based on organosilicate scaffolds that are either mesoporous or offer a hierarchical materials structure. A number of approaches were taken for increasing the binding capacity and reactivity of the sorbent materials. Grafting of metalloporphyrins was investigated as a result of the known catalytic properties of those compounds. Sites were incorporated for metal coordination. Acidic and basic groups were incorporated. The hydrophobic/hydrophilic properties of the sorbents were altered. The impact of morphological considerations, such as pore size and organization, was also evaluated. Several materials were developed that provide improvements over state-of-the-art materials in capture and retention of one or more of the selected targets.

Background

Targets for this effort were selected based on the Toxic Industrial Chemical/Toxic Industrial Material (TIC/TIM) Task Force MFR#1 published in February 2009. The document focuses on inhalation hazards in an operational environment and provides a list of compounds prioritized based on toxic hazard and the likelihood of an encounter [1]. Cartridge-based air purifying respirators are used to protect the warfighter against chemical exposure. Traditional air purification materials often rely on porous carbons such as activated carbon or activated charcoal [2]. Through modification of these types of carbon materials, functional moieties can be combined with high surface area and adsorptive properties to provide air purification materials with improved characteristics or novel function [3,4]. Ongoing efforts seek to improve the performance of carbon materials in air purification applications as well as to provide alternatives to these materials [5-9]. Improvements such as active residual life indication and regenerable or catalytic cartridge materials are of ongoing interest.

Organosilicate Materials

Porous organosilicates have been used in a wide range of applications from catalysis to sensing [10-12]. The materials can be synthesized with ordered or disordered pore conformations. Surface areas of up to 1,000 m²/g are possible with average pore diameters from 28 to 120 Å [13,14]. These materials are synthesized using surfactant-templating during condensation of polysilsesquioxane precursors (Fig. 1) [15]. Structural rigidity in the materials is provided by the silica component. Target interaction characteristics can result from the organic groups of the precursors or can be incorporated through post-

synthesis modification of the sorbents. Modification of the synthetic procedures produces variations in the morphological characteristics of the materials. It is possible, for example, to synthesize sorbents combining controlled mesoporosity (2 to 80 nm) with macroscale texture (>50 nm) to improve access to the mesopore volume [16-18]. The macropores provide improved flow through the sorbents and enhanced access to the mesopore volume, which is advantageous to diffusion dependent applications. The high surface area and a large interconnected pore volume of mesoporous organosilicates offer an ideal scaffold for immobilization of porphyrins and other functional moieties. These materials have been used in a wide range of catalysis and sensing applications [10-12], including in the capture and detection of gases [19-25].

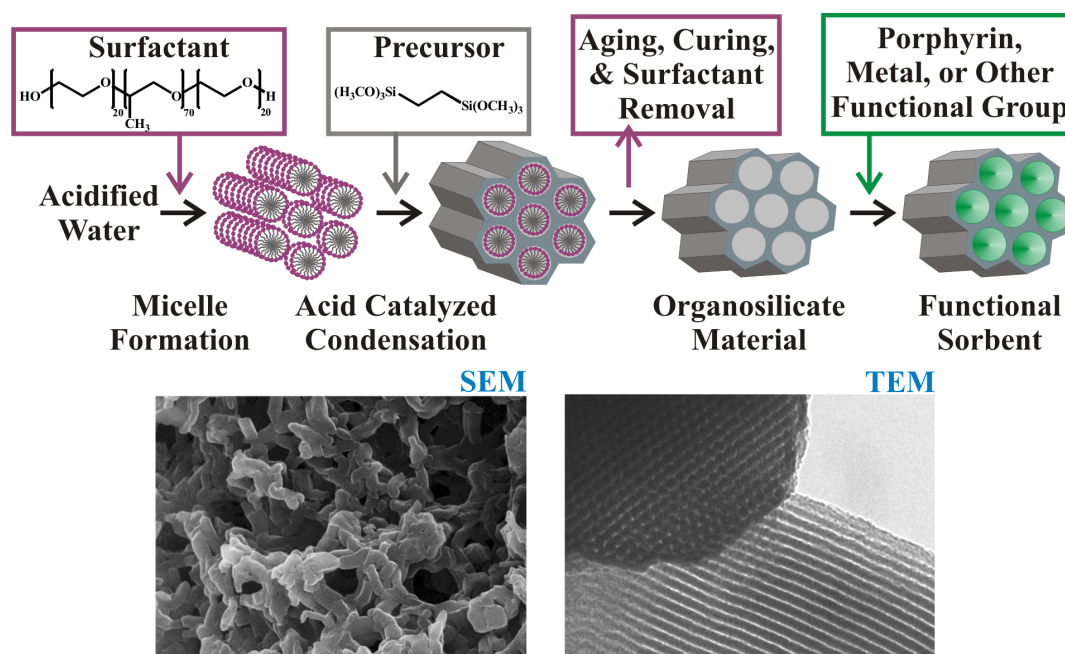


Fig. 1 – Synthesis and morphology. Conditions are established to produce the formation of micelles of surfactant molecules (for example, the Pluronic P123 shown here). Siloxane precursors, which have alternating organic and silicate groups, are then added to the solution. The surfactant micelles act as a template during condensation of precursors; the organized pore system is retained when the surfactant is removed. Phase separation during condensation can lead to the formation of large features ($\sim 1 \mu\text{m}$; SEM) in addition to the mesopores (TEM). Porphyrins and other functionality can also be added following sorbent synthesis.

We have previously reported on our efforts directed at optimizing the characteristics of organosilicate materials for capture of nitroenergetic [26,27], hydrocarbon [28], and organophosphate targets [29]. Those efforts focused on the development of a scaffold with high binding capacity and selectivity for the targets through alteration of the bridging groups comprising the pore walls. Here, we have taken two approaches. For many of the sorbents, simple scaffolds were used and alterations to the characteristics of the scaffolds were achieved through post-synthesis modification. For small pendant functional groups, co-condensation approaches have also been used. While organic functionalities can be incorporated in high amounts by one-step co-condensation of silanes during synthesis, this can significantly affect the final pore structure of a product [10]. Post-synthesis grafting also increases the likelihood that pendant functional groups are located on the surface.

Porphyrins

Porphyrins offer spectrophotometric and interaction characteristics that may provide advantages to these applications. Varying the coordinated metal ion or the molecular structure of the porphyrin (Fig. 2) has been shown to significantly impact the sensitivity of spectrophotometric characteristics to the presence of ammonia, for example, as well as the reversibility of the response [30-32]. Evidence of the potential for photoreactivity between a metalloporphyrin and a light gas target has been demonstrated with nitrogen dioxide [33,34].

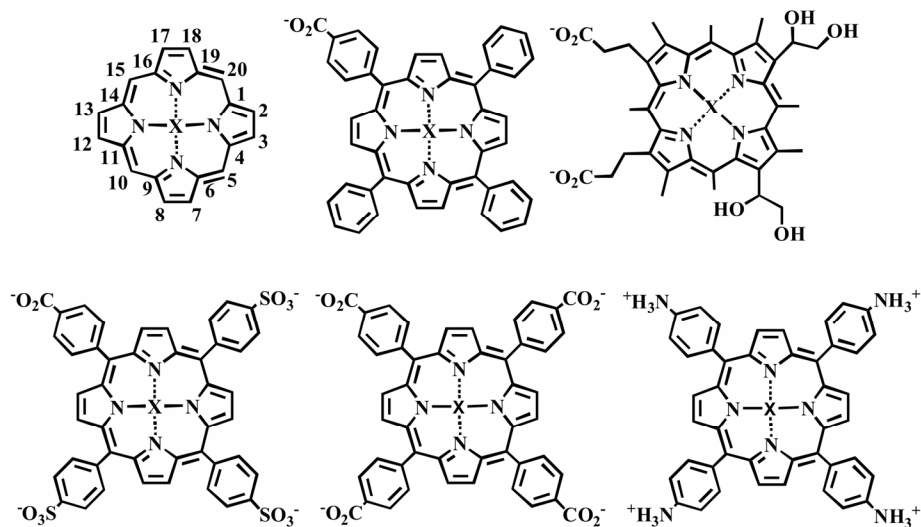


Fig. 2 – Structures of the porphyrin parent compound and those porphyrins used in the presented studies: top from left to right: porphine, 5-mono(4-carboxyphenyl)-10, 15, 20-triphenyl porphyrin (C_1 TPP); Deuterioporphyrin IX 2,4 bis-ethylene glycol (DIX); bottom from left to right: meso-tri(4-sulfonatophenyl)mono(4-carboxyphenyl) porphyrin (C_1S_3 TPP); meso-tetra(4-carboxyphenyl) porphyrin (C_4 TPP); and meso-tetra(4-aminophenyl) porphyrin (N_4 TPP).

We have previously reported on our efforts directed at combining the materials characteristics provided by organosilicate scaffolds with the optical and catalytic properties of porphyrins [28,29,32,35]. For larger targets in aqueous solutions, the scaffold provided high binding capacity and selectivity for the targets [28,29,35]. For light gases, we used the scaffold as purely that and incorporated binding sites through grafting onto the scaffold surface [32,36,37]. In air filtration applications, the porphyrins provide binding capacity and affinity, and the spectrophotometric characteristics offer the potential for residual life indication. In addition, the catalytic activity of the porphyrins may provide avenues for extending the functional lifetime of a sorbent bed.

APPROACH

Deuterioporphyrin IX 2,4 bis-ethylene glycol (DIX), 5-mono(4-carboxyphenyl)-10, 15, 20-triphenyl porphyrin (C_1 TPP), meso-tetra(4-carboxyphenyl) porphyrin (C_4 TPP), meso-tetra(4-aminophenyl) porphyrin (N_4 TPP), and meso-tri(4-sulfonatophenyl)mono(4-carboxyphenyl) porphyrin (C_1S_3 TPP) were obtained from Frontier Scientific, Logan, UT (Fig. 1). Triethylenediamine (TEDA; DABCO), copper (II) chloride, cobalt (II) acetate, magnesium chloride hexahydrate, europium (II) chloride, iron (II) chloride, zinc chloride, nickel (II) chloride, tryptamine, and phosgene (20% in toluene) were purchased from Sigma-

Aldrich (St. Louis, MO). Chemicals were used as received. Water was deionized to 18.2 M Ω cm using a Millipore Milli-Q UV-Plus water purification system.

Material Synthesis and Grafting

Different materials syntheses result in sorbents with varied characteristics [27,29,32,37-39]. Several variations were used in an attempt to provide improved capture across the spectrum of targets considered. In many of the sorbents, an ethane bridged scaffold is used for support of functional groups. The sorbent E50 is an example of this type of material. Functional groups were incorporated through post-synthesis grafting or through co-condensation. This type of material was also used to support porphyrins and metalloporphyrins for additional functionality. Other materials incorporated metal chelating groups into the sorbent structure to provide sites for interaction with light gas targets, for example, ethylenediamine. Zirconium particles were incorporated into sorbents based on previous descriptions of their application to removal of sulfur dioxide [40]. Larger more hydrophobic groups were also considered as was the impact of physisorbed functionalities (see MM3). Table 1 summarizes the reagents used and provides the abbreviations adopted throughout this document. Table 2 summarizes the types of materials and associated morphological characteristics. The specifics of materials synthesis are provided in the sections describing their development and application.

Activated Carbon Sorbent

A carbon sorbent was selected for use as a benchmark for comparison of materials developed under this study and those developed by related efforts. BPL activated carbon (12 \times 30 mesh) impregnated with 5% (nominal) zinc oxide by weight was provided by Calgon Carbon Corporation. Triethylenediamine (TEDA; DABCO, Aldrich Chemical Company) was added to the carbon (3%, nominal) in a large vial (BPL/Zn/TEDA). The vial was placed on a rotating mixer and equilibrated for 2 days at room temperature, allowing the TEDA to sublime into the pores of BPL carbon. The resulting material was pulverized to a powder before breakthrough testing to reduce bulk mass transfer effects.

Material Characterization

A Micromeritics ASAP 2010 was used for N₂ sorption experiments performed at 77 K. Prior to analysis, samples were degassed to 1 μ m Hg at 100 °C. Standard methods were applied to the calculation of characteristics. Surface area was determined by use of the Brunauer-Emmett-Teller (BET) method; pore size was calculated by the Barrett-Joyner-Halenda (BJH) method from the adsorption branch of the isotherm; total pore volume was calculated by the single point method at relative pressure (P/P₀) 0.97. Morphological characteristics for the materials are summarized in Table 2. Thermogravimetric analysis was performed using a TA Instruments Hi-Res 2950 Thermogravimetric Analyzer under a N₂ atmosphere; temperature was ramped 5 °C/min to 800 °C. Powder X-ray diffraction patterns were obtained with one of two systems: (1) a Rigaku high-resolution powder diffractometer with 18 kW CuK α radiation derived from a high-power Rigaku rotating anode X-ray generator or (2) CuK α radiation from a Brüker MICROSTAR-H X-ray generator operated at 40 kV and 30 mA equipped with a 3 mRadian collimator, and a Brüker Platinum-135 CCD area detector (room temperature). A custom fabricated beamstop was mounted on the detector to allow data collection to approximately 0.4° 2 θ (approximately 210 Å) with a sample to detector distance of 30 cm. After unwarping the images, the XRD² plug-in was used to integrate the diffraction patterns from 0.6° to 8° 2 θ .

Table 1 — Synthesis Reagents

Compound	Abbrev	Supplier	Function	Notes
Bis(trimethoxysilyl)ethylbenzene	DEB	Gelest	Precursor	95%
1,2-bis(trimethoxysilyl)ethane	BTE	Gelest	Precursor	
(3-aminopropyl)triethoxysilane	APS	Gelest	Precursor	>98%
3-isocyanatopropyltriethoxysilane	ICS	Gelest	Precursor	
N,N'-bis[3-(trimethoxysilyl)propyl]ethylenediamine	EDA	Gelest	Precursor	
N-2-(aminoethyl)-3-aminopropyltrimethoxysilane	AEA	Gelest	Precursor	
Carboxyethylsilanetriol	CES	Gelest	Precursor	
Hydrochloric acid	HCl	Sigma-Aldrich	Solvent System	37%
Polyoxyethylene (10) stearyl ether, C ₁₈ H ₃₇ (OCH ₂ CH ₂) _n OH, n~10	Brij®76	Sigma-Aldrich	Surfactant	
Diethyl chlorophosphate		Sigma-Aldrich	Target Analog	
Dichloromethane		Sigma-Aldrich	Template Synthesis	Solvent >99.5%
Sodium bicarbonate	NaHCO ₃	Sigma-Aldrich	Template Synthesis	Purification
Magnesium turnings		Sigma-Aldrich	Phase Separation	98%
Tetramethyl orthosilicate	TMOS	Sigma-Aldrich	Precursor	98%
Tetraethyl orthosilicate	TEOS	Sigma-Aldrich	Precursor	
Zirconium n-propoxide		Sigma-Aldrich	Precursor	
Toluene		Sigma-Aldrich	Grafting	Solvent
1,3,5-trimethylbenzene	TMB	Sigma-Aldrich	Spinodal Decomposition	Mesitylene
Poly(ethylene glycol)- <i>block</i> -poly(propylene glycol)- <i>block</i> -poly(ethylene glycol) average M _n ~5800	P123	BASF	Surfactant	Pluronic P123
Ethylene oxide/propylene oxide block copolymer	F127	BASF	Surfactant	Pluronic F127
Cetyltrimethylammonium chloride	CTAB	Sigma	Surfactant	99%
Nitric acid	HNO ₃	Sigma-Aldrich	Solvent System	70%
Ethanol		Warner-Graham	Solvent System	200 proof
Methanol		Sigma-Aldrich	Solvent System	ChromaSolv
1-ethyl-3-[3-dimethylaminopropyl]carbodiimide	EDC	Pierce	Coupling Chemistry	
2-(N-morpholino)ethanesulfonic acid	MES	Sigma	Coupling Buffer	100 mM, pH 6.0
1,3-acetonedicarboxylic acid	ACA	Sigma	Dicarbonyl groups	

Table 2 — Sorbent Materials and Morphological Characteristics

Abbreviation	Description	Surface Area (m ² /g)	Pore Volume (cm ³ /g)	Pore Diameter (Å)
EA5	Co-condensed ethyl bridging and amine pendant groups (0.2 mmol/g)	1,012	1.19	79
DIX-EA5	DIX functionalized EA5 (including metal variants: Co, Cu, Fe, Zn, Eu, Mg)	1,001	1.00	82
E50	Ethane bridged scaffold	1,096	1.04	81*
E50A	E50 with grafted pendant amine groups (2 mmol/g)	637	0.87	81*
E50I	E50 with grafted pendant isocyanate groups (2 mmol/g)	1,012	1.12	81*
EA2	Co-condensed ethyl bridging and amine pendant groups (0.1 mmol/g)	791	1.01	75
EA2-CuC	EA2 with Cu C ₄ TPP porphyrin	804	1.02	66
EA5-CuD	DIX-EA5 with copper	1,002	1.19	79
EA5-CoC1	Co C ₁ TPP functionalized EA5	1,008	1.05	80
E50A-CuD	E50A with Cu DIX porphyrin	723	0.72	76*
E50A1-CuD	E50 with grafted pendant amine groups (0.5 mmol/g) and Cu DIX porphyrin	890	0.83	68
E50A5-CuD	E50 with grafted pendant amine groups (5 mmol/g) and Cu DIX porphyrin	800	0.76	76
E50A5-CuC	E50 with grafted pendant amine groups (5 mmol/g) and Cu C ₄ TPP porphyrin	726	0.82	78
E50A10-CuC	E50 with grafted pendant amine groups (10 mmol/g) and Cu C ₄ TPP porphyrin	719	0.82	76
E50I-CuN	E50I with Cu N ₃ TPP porphyrin	1,031	1.00	70
E50I5-CuN	E50 with grafted pendant isocyanate groups (5 mmol/g) and Cu N ₃ TPP porphyrin	1,019	1.02	77
E50-I10-CuN	E50 with grafted pendant isocyanate groups (10 mmol/g) and Cu N ₃ TPP porphyrin	1,069	1.23	65
EB-Cu2D	Similar to EA2 with Cu(II) DIX porphyrin	1,080	0.92	76
EB-Cu1D	Similar to EA2 with Cu(I) DIX porphyrin	1,071	1.04	75
EC-Cu2D	Similar to EA2 with Cu(II) DIX porphyrin	925	0.72	60
EC-Cu1D	Similar to EA2 with Cu(I) DIX porphyrin	925	0.72	60
NiC1S3-ED13	50:50 diethylbenzene:ethane bridged scaffold with 1 g/g APS graft and Ni C ₁ S ₃ TPP porphyrin	307	0.33	79
ZrMP4-A	Zr-MP4 treated with sulfuric acid	480	0.70	56
ZrMP4	Zr on hierarchical silica	520	0.37	31
ZrM41-A	ZrM41 treated with sulfuric acid	624	0.72	28
ZrM41	Zr on MCM-41 type material	623	0.625	28
Co E50	E50 refluxed in CoCl ₂	1,007	1.08	76
Cu E50	E50 refluxed in CuCl ₂	1,007	1.08	76
Mg E50	E50 refluxed in MgCl ₂	1,007	1.08	76
CuEDA(3)	Cu EDA sorbent using 3 g HCl	512	0.47	50*

Table 2 — Sorbent Materials and Morphological Characteristics, continued

CuEDA(4)	Cu EDA sorbent using 4 g HCl	564	0.75	50*
CuAEA(3)	Cu AEA sorbent using 3 g HCl	590	0.59	92
CuAEA(4)	Cu AEA sorbent using 4 g HCl	716	0.87	64
ZnEDA(2)	Zn EDA sorbent using 2 g HCl	190	0.41	181
ZnEDA(4)	Zn EDA sorbent using 4 g HCl	716	0.87	64
ZnAEA(2)	Zn AEA sorbent using 2 g HCl	275	0.70	223
ZnAEA(4)	Zn AEA sorbent using 4 g HCl	294	0.71	250*
MM3	50:50 diethylbenzene:ethane bridged scaffold	324	0.39	47
E50-TEDA	E50 with physisorbed TEDA	1,096	1.04	81*
MM3-TEDA	MM3 with physisorbed TEDA	324	0.39	47
CAR-40	Silicate with pendant carboxyl groups	487	0.53	55
ADC-10	Silicate modified with acetonedicarboxylic acid	310	0.53	75

*Indicates broad pore size distribution

Conducting carbon tape was used to mount samples on scanning electron microscopy (SEM) stubs for imaging by SEM. Sputter coating with gold under argon was accomplished using a Cressington 108 auto-sputter coater for (duration 60 s). Scanning electron micrographs of the samples were collected using a LEO 1455 SEM (Carl Zeiss SMT, Inc., Peabody, MA). For imaging via transmission electron microscopy (TEM), samples were deposited onto a holey carbon grid (200 mesh copper, SPI, West Chester, PA) and viewed under an energy filtering transmission electron microscope (LIBRA 120 EFTEM, Carl Zeiss SMT, Peabody, MA) operated at 120 kV. Zero Loss, brightfield, energy filtered (EF) TEM images were captured on a bottom-mounted digital camera (KeenView, Olympus SIS, Montvale, NJ).

Microbreakthrough Screening

Organosilicate materials were evaluated as powders in a microbreakthrough apparatus that has been described elsewhere [41]. Sorbent volume was fixed at 55 mm³ with masses ranging from 4 to 22 mg. Experiments were conducted at 20 °C with 0% (-40 °C T_{dp}) or 80% relative humidity. The sorbents pre-equilibrated for 2 h under those conditions. Target flow rate was fixed at 20 mL/min. Materials were evaluated with ammonia, cyanogen chloride, octane, and sulfur dioxide. Ammonia (NH₃, 1,000 mg/m³) is a basic/base-forming target. Cyanogen chloride (CNCl, 4,000 mg/m³) and sulfur dioxide (SO₂, 1,000 mg/m³) are acidic/acid-forming targets. Octane (4,000 mg/m³) is used to probe materials for physical adsorption capacity and retention.

The packed sorbent tube was submerged in a temperature-controlled water bath set to 20 °C. For ammonia, cyanogen chloride (CK), and sulfur dioxide tests, a ballast containing a known mass of gas was charged with air to create a pressurized, concentrated reservoir. In the case of octane, a saturator cell was used with an air stream sweeping across liquid octane, creating a saturated vapor. The target stream was mixed with either dry or humid air to achieve the required challenge concentration at the desired relative humidity. The mixed stream was pushed through the packed bed, and the effluent was monitored using a photoionization detector (PID) equipped with a 10.6 eV lamp for ammonia, a flame ionization detector (FID) for cyanogen chloride and octane, and a flame photometric detector (FPD) equipped with a sulfur

lens for sulfur dioxide. Results are plotted on a weighted basis to account for differences in material density.

Breakthrough curves were integrated to saturation for calculation of saturated loading levels. Calculation of the dynamic sorption capacity, or loading, of the materials based on microbreakthrough data has been described previously [5]. In general, the integral of the breakthrough curve is subtracted from the integral of the challenge profile yielding the amount of target adsorbed, the difference. The sorption capacity to saturation was calculated using the integral of the breakthrough curve to the point where the effluent concentration equaled the feed concentration. To provide an indication of how strongly chemicals are adsorbed on the materials, the effective loading was calculated through consideration of the integral of the desorbed target during purge of the column.

EXPERIMENTS

The types of targets selected for this effort cover a range of light gases and include different threats such as acid forming or base forming targets. The material presented here is divided on the basis of the type of sorbent used and further divided by target type. Phosgene is handled separately as different testing protocols were used for that target.

Phosgene

Phosgene is well-known as a chemical warfare agent, but it is also used in industrial and pharmaceutical processes. It was identified as a potential threat in the list of ocular and inhalation hazards [1]. The wide availability of phosgene results in a greater threat than that presented by several of the higher toxicity compounds on the list. The chlorinated structure of the compound also provides the potential for its use as a representative of the blister agent family. As phosgene interacts with humidity in the air, hydrochloric acid is evolved. Adsorption technologies are sought to capture not only the primary threat, but to reduce or eliminate the threat of these types of secondary compounds.

Material Synthesis

These studies focused on application of an amine functionalized ethane bridged sorbent. The material was synthesized by a common preparation method using Pluronic P123 in acidic media [17,37]. Pluronic P123 (1.9 g) and TMB (0.3 g) were dissolved in 0.1 M HNO₃ (9.5 g) with stirring at 60 °C. When the solution had cooled to room temperature, a precursor mixture of 2.12 g BTE and 0.025 g APS was added drop-wise. The reaction mixture was stirred until homogeneous and heated in a sealed tube overnight at 60 °C. The tube was unsealed and heated at 60 °C for 2 d, and then 80 °C for 2 d. The product in the form of a white monolith was refluxed three times in 1 M HCl in ethanol for at least 12 h to extract the surfactant. The powder was collected by suction filtration, rinsed with ethanol and water, and dried at 110 °C. Nitrogen adsorption/desorption isotherms and pore size distributions for EA5 are presented in Fig. 3 [32,36]. Prior to metalloporphyrin functionalization, the amine-functionalized material had a surface area of 1,012 m²/g, a pore volume of 1.19 cm³/g, and an average pore diameter of 79 Å. Metalloporphyrin functionalization resulted in a surface area of 1,001 m²/g, a pore volume of 1.00 cm³/g, and an average pore diameter of 82 Å.

Porphyrin incorporation (DIX) into the amine-functionalized sorbent was accomplished using 1-ethyl-3-[3-dimethylaminopropyl]carbodiimide (EDC) coupling chemistry. The organosilicate material (1 g) was placed in a solution of 5 mM EDC and 0.6 mM porphyrin in 100 mM MES buffer (2-(*N*-morpholino)ethanesulfonic acid; total volume 50 mL). The solution was incubated overnight with agitation and collected by vacuum filtration. It was then rinsed with ethanol and water. Metals were incorporated into the porphyrin-functionalized material by refluxing the sorbent in a solution of 1 mM

metal salt in deionized water overnight. Metal salts used were copper (II) chloride (CuDIX), cobalt (II) acetate (CoDIX), magnesium chloride hexahydrate (MgDIX), europium (II) chloride (EuDIX), iron (II) chloride (FeDIX), and zinc chloride (ZnDIX).

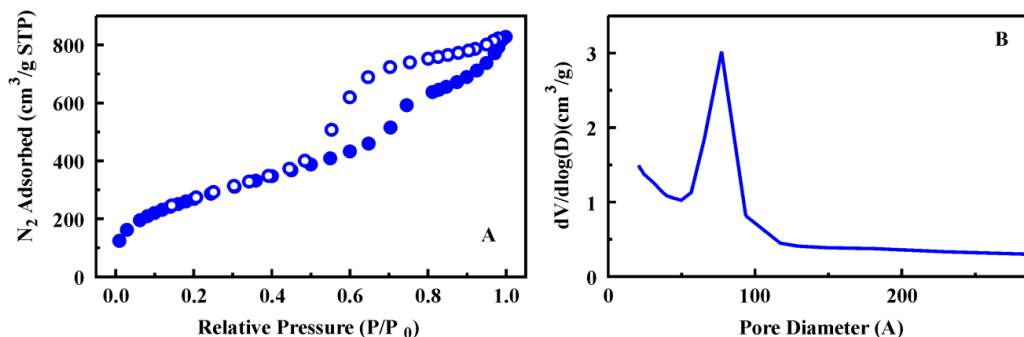


Fig. 3 — Characterization of EA5. (A) Nitrogen adsorption / desorption isotherm. (B) Pore size distribution.

Different metals were incorporated into the porphyrin to evaluate phosgene capture by the material variants. Selection of a candidate material from the metal variants was accomplished based on comparison of phosgene capture from a single exposure. Air (50 mL) containing 280 μg phosgene was passed through the sorbent columns (50 mg). The column effluents were analyzed by HPLC using an impinge-based method [36,42]. Table 3 summarizes the results. The Cu(II) functionalized sorbent removed significantly more phosgene than the other metal variants. As a result, the Cu(II)DIX sorbent was selected for full characterization as described in the following paragraph.

Table 3 — Capture of Phosgene by DIX Sorbent Columns

Sorbent	% phosgene removed [†]	Peak excitation (nm)	Peak emission (nm)	Toluene % change [*]	Phosgene % change [*]
Cu(II)DIX EA5	55	365	500	16	40
Cu(I)DIX EA5	23	365	500		
FeDIX EA5	30	415	640	15	11
EuDIX EA5	23	410	660	21	28
ZnDIX EA5	16	410	640	13	48
MgDIX EA5	32	400	680	15	59
CoDIX EA5	35	380	500	N/D	N/D

[†] Based on single exposure (280 μg , 50 mL air) capture by 50 mg sorbent column; ^{*} Calculated based on ratio of peak minus trough difference intensity to peak intensity of pre-exposure spectrum

Capture, Retention, and Conversion.

To provide a baseline for comparison, the removal of phosgene by the E50 sorbent was evaluated. It was not expected to provide any binding capacity for phosgene. Overall, the total phosgene retained was 47 μg (Fig. 4). The Cu(II)DIX functionalized sorbent retained 271 μg phosgene. This quantity is approximately equivalent to the estimated number of porphyrin sites on the sorbent column (2.7 mmol/g). When the sorbent was evaluated at varied levels of relative humidity, a slight increase in capacity was observed (Fig. 4). The interaction of phosgene with water is known to produce carbonic acid and hydrochloric acid [42]. The activity of phosgene upon interaction with water raises a point of interest due to the potential for formation of acid products. Ion chromatography was used to determine whether chloride, carbonate, or hypochlorite could be detected in the column effluent. No carbonate or hypochlorite were detected in any samples, and only $\sim 5\%$ of the chloride applied as phosgene was recovered. When the sampling rate and impinger volumes were reduced to produce a higher concentration in each impinger, impinger solutions ($10\times$) contained no detectable carbonate or hypochlorite. Figure 5 shows chloride recovery from experiments using the E50 ethane-bridged sorbent and those with the Cu(II)DIX sorbent. In the absence of porphyrin, a mole balance of chloride is recovered in the column effluent. For the Cu(II)DIX functionalized sorbent, only 41% of the chloride is recovered.

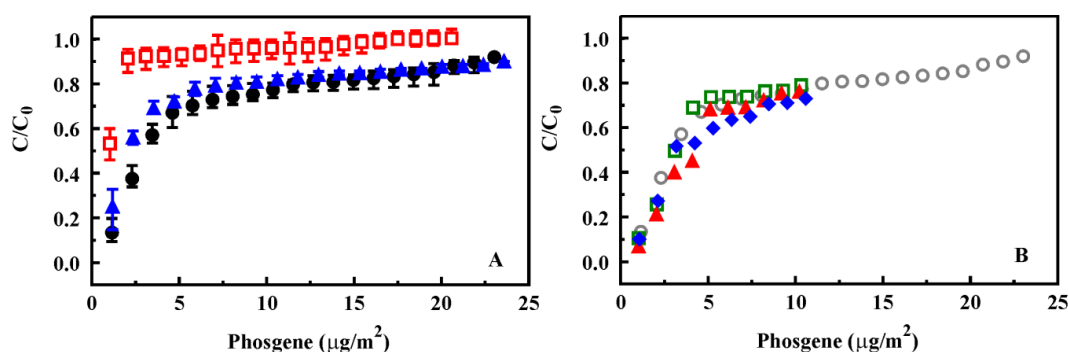


Fig. 4 — Phosgene breakthrough on sorbent columns. (A) Capture of phosgene by E50 (red square; total 47 μg), Cu(II)DIX sorbent (black circle; total 271 μg), and Cu(I)DIX sorbent (blue triangle; total 216 μg) under dry conditions. (B) Capture of phosgene by Cu(II)DIX sorbent under 32% (triangle; 201 μg), 54% (diamond; 235 μg), and 80% (square; 234 μg) relative humidity. The data collected under dry conditions are presented for comparison (circle; 192 μg at identical application level).

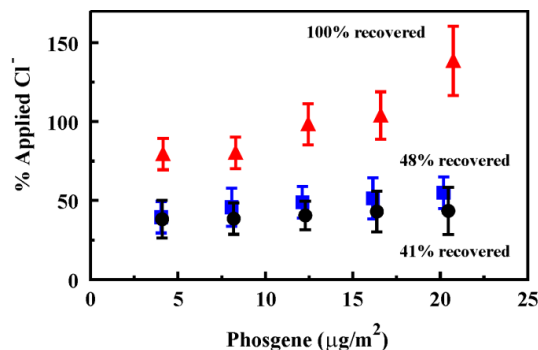


Fig. 5 — Chloride recovery. Chloride recovered from breakthrough experiments for the porphyrin functionalized sorbents (Cu(II)DIX, 41%, circle and Cu(I)DIX, 48%, square) was less than that expected based on a mass balance while all chloride was recovered from experiments using the base sorbent (triangle).

To evaluate reusability, a single sorbent column was subjected to phosgene application to the point of complete breakthrough. The column was then subjected to a bake (at 110 °C overnight)-breakthrough cycle twice more. There was some loss in capacity from the first cycle (~20%); however, the column continued to remove phosgene with a capacity significantly greater than that of the bare sorbent over all cycles (Fig. 6). The impact of illumination on column performance was also evaluated. Under illumination, the total phosgene removed was increased to 513 μg from 271 μg . When a Cu(I)DIX sorbent column was similarly evaluated, phosgene removal increased from 216 to 335 μg under illumination (Fig. 6). These use cycles did not result in morphological changes to the sorbent materials; pore size and surface area remained unchanged.

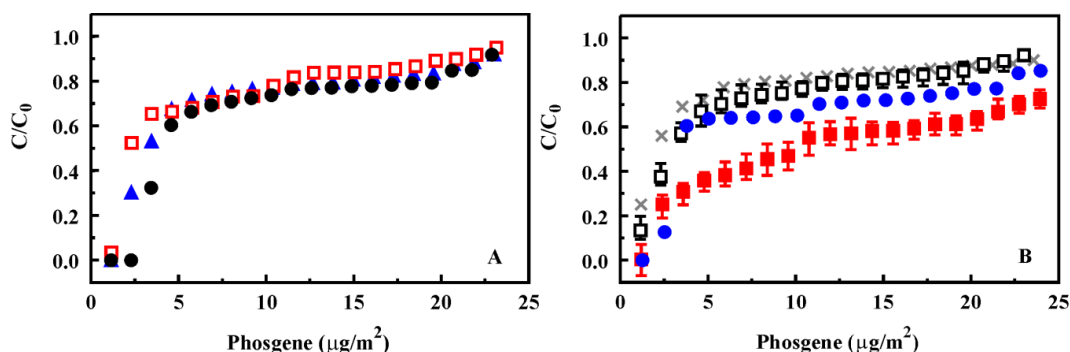


Fig. 6 — Reusability. (A) Performance over repeated cycles of target challenge followed by baking of the sorbent under dry conditions: fresh (circle; 345 μg), second cycle (triangle; 288 μg), and third cycle (square; 263 μg). (B) Illumination of sorbents results in increased target removal: dark Cu(II)DIX (black, 271 μg), illuminated Cu(II)DIX (red, 513 μg), dark Cu(I)DIX (gray, 216 μg), and illuminated Cu(I)DIX (blue, 335 μg).

Spectrophotometric Characteristics

Changes in the fluorescence characteristics of the sorbents upon phosgene exposure were monitored using a microwell plate format. It was necessary to eliminate the contribution of toluene to changes in the fluorescence characteristics of the sorbents. Fluorescence of the sorbents was measured before/after exposure to toluene and before/after exposure to phosgene in toluene. Difference spectra were calculated by subtraction of pre-exposure spectra from post-exposure spectra. Phosgene difference spectra were then compared to changes resulting from toluene exposure. Exposure of FeDIX and CoDIX functionalized sorbents to toluene and phosgene resulted in only minimal changes (Fig. 7). Changes could be attributed to interaction of the sorbent with toluene and full relaxation of the changes occurred over 0.5 h. Stronger changes in fluorescence were observed for Cu, Mg, Zn, and Eu sorbents (Figs. 8 and 9). Changes resulting from interaction with toluene were observed to relax during the first 0.5 h following exposure. While some relaxation of changes resulting from phosgene exposure was also observed, a significant portion of the changes was retained by the Cu, Zn, and Eu sorbents. The Cu, Mg, and Zn sorbents offered the largest relative changes (Table 3).

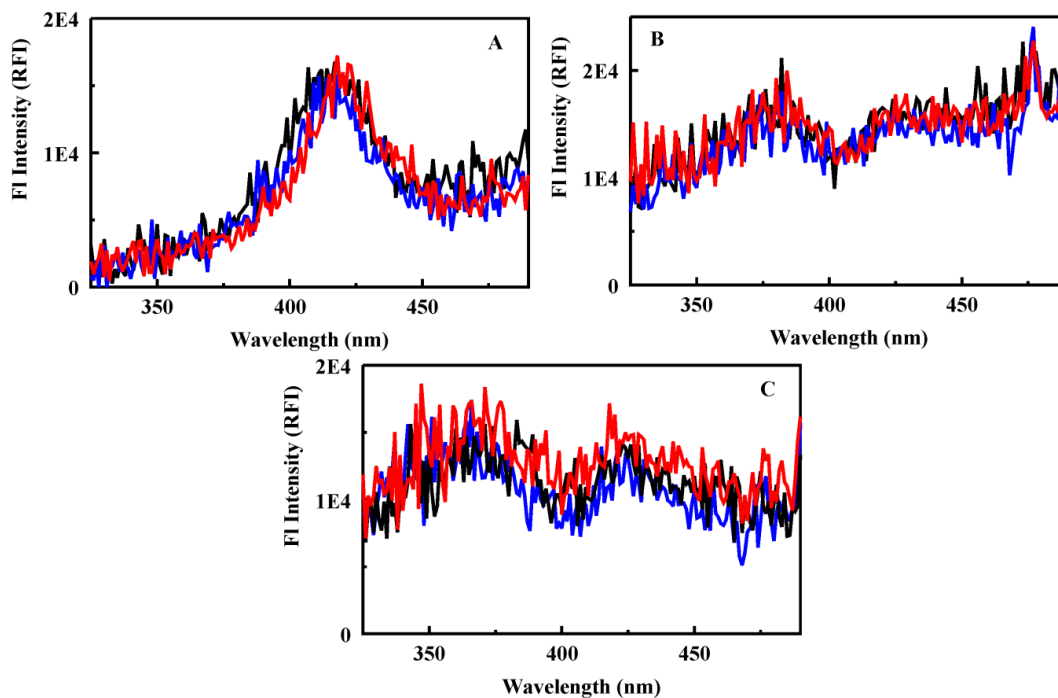


Fig. 7 — Low fluorescence materials. Fluorescence of DIX variants before (black) and immediately following exposure to toluene (blue) and phosgene (red): FeDIX (A), CoDIX (B), and Cu(I)DIX (C).

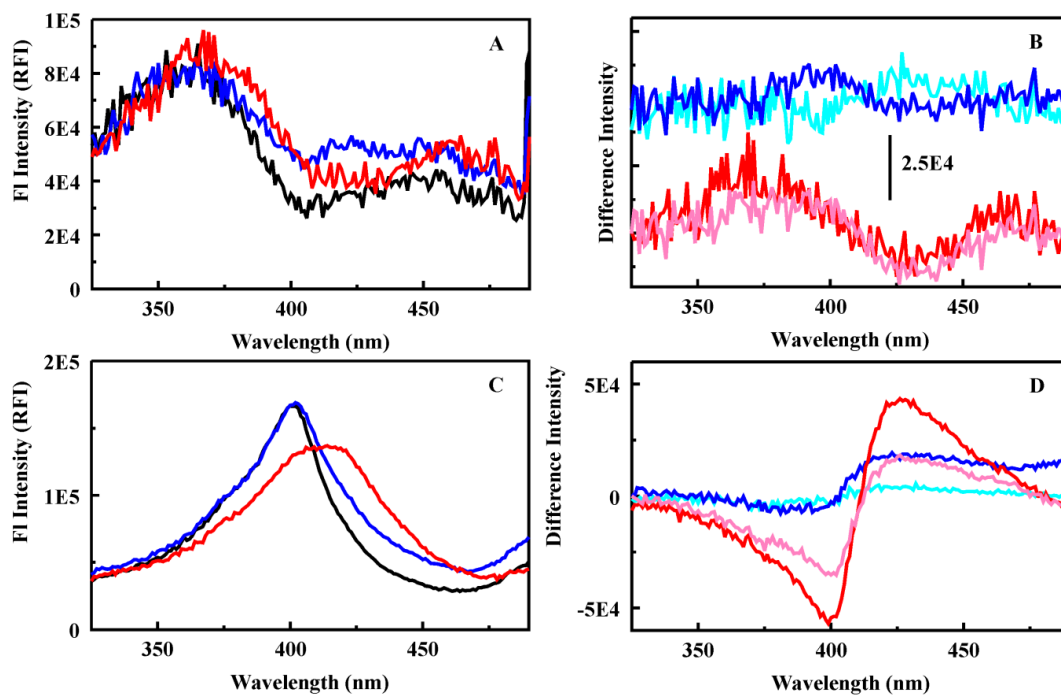


Fig. 8 — Fluorescence response to phosgene. Fluorescence spectra of DIX variants (500 nm emission) before (black), and immediately after exposure to toluene (blue) and phosgene (red). Also shown are difference spectra (blue – toluene, red – phosgene). In addition, difference spectra for materials following a 0.5 h re-equilibration period are provided (cyan – toluene, pink – phosgene), CuDIX (A, B), and MgDIX (C, D).

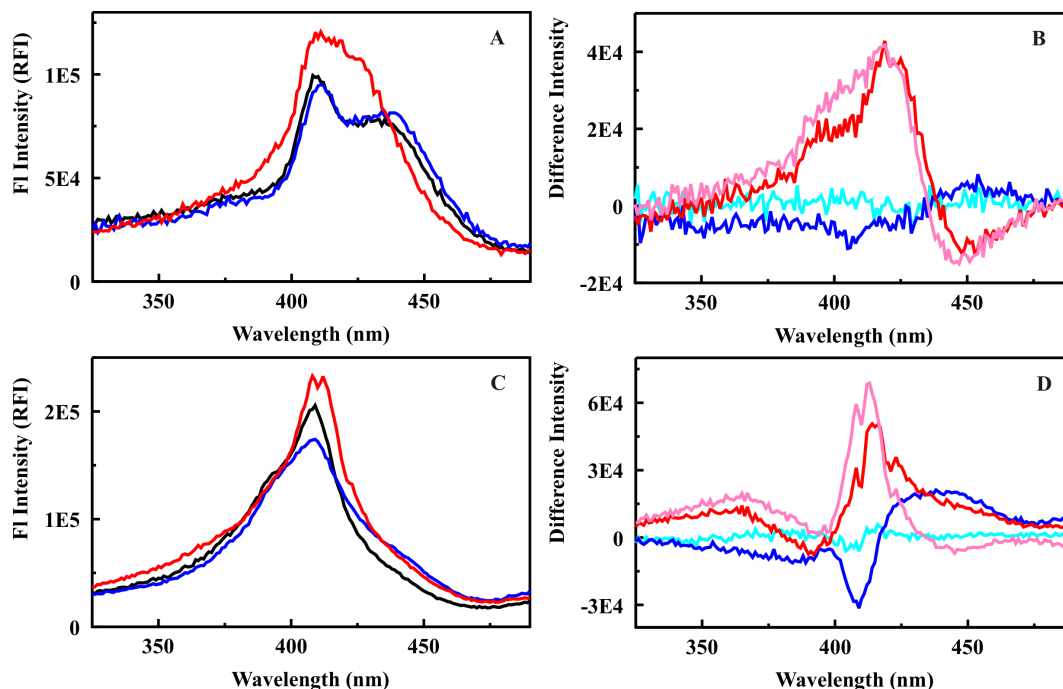


Fig. 9 — Fluorescence response to phosgene. Fluorescence spectra of DIX variants (500 nm emission) before (black), and immediately after exposure to toluene (blue) and phosgene (red). Also shown are difference spectra (blue – toluene, red – phosgene). In addition, difference spectra for materials following a 0.5 h re-equilibration period are provided (cyan – toluene, pink – phosgene), ZnDIX (A, B), and EuDIX (C, D).

Analysis by HPLC indicated that similar phosgene removal was obtained for the Co and Fe sorbents and those with stronger fluorescence characteristics. Images of sorbent columns were collected using a scanner before and after exposure to phosgene as well as following an air purge. Total phosgene bound during the exposure was evaluated using the impinger based HPLC protocol (Table 3). The RGB color values from the resulting images were used to provide an indication of changes in the spectrophotometric characteristics of the sorbents (Fig. 10). These results indicate the strongest interactions occurred with the Cu and Mg sorbents. In fact, these changes were discernible by visual inspection. Changes in reflectance were observed for all sorbents, though the magnitude of those changes was significantly less than that observed for Cu and Mg sorbents.

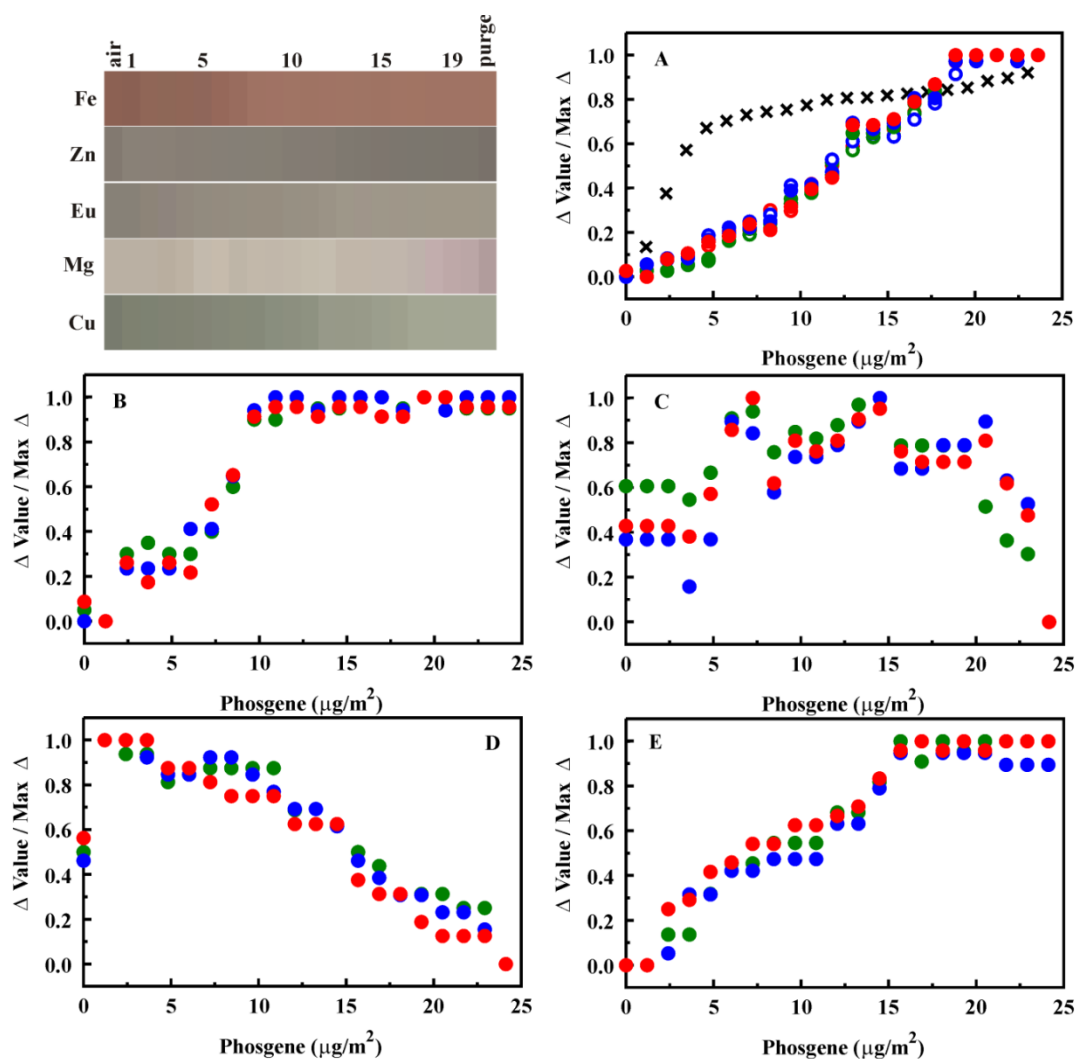


Fig. 10 — Lifecycle. Shown here are the color changes for sorbents exposed repeatedly to phosgene (20 additions, total 25 mg/m^2) to the point of complete breakthrough: Cu(II)DIX (A), FeDIX (B), MgDIX (C), ZnDIX (D), and EuDIX (E). Panel A provides the results from HPLC analysis for comparison.

The reflectance characteristics of the sorbents over the column performance cycle from fresh material to complete target breakthrough were evaluated (Fig. 10). Total loading levels for complete breakthrough were determined based on the breakthrough studies described above. The air equilibrated Cu sorbent had reflectance RGB values of 126, 129, and 112, respectively. Over 16 phosgene additions ($\sim 18 \mu\text{g phosgene} / \text{m}^2$ sorbent), these values changed by 38, 37, and 36, respectively. As shown in Fig. 10, the changes in the values did not follow the trend observed for phosgene breakthrough as analyzed by HPLC. The reflectance changes would tend to indicate that column saturation occurs at a slightly lower loading level.

Based on the color trends presented (Fig. 10), the Cu sorbent appears to become lighter in color as saturation loading levels are approached. The Fe and Eu sorbents also appear to become lighter while the Zn sorbent gets darker over the range of loading levels. The Mg sorbent gradually shows increasing red tones over this range (Fig. 10). Plots of the normalized changes in RGB values show a rapid saturation of

the Fe sorbent ($\sim 9.7 \mu\text{g}/\text{m}^2$). The Eu sorbent continues to show reflectance changes to an exposure level of $\sim 14.4 \mu\text{g}/\text{m}^2$. Interestingly, the Mg sorbent doesn't show a trend for the RGB values across the range of exposures. Instead, the color profile observed results from changing ratios of the color values.

Simple Grafted Functionalities

Our previous efforts focused largely on modification of the bridging groups and morphological characteristics of organosilicate sorbents for application to the capture of targets from aqueous solutions [26-29,43-45]. The capture of light gas targets such as ammonia and cyanogen chloride requires a different approach. Alterations to the characteristics of the organosilicate scaffold, achieved through post-synthesis modification, provide accessible pendant functional groups for interaction with the targets. This section addresses the impact of two such modifications providing pendant amine and isocyanate groups.

Material Synthesis

These studies focused on application of an ethane bridged sorbent that was modified through grafting. The material (E50) was synthesized by a preparation method using Pluronic P123 in acidic media [17,37]. Briefly, Pluronic P123 (1.9 g) and TMB (0.5 g) were dissolved in 0.1 M HNO_3 (6.07 g) with stirring at $\sim 60^\circ\text{C}$. The solution was allowed to cool to room temperature and silane precursor (2.12 g BTE) was added drop-wise. The reaction mixture was stirred until homogeneous and then transferred to a culture tube which was sealed tightly and heated at 60°C overnight. The tube was unsealed and heated at 60°C for 2 d, and then 80°C for 2 d. The product, in the form of a white monolith, was refluxed three times in 1 M hydrochloric acid in ethanol for at least 12 h to extract the surfactant, a process that resulted in crushing the monolith to a powder. The powder was collected by suction filtration, rinsed with ethanol and water, and dried at 110°C . Functional groups were incorporated on the surface of the organosilicate material (E50) through post-synthetic grafting. Sorbent material was dried at 110°C and added to a solution of either the APS (E50A) or the ICS (E50I) precursor in 200 mL toluene to achieve a final concentration of 0.6 mol precursor per gram sorbent. The mixture was refluxed for 18 h. Grafted material was collected by vacuum filtration, washed with toluene, and dried at 110°C .

E50 has an average BET surface area of $1,096 \text{ m}^2/\text{g}$ and total pore volume of $1.04 \text{ cm}^3/\text{g}$. The isotherm is type IV, but has characteristics that suggest a complex pore structure (Fig. 11) [46]. It has a wide pore size distribution (< 0.2 to 50 nm) with a shoulder-like peak at 76 \AA (average pore diameter 81 \AA). XRD confirms the lack of an ordered meso-structure (Fig. 11). Scanning electron microscopy shows a foam-like texture (Fig. 11) similar to previously reported materials [39]. Functionalization of E50 with amine groups (E50A) reduces the surface area of the material to $637 \text{ m}^2/\text{g}$. Functionalization with isocyanate groups (E50I) yielded only a slight change in surface area ($1,012 \text{ m}^2/\text{g}$). The pore volume of E50A is less than that of E50 ($0.87 \text{ cm}^3/\text{g}$), while that of E50I shows little change from the scaffold material ($1.12 \text{ cm}^3/\text{g}$). Average mesopore diameters are similar to E50 (81 \AA). There is a significant reduction in the pore diameter distribution near the micropore range (leading edge, Fig. 11) resulting from grafting of the functional groups.

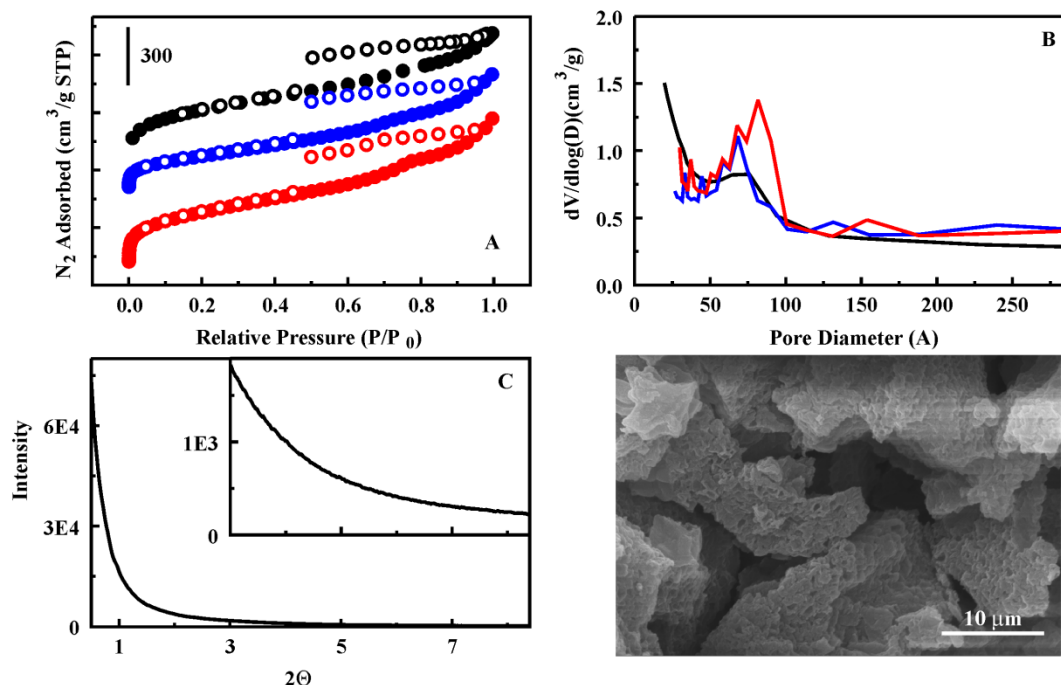


Fig. 11 — Material characteristics (E50, black; E50A, blue; E50I, red). Shown here are nitrogen sorption isotherms (A; E50A offset by -100; E50I offset by -450), and pore size distributions (B) for materials used in these studies. The XRD spectrum (C, inset shows zoom of spectrum above 3) and an SEM image for E50 are also shown.

Ammonia

Figure 12 summarizes the ammonia breakthrough profiles for the organosilicate and control materials. Calculated capacities are provided in Table 4. Under dry conditions, E50 demonstrates higher saturated loading than the carbon control material (BPL/Zn/TEDA). Saturated loading decrease slightly as the pH of the sorbent is increased from pH 6.5 to pH 9. The detrimental effect of increasing pH on ammonia removal is not surprising as ammonia is basic. Increased humidity (80% RH) negatively impacts sorption of ammonia by BPL/Zn/TEDA and E50 at all pH values.

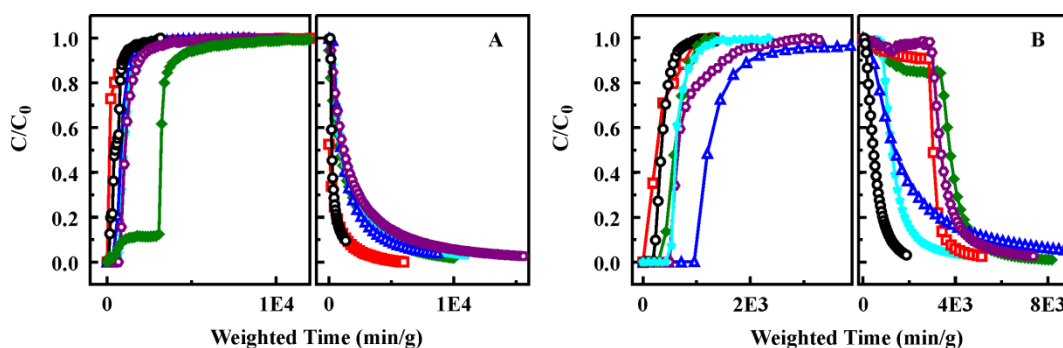


Fig. 12 — Ammonia breakthrough for organosilicates under (A) dry and (B) humid RH conditions. E50 as synthesized (green), at pH 7 (purple), and at pH 9 (cyan) is compared to BPL/Zn/TEDA (black), E50A (red) and E50I (blue) functionalized materials.

Table 4 — Calculated Target Loading Capacities* – Ammonia and Cyanogen Chloride

		Ammonia			Cyanogen Chloride		
		Sorbent Mass	Sat. Loading	Post-Purge	Sorbent Mass	Sat. Loading	Post-Purge
Sample	RH	mg	mol/kg	mol/kg	mg	mol/kg	mol/kg
BPL/Zn/TEDA	0/0	20.6	0.7	0.4	21.8	1.2	0.7
	80/80	22.7	0.5	0.0	20.9	2.1	2.0
E50	0/0	6.6	4.0	1.9	8.6	0.5	0.1
	80/80	7.3	0.5	0.0	5.3	0.2	0.1
E50 (pH 7)	0/0	6.3	1.5	0.0	9.0	0.3	0.1
	80/80	10.7	1.0	0.1	8.7	0.1	0.0
E50 (pH 9)	0/0	11.0	1.4	0.0	10.7	0.5	0.0
	80/80	10.0	0.8	0.0	14.2	0.2	0.1
E50A	0/0	4.8	1.2	0.5	4.7	2.0	1.8
	80/80	5.6	0.2	0.0	5.0	2.8	2.7
E50I	0/0	3.3	1.1	0.0	4.7	0.9	0.7
	80/80	4.4	2.1	0.0	5.5	0.4	0.3

* Capacity values are calculated to sorbent saturation (Sat. Loading) and after purging the column with air (Post-Purge).

Grafting of amine (E50A) and isocyanate (E50I) functional groups to the surface of E50 decreases the ammonia capacity per gram under dry conditions, possibly due to a reduction in available surface hydroxyl groups. All values reported here are normalized based on weight. It is important to note, however, that when the performance of E50 and E50A are compared on a per surface area basis, E50A slightly out performs E50 ($1.9 \mu\text{mol}/\text{m}^2$ versus $1.6 \mu\text{mol}/\text{m}^2$). Increased humidity negatively impacts the sorption of ammonia by E50A. E50I shows improved performance at 80% RH. This behavior is likely due to the reaction of the surface tethered isocyanate groups with water and ammonia leading to the formation of ammonium isocyanate [47]. Figure 13 shows the water binding isotherms for the sorbents. All materials show significant desorption after feed termination, indicating that any interaction between ammonia and the sorbents is highly reversible.

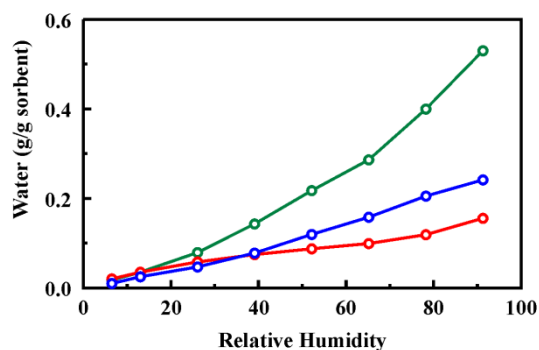


Fig. 13 — Water binding isotherms for E50 (green), E50A (red), and E50I (blue).

Cyanogen Chloride

Cyanogen chloride saturated loading levels for E50 are significantly lower than those for the carbon control regardless of the pH of the sorbent under dry conditions. Breakthrough curves are presented in Fig. 14 with calculated loading levels provided in Table 4. The shape of the E50 breakthrough curve is indicative of a physical sorption mechanism. E50 demonstrated immediate breakthrough under high RH conditions regardless of sorbent pH. Similar behaviors under dry and humid conditions are seen for E50I, indicating that the isocyanate functionality has no effect on CK removal. E50A, however, shows significantly enhanced performance over E50 and the carbon sorbent. The sorbent exhibits a steep decrease in CK concentration after feed termination (Fig. 14), indicating that CK remaining in the porous structure is strongly adsorbed. It is possible that the amine surface groups react with CK as this has been shown for other amine groups [48], although this typically occurs with tertiary amines. It is also possible that the basicity of the sorbent (pH 9.2) coupled with the amine groups creates hydroxyl groups necessary for CK hydrolysis.

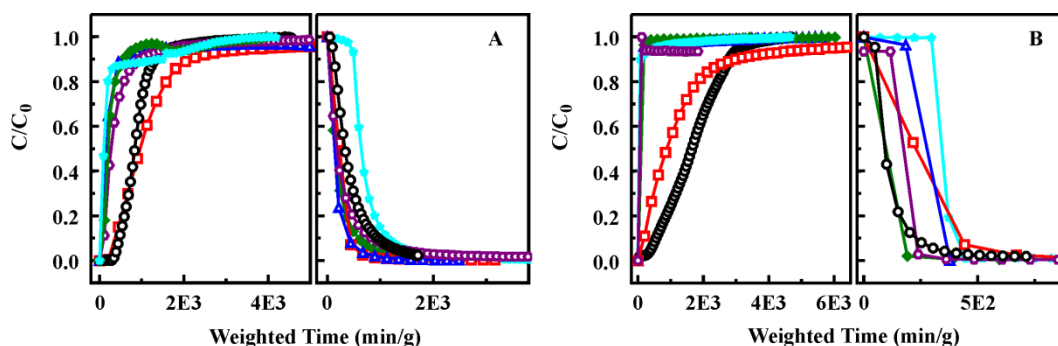


Fig. 14 — Cyanogen chloride breakthrough for organosilicates under (A) dry and (B) humid RH conditions. E50 as synthesized (green), at pH 7 (purple), and at pH 9 (cyan) is compared to BPL/Zn/TEDA (black), E50A (red) and E50I (blue) functionalized materials.

Sulfur Dioxide

E50 does not retain sulfur dioxide regardless of the pH of the sorbent or the humidity conditions. (Fig. 15 and Table 5). Functionalization of E50 using isocyanate groups (E50I) does not alter the performance of the sorbent. Amine functionalization did provide an improvement in sulfur dioxide retention. In fact, E50A provides substantially higher removal than the carbon control. Sulfur dioxide interaction with amine groups has been investigated previously, and many interactions have been shown to form molecular adducts [49]. It is likely that this mechanism is at work in the E50A sorbent. This is further supported by the fact that, although the interaction of sulfur dioxide and the sorbent is substantial, it is also reversible as indicated by the slope of the breakthrough curve following feed termination.

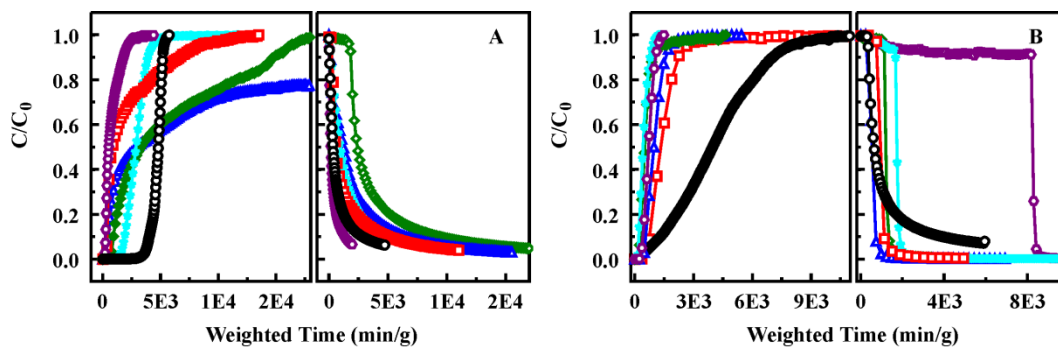


Fig. 15 — Sulfur dioxide breakthrough for organosilicates under (A) dry and (B) humid RH conditions. E50 as synthesized (green), at pH 7 (purple), and at pH 9 (cyan) is compared to BPL/Zn/TEDA (black), E50A (red) and E50I (blue) functionalized materials.

Table 5 — Calculated Target Loading Capacities* – Sulfur Dioxide and Octane

		Sulfur Dioxide			Octane		
		Sorbent Mass	Sat. Loading	Post-Purge	Sorbent Mass	Sat. Loading	Post-Purge
Sample	RH	mg	mol/kg	mol/kg	mg	mol/kg	mol/kg
BPL/Zn/TEDA	0/0	23.6	0.3	0.0	29.3	3.3	2.7
	80/80	20.1	0.8	0.5	18.1	2.9	2.2
E50	0/0	7.8	0.1	0.0	6.9	3.8	1.8
	80/80	5.9	0.1	0.0	8.5	0.4	0.3
E50 (pH 7)	0/0	7.7	0.1	0.0	32.8	0.6	0.3
	80/80	5.7	0.2	0.0	8.6	0.2	0.1
E50 (pH 9)	0/0	11.3	0.1	0.0	9.4	2.1	0.2
	80/80	12.4	0.1	0.0	13.4	0.2	0.1
E50A	0/0	7.1	1.0	0.0	6.0	1.6	0.5
	80/80	6.3	1.1	0.0	2.8	1.0	0.8
E50I	0/0	4.2	0.1	0.0	6.8	9.2	7.6
	80/80	4.6	0.1	0.0	4.3	0.8	0.6

* Capacity values are calculated to sorbent saturation (Sat. Loading) and after purging the column with air (Post-Purge).

Octane

Figure 16 presents octane breakthrough curves for the materials studied; the octane capacities are summarized in Table 5. The E50 sorbent provides octane removal under dry conditions, though, based on the shape of the curve, there seem to be mass transfer limitations. Where the carbon sample exhibits a classic S-curve, E50 shows initial breakthrough followed by substantial additional capacity. This tends to indicate bulk and internal diffusion limitations. Under humid conditions the phenomenon is exacerbated; breakthrough occurs more rapidly, and saturated loading levels are decreased (Fig. 16).

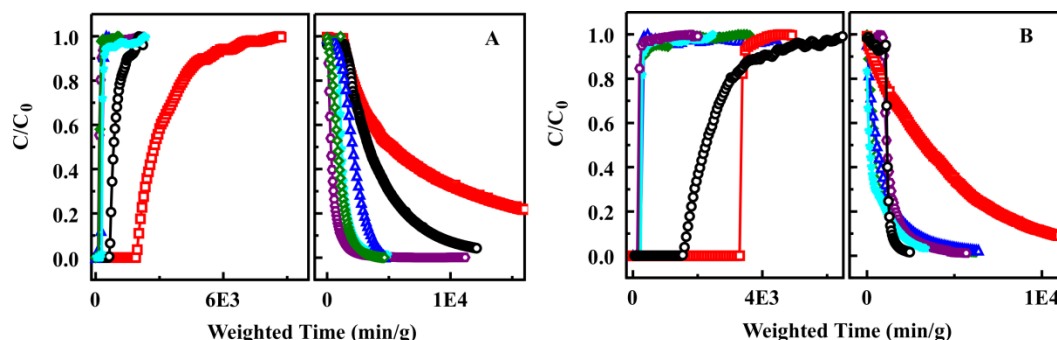


Fig. 16 — Octane breakthrough for organosilicates under (A) dry and (B) humid RH conditions. E50 as synthesized (green), at pH 7 (purple), and at pH 9 (cyan) is compared to BPL/Zn/TEDA (black), E50A (red) and E50I (blue) functionalized materials.

Grafting of isocyanate groups increases octane capacity under dry conditions. Although there is significant initial octane breakthrough on E50I, the calculated capacity is approximately three times that of the carbon and E50 samples. When the low loading region of the breakthrough curves for the E50 materials are evaluated separately (Fig. 15), distinct regimes of behavior can be observed. One possibility is that octane sorption is limited by internal pore diffusion rates resulting from condensation in smaller pores first which may restrict access to the remaining sorbent pore volume. This would also enhance physical sorption and retention once the octane penetrates into the pore structure. The possibility that pore condensation is occurring in E50I is supported by the saturated loading level (7.6 mol/kg) which is sufficient to fill 25% of the reported pore volume (1.12 cm³/g). Regardless of the octane sorption mechanism, water is preferentially adsorbed under humid conditions as all organosilicate materials exhibit a substantial decrease in octane sorption capacity at 80% RH.

Chlorine

Retention of chlorine by E50 was negligible (Fig. 17). Functionalization of the sorbent with amine groups resulted in a significant increase in the capture target (1.19 mol/kg) and the target was retained following the air purge. Limitations on time and equipment prevented full characterization (only 0% RH data collected) of the E50A sample, and E50I was not evaluated.

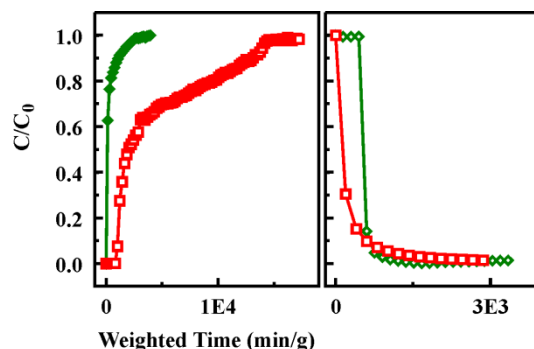


Fig. 17 — Chlorine breakthrough for organosilicates under dry conditions. E50 as synthesized (green) and E50A (red) materials. E50 saturated loading = 0.10 mol/kg; with desorption = 0.07 mol/kg. E50A saturated loading = 1.19 mol/kg; with desorption = 1.12 mol/kg.

Porphyrin Functionalized

Having evaluated basic scaffold materials and simple functionalities [37], we sought to determine if metalloporphyrins could enhance the performance of the materials. Porphyrins of varying structure were evaluated to determine the impact of structure on the interaction of the coordinated metal with the gas targets. Three porphyrin structures were considered (Fig. 2). C₄TPP is soluble in slightly basic, aqueous solutions and offers electron withdrawing carboxylic acid groups at the para-position of the phenyl rings. N₄TPP offers a highly similar structure where carboxylic acid groups are replaced by electron donating amine groups making this porphyrin soluble in slightly acidic, aqueous solutions. The final porphyrin used in these studies (DIX) has a significantly different structure without the phenyl rings of the other porphyrins and offers a reduced degree of conjugation. This porphyrin was previously used for removal of phosgene ([above](#)) [36,50]. As a result of the partial success achieved with MOF materials, copper was selected for incorporation into the porphyrin embedded materials [41,51-55]. Another porphyrin, Co C₁TPP, was evaluated on the basis of earlier successes using cobalt modified sorbents. This porphyrin offers a coordinated cobalt atom in a hydrophobic structure with only a single peripheral group used for covalent immobilization. The impact of material morphology on the performance of porphyrin modified materials was evaluated using variations on synthetic procedures, and the implication of the differences in Cu (I) and Cu (II) materials mentioned in the previous section were further explored. Finally, a metalloporphyrin embedded material synthesized for use against organophosphates [29] was challenged with the air purification targets.

Material Synthesis

Synthesis of E50 and EA5 were described in earlier sections. The materials synthesized for these comparisons followed the standard preparation method [17]. Variations on the concentrations of the reagents used produces differences in the morphological characteristics of the resulting sorbents. The variations used here are detailed in Table 6. Amine functional groups were directly incorporated into EA5, EA2, EB, and EC sorbents (Table 2) through inclusion of 0.05 g (EA5) or 0.025 g APS (all others) with the BTE in the precursor mixture. For all other amine functionalized materials, post-synthetic grafting of APS was used as described [above](#). For ED13, the target analog used for imprinting was generated through esterification of Pluronic P123 with diethyl chlorophosphate [41-43]. Briefly, P123 (4g; 0.7 mmol) and diethyl chlorophosphate (0.4 mL; 3 mmol) were dissolved in 60 mL of dichloromethane. Magnesium turnings were added and the mixture was refluxed for 3 h. The liquid was shaken with 60 mL 2% NaHCO₃ in a separatory funnel. The organic phase was then extracted and evaporated under vacuum. For the sorbent, Pluronic P123 (1.66 g) was dissolved in 0.1 M HNO₃ (7.5 g) with TMB (0.6 g) and 0.24 g of the target analog at 60°C with continuous stirring. To this solution, a mixture of BTE (1.06 g) and DEB (1.468 g) was added dropwise. The mixture was stirred until homogenous, transferred to a culture tube, sealed, and heated at 60 °C overnight. The tube was unsealed to dry for two days at 60 °C and two days at 80 °C. Surfactant was removed by refluxing three times for 12 h in 1 M HCl followed by rinsing and drying at 110 °C. MM3 was synthesized similarly using 0.3 g TMB and 8.0 g HNO₃.

Porphyrin incorporation into the amine-functionalized sorbents was accomplished using EDC chemistry as described [above](#). Porphyrin incorporation into isocyanate-functionalized sorbents was accomplished through incubation of the sorbent (1 g in 100 mL) with a porphyrin bearing primary amine functional groups (0.6 mM) overnight. Following incubation, the sorbent was collected by vacuum filtration and rinsed with ethanol and water. The absorbance spectra of the rinsates were collected to determine porphyrin concentrations. For the materials described in these studies, porphyrin absorbance spectra were not observed for the rinse solutions. Metals were incorporated into porphyrin-functionalized materials by refluxing the sorbent in a solution containing 3 mM copper (II) chloride or nickel (II)

chloride in deionized water overnight. The quenched fluorescence of the resulting materials is indicative of copper metalloporphyrin formation (Fig. 18).

Table 6 – Summary of Reagent Combinations Used for Synthesis

Material	Pluronic P123 (g)	0.1 M HNO ₃ (g)	TMB (g)	Precursors
EA5	1.9	9.5	0.4	0.05 g APS + 2.12 g BTE
EA2	1.9	9.5	0.3	0.025 g APS + 2.12 g BTE
EB	1.9	9.5	0.2	0.025 g APS + 2.12 g BTE
EC	1.9	9.5	0.3	0.025 g APS + 2.12 g BTE
E50	1.9	6.07	0.5	2.12 g BTE
ED13	1.9	7.5	0.55	1.47 g DEB + 1.06 g BTE
MM3	1.9	8.0	0.3	1.47 g DEB + 1.06 g BTE

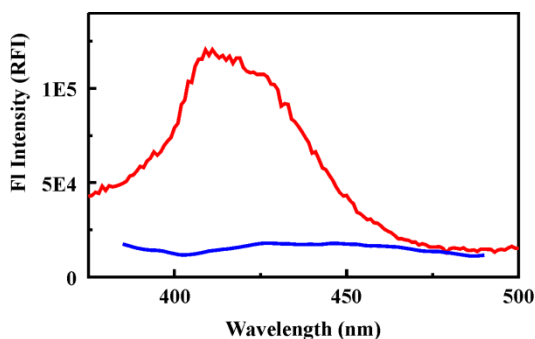


Fig. 18 — Fluorescence quenching. Fluorescence spectra of DIX adsorbed onto E50 (red) without and with (blue) copper.

Morphological characteristics for the materials are provided in Fig. 19 and Table 2. EA5 had a surface area of 1,061 m²/g, a pore volume of 1.33 cm³/g, and an average pore diameter of 79 Å. EA2 had a surface area of 685 m²/g, a pore volume of 0.72 cm³/g, and an average pore diameter of 62 Å. The surface area of E50 was 1,096 m²/g with a pore volume of 1.04 cm³/g and an average pore diameter of 81 Å. Grafting of APS (E50A, 2 mmol/g sorbent) to the surface of this material resulted in reduced surface area (637 m²/g) and pore volume (0.87 cm³/g) with little change in pore diameter. Grafting of ICS (E50I, 2 mmol/g sorbent) to the surface of E50 caused only slight variations in the materials characteristics (surface area = 1,012 m²/g; pore volume = 1.12 cm³/g; average pore diameter 81 Å). Nitrogen sorption analysis for the porphyrin-embedded sorbents indicated that porphyrin incorporation had little impact on the transport of N₂ throughout the pore structure (Figs. 19 and 20).

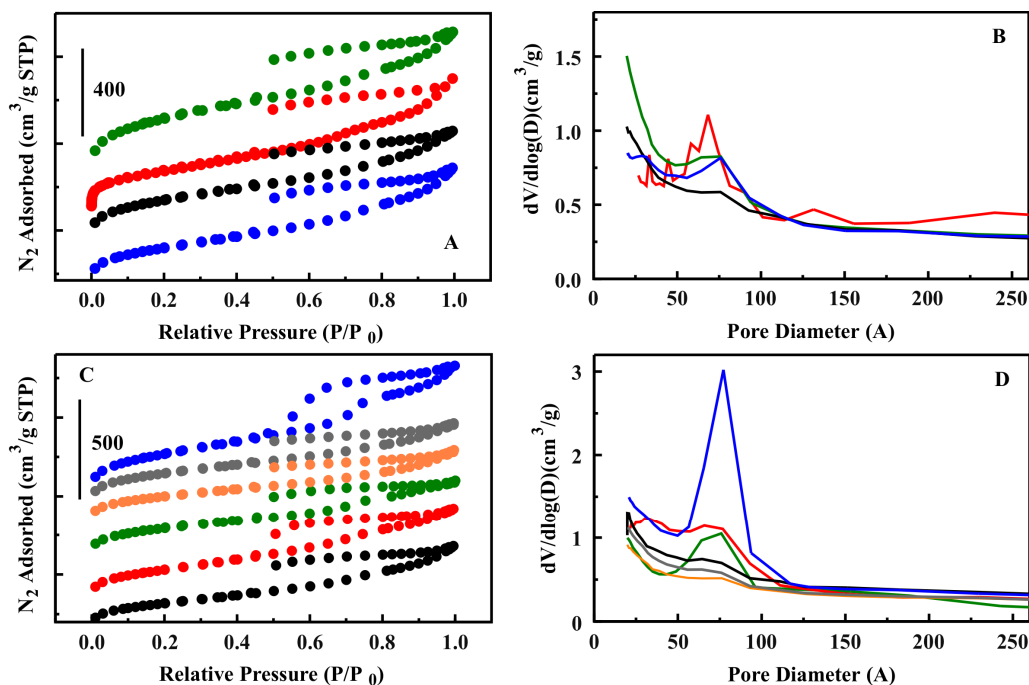


Fig. 19 — Material characteristics for porphyrin functionalized sorbents. Nitrogen adsorption/desorption (left) and pore size distribution (right) data. (A & B) E50 (green), E50A (red), E50A-CuD (black), and E50A5-CuC (blue). (C & D) EA5 (blue), E50A1-CuD (gray), E50A5-CuD (orange), EA2 (green), EA2-CuC (red), and E50A10-CuC (black).

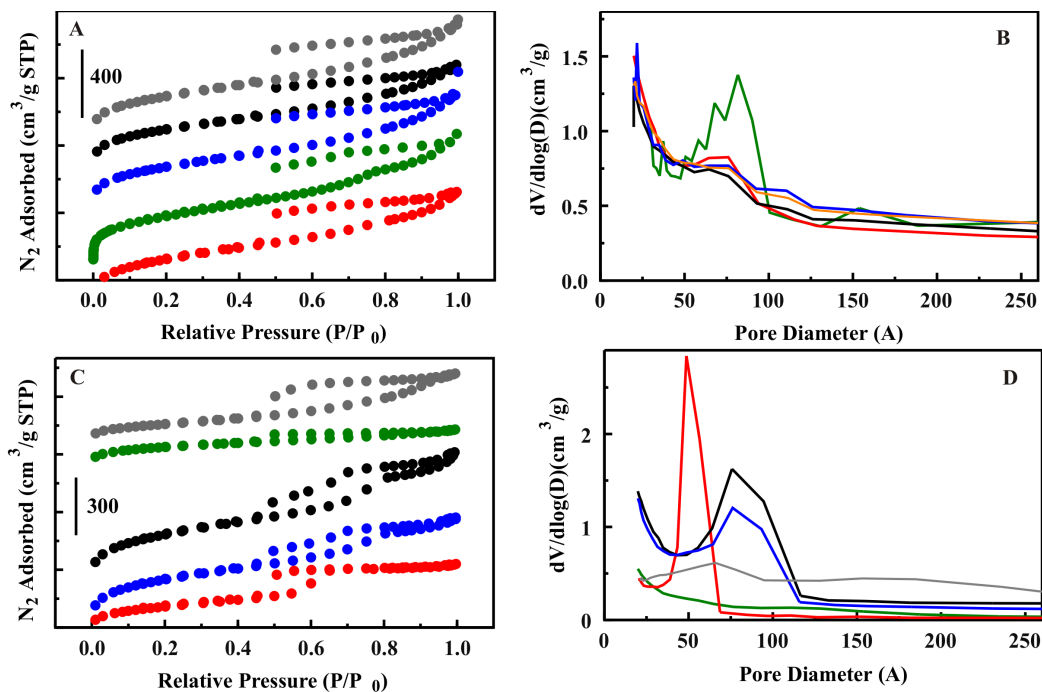


Fig. 20 — Material characteristics for porphyrin functionalized sorbents. Nitrogen adsorption/desorption (left) and pore size distribution (right) data. (A & B) E50 (red), E50I (green), E50I10-CuN (blue), E50I-CuN (black), and E50I5-CuN (gray). (C & D) ED13 (red), EB Cu1D (blue), EB Cu2D (black), EC Cu1D (green), and EC Cu2D (gray).

Ammonia Capture

In Fig. 21, breakthrough data for the E50 sorbent with varied Cu DIX loading are presented under dry and humid conditions. All of these materials showed higher saturated loading levels than the carbon control (Table 7). In the case of the grafted materials, the E50 sorbent structure is largely retained for lower APS loading levels and some pore blockage may occur at higher levels (Fig. 19). It can also result in the loss of pore volume in the smaller mesopore or micropore ranges. The shape of the ammonia breakthrough curve for the Cu DIX sorbents resulting from grafting is similar to that of the APS grafted material reported above (Fig. 12). The ammonia capacity at saturation is higher than that reported for E50A (Table 7); however, as in the case of E50A, little ammonia is retained by the sorbents following desorption. No trends are observed for the varied APS loading levels within the sorbents.

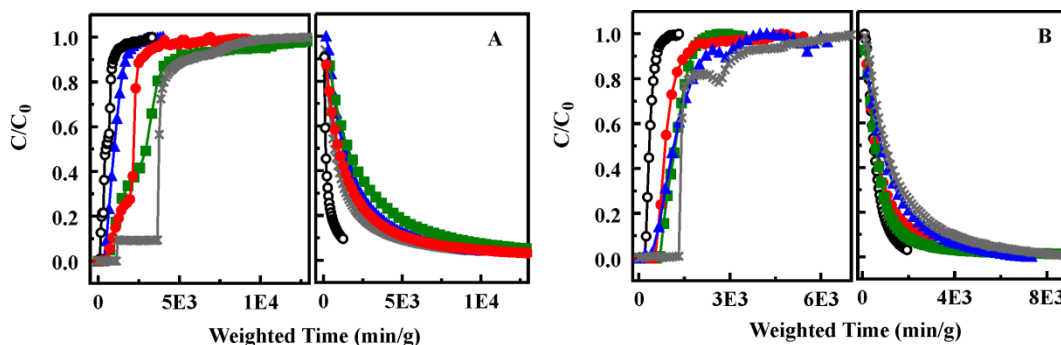


Fig. 21 — Ammonia breakthrough for the Cu DIX materials under dry (A) and humid (B) RH conditions. BPL/Zn/TEDA (black), EA5-CuD (gray), E50A5-CuD (red), E50A-CuD (blue), and E50A1-CuD (green).

The co-condensed CuDIX material (EA5-CuD) has a breakthrough profile (Fig. 21) similar to that observed for the base E50 sorbent (Fig. 12). Under dry conditions, there is low level breakthrough initially followed by additional retention before total target breakthrough is achieved. The elongated form near the top of the breakthrough curve is also apparent. This material is different from the other CuDIX materials evaluated in that the saturated loading is higher under both humid and dry conditions and the retained ammonia following desorption is significant (Table 7). The porphyrin loading level in this sorbent is significantly less than that of the grafted materials. For comparison, a sorbent was prepared by refluxing E50 with copper chloride. This should produce a sorbent in which any retained copper is that coordinated with surface hydroxyl groups. As shown in Table 7, incorporation of copper did not produce the results that were observed with the metalloporphyrin.

Table 7 — Calculated Ammonia Loading Capacities*

		Mass	Sat. Load	Post-Purge			Mass	Sat. Load	Post-Purge
Sample	RH	mg	mol/kg	mol/kg	Sample	mg	mol/kg	mol/kg	
BPL/Zn/TEDA	0/0	20.6	0.7	0.4	EA2-CuC	12.2	1.2	0.0	
	80/80	22.7	0.5	0.0		11.0	1.2	0.0	
E50	0/0	6.6	4.0	1.9	E50A-CuC	12.0	1.1	0.0	
	80/80	7.3	0.5	0.0		8.4	1.3	0.2	
E50-A	0/0	4.8	1.2	0.5	E50A3-CuC	13.3	1.0	0.0	
	80/80	5.6	0.2	0.0		4.7	2.2	0.0	
EA5-CuD	0/0	10.5	4.9	3.0	EB-Cu2D	9.6	1.6	0.0	
	80/80	10.5	2.9	1.1		--	--	--	
E50A-CuD	0/0	6.0	2.4	0.0	EB-Cu1D	--	--	--	
	80/80	5.9	1.2	0.0		9.7	4.1	2.6	
E50A2-CuD	0/0	6.4	1.3	0.0	EC-Cu2D	7.5	0.8	0.0	
	80/80	4.8	2.0	0.5		11.8	0.5	0.0	
E50A1-CuD	0/0	2.9	3.7	0.2	EC-Cu1D	14.4	3.74	0.7	
	80/80	9.1	1.4	0.4		17.0	0.5	0.0	
EA5-CoC1	0/0	11.9	1.2	0.0	NiC1S3-ED13	5.4	1.0	0.0	
	80/80	13.9	1.6	1.2		4.7	0.3	0.0	
E50-I	0/0	3.3	1.1	0.0	E50I2-CuN	8.6	1.8	0.0	
	80/80	4.4	2.1	0.0		8.7	1.6	0.0	
E50I-CuN	0/0	4.8	4.3	0.0	E50I1-CuN	6.9	1.5	0.0	
	80/80	7.9	2.6	0.0		6.4	1.7	0.0	

* Capacity values are calculated to sorbent saturation (Sat. Load) and after purging the column with air (Post-Purge).

Ammonia breakthrough curves for the Cu C₄TPP functionalized sorbents are shown in Fig. 22 under dry and humid conditions. Calculated loadings to saturation ($C/C_0 = 1$) are summarized in Table 7. Again, all of the CuC₄TPP functionalized sorbents provided higher saturated loading levels than the carbon control material; however, under dry conditions, the saturated loading levels for all three materials are approximately that of the E50A sorbent. It appears that the addition of this porphyrin has no measureable effect on ammonia retention. Under humid conditions, a trend becomes apparent in the breakthrough data, with ammonia loading increasing with increasing porphyrin content. This may indicate that moisture is required for interactions with copper to occur. The material with the highest porphyrin loading also exhibits an elongation near the top of the breakthrough curve, possibly indicating internal pore diffusion limitations. There is no significant difference in the nitrogen adsorption/desorption isotherm for this material, so this is likely owing to porphyrin interactions rather than bottle necks within the sorbent structure (Figs. 19 and 20). Ammonia removal was higher under humid conditions for the CuC₄TPP functionalized materials (Fig. 22), while E50A and E50 showed the opposite effect (Fig. 12). The observed ammonia interaction here is likely a combination of the interactions with the copper metalloporphyrin and the surface hydroxyl groups of the organosilicate sorbent. Under both dry and humid conditions, all ammonia initially adsorbed onto the materials elutes when purged with clean air, indicating ammonia is physically adsorbed and/or loosely bonded.

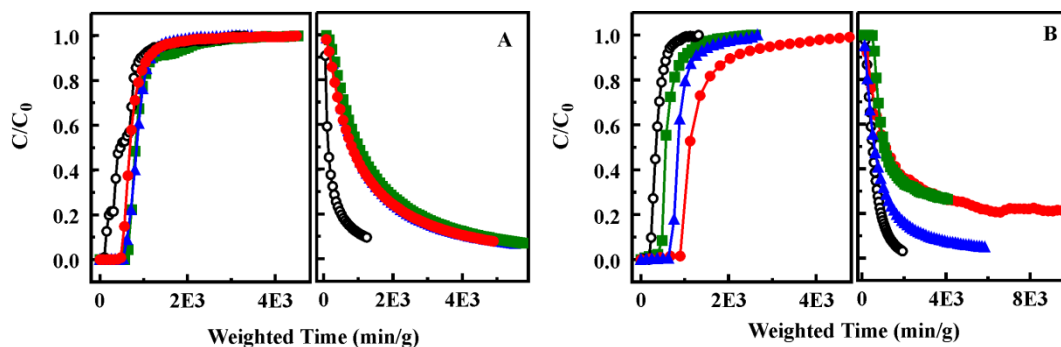


Fig. 22 — Ammonia breakthrough for the Cu C₄TPP materials under dry (A) and humid (B) RH conditions. BPL/Zn/TEDA (black), EA2-CuC (green), E50A10-CuC (red), and E50A5-CuC (blue).

A series of isocyanate functionalized materials was modified using Cu N₄TPP. As with the other porphyrin functionalized sorbents, this series shows higher saturated loading than the control carbon material. Under dry conditions, the highest concentration of porphyrin (E50I10-CuN) provides the greatest ammonia removal (Table 7). The shape of the breakthrough curve at this porphyrin loading level is also distinctly different from that for the lower loading levels (Fig. 23). Under humid conditions, the saturated loading level is significantly reduced for all three materials, and ammonia breakthrough on E50I10-CuN is of a similar form to that of the other two sorbents. As with many of the other sorbents evaluated, all ammonia initially adsorbed elutes from these materials under purge.

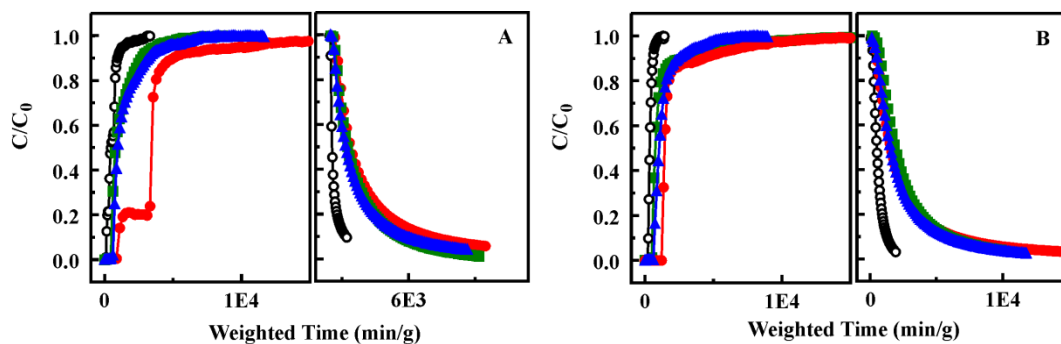


Fig. 23 — Ammonia breakthrough for the Cu N₄TPP materials under dry (A) and humid (B) RH conditions. BPL/Zn/TEDA (black), E50I10-CuN (red), E50I5-CuN (blue) and E50I-CuN (green).

The final material evaluated was the co-condensed EA5 sorbent with Co C₁TPP. This sorbent was developed for potential application to the capture of sulfur dioxide, but was evaluated on challenge by all compounds. Under dry conditions, the sorbent retained no ammonia following purge (Fig. 24). Under humid conditions, the material retained 1.2 mol/kg making it competitive with the EA5-CuD sorbent.

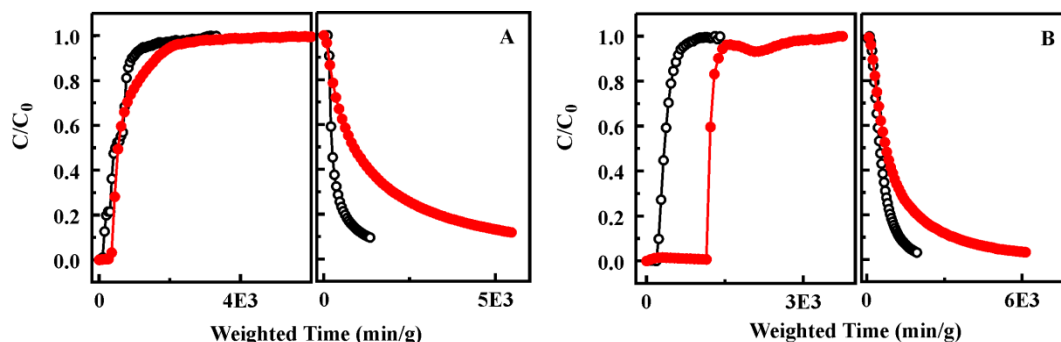


Fig. 24 — Ammonia breakthrough for the Co C₁TPP material under dry (A) and humid (B) RH conditions. BPL/Zn/TEDA (black) and EA5-CoC1 (red).

Ammonia Detection

Materials appropriate for use in ammonia removal applications were expected to show a strong interaction between the metalloporphyrin component of the construct and the target as there was little interaction between the scaffold and the target (Fig. 12). Fluorescence screening was used to provide insight into this interaction. The interaction of ammonia with the coordinated copper was expected to produce a change in the spectrophotometric characteristics of the sorbents. In addition, a strong interaction between the porphyrin and the target would be expected to produce changes in the spectrophotometric characteristics, which did not relax as the sorbent was allowed to exchange with ambient air.

The sorbents were subjected to two cycles of ammonia exposure (50 ppm) each followed by a period of exposure to laboratory ambient conditions (32% RH, 22 °C). Fluorescence spectra were collected prior to the first exposure, following each exposure, and following ambient air exchange. Figure 25 presents the fluorescence spectra for the CuDIX sorbents as well as calculated difference spectra. Upon exposure of E50A2-CuD to ammonia, the fluorescence difference spectrum indicated an increase in fluorescence intensity around 450 nm with an associated decrease in intensity around 408 nm. The magnitude of this difference intensity decreased following equilibration of the materials with ambient air. The second ammonia exposure achieved a difference intensity that was also partially relaxed upon exposure to ambient air. The fluorescence characteristics of the sorbent following the second ambient air exposure were retained when fluorescence spectra were collected after 24 h of ambient air exposure. Changes in fluorescence for CuC₄TPP and CuN₄TPP were smaller than those observed for CuDIX and relaxed completely upon exposure to ambient air (Figs. 26 and 27).

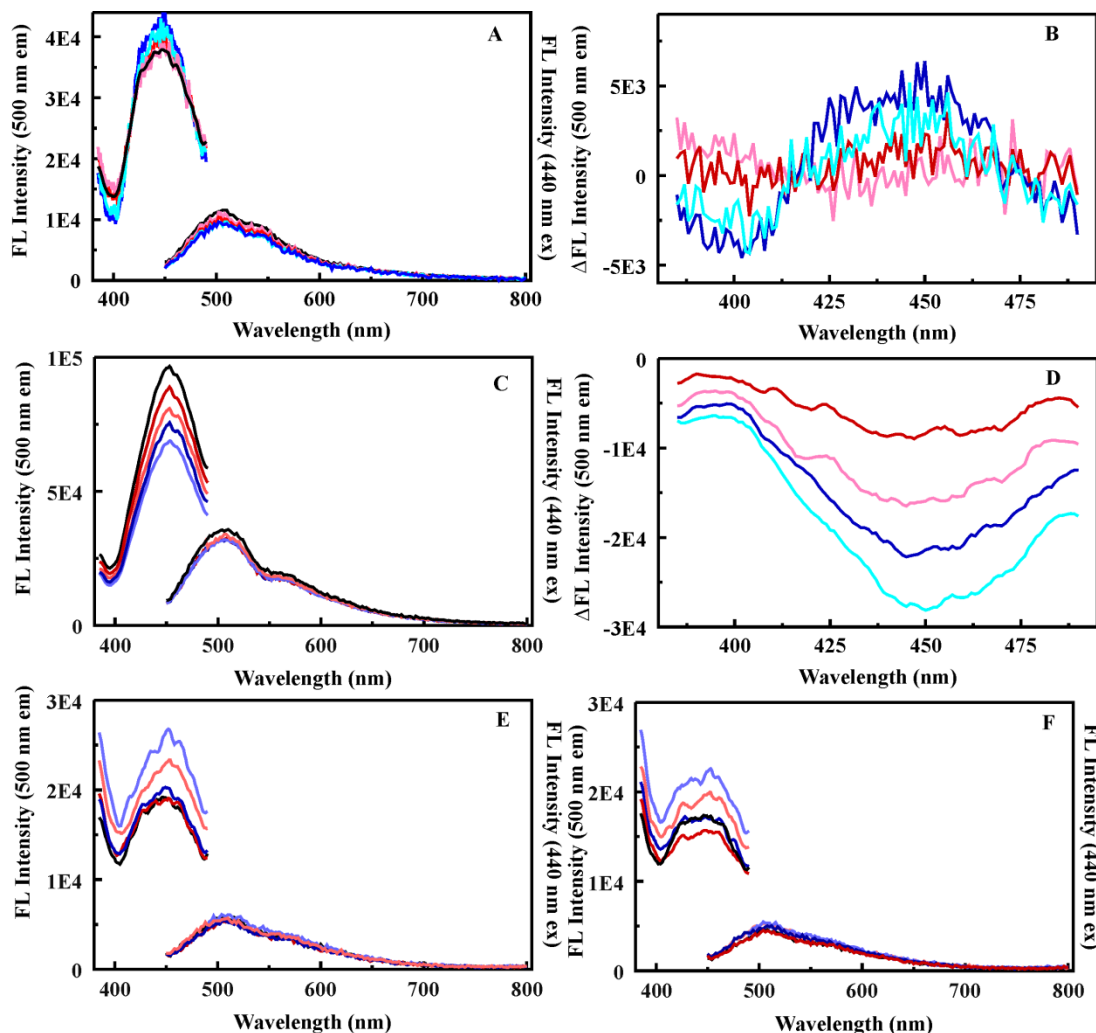


Fig. 25 — Fluorescence excitation (500 nm emission) and emission (440 nm excitation) spectra for CuDIX functionalized sorbents prior to (black) and following the first exposure to 50 ppm ammonia (pink), the first relaxation (red), the second exposure to ammonia (cyan), and the second relaxation (blue). Difference spectra are also presented: E50A1-CuD (A and B), EA5-CuD (C and D), E50A-CuD (E), and E50A5-CuD (F).

The reduction in difference intensity (relaxation of a portion of the changes in the fluorescence spectra) during a five minute re-equilibration period indicates weak interactions between the target and porphyrin. That is, as the ammonia dissociates from the porphyrin, the original spectrophotometric characteristics are recovered. A portion of the changes initially resulting from ammonia exposure was stable for only the CuDIX sorbent. This difference in the sorbents is reflected in the results of the breakthrough experiments. Both the CuC₄TPP and CuN₄TPP sorbents showed loading of ammonia to saturation, which was reversible during purge. The CuDIX sorbents retained some, but not all, of the ammonia captured during the purge step. These similarities tend to indicate that fluorescence screening could be used for selection of appropriate porphyrin-functionalized sorbent candidates prior to extensive breakthrough testing.

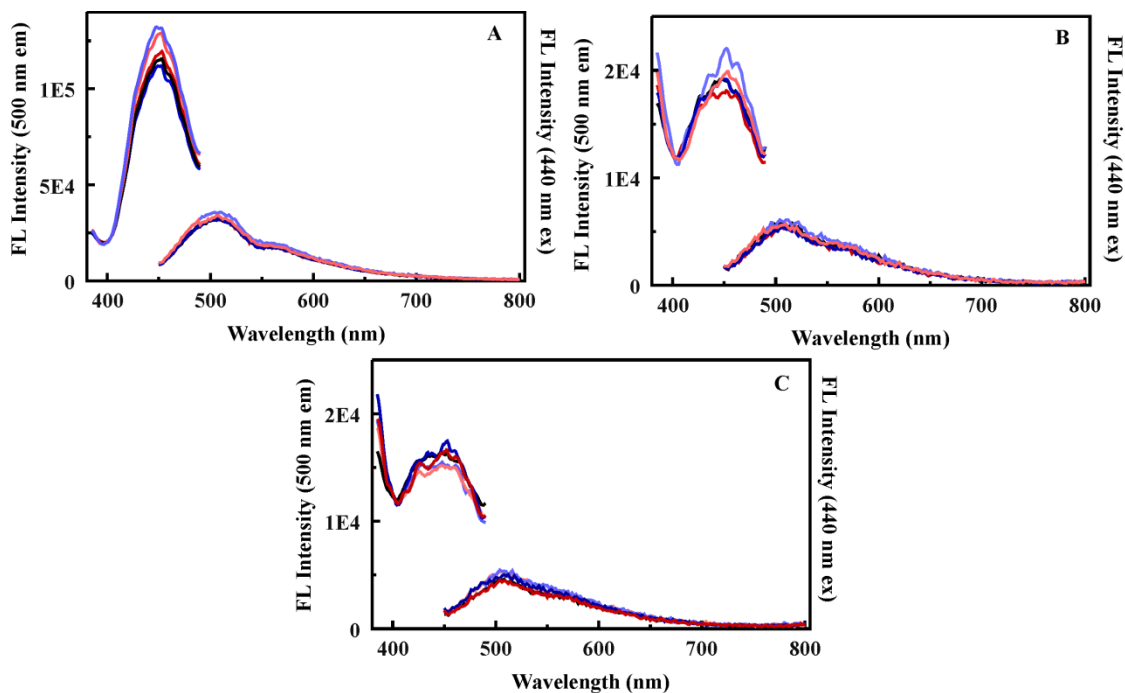


Fig. 26 — Fluorescence excitation (500 nm emission) and emission (440 nm excitation) spectra for CuC_4TPP functionalized sorbents prior to (black) and following the first exposure to 50 ppm ammonia (pink), the first relaxation (red), the second exposure to ammonia (cyan), and the second relaxation (blue): EA2-CuC (A), E50A5-CuC (B), E50A10-CuC (C).

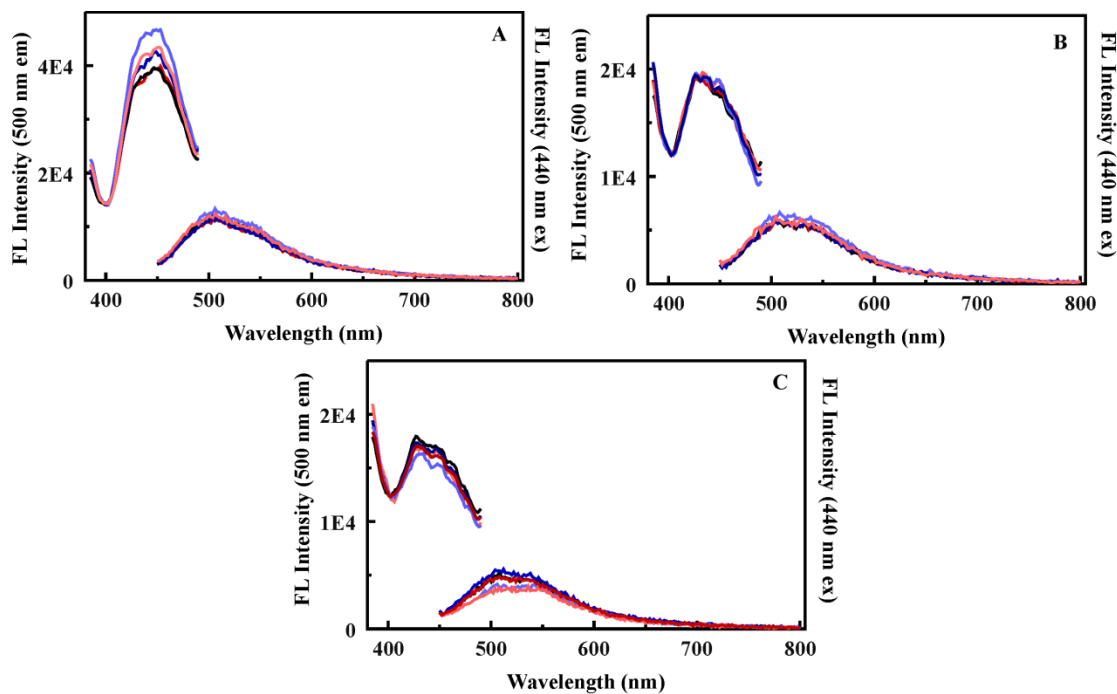


Fig. 27 — Fluorescence excitation (500 nm emission) and emission (440 nm excitation) spectra for CuN_4TPP functionalized sorbents prior to (black) and following the first exposure to 50 ppm ammonia (pink), the first relaxation (red), the second exposure to ammonia (cyan), and the second relaxation (blue): E50I-CuN (A).

Other Targets, Capture and Detection

Loading capacities for cyanogen chloride, sulfur dioxide, and octane are provided in Table 8. To further evaluate the utility of the spectrophotometric characteristics of these materials, fluorescence spectra were collected as described above using sulfur dioxide and octane as targets. The materials described here were not designed with the capture of these targets in mind. Sulfur dioxide was retained only at low loading levels by the sorbents during breakthrough experiments and was desorbed during the purge step for all of the sorbents. Fluorescence response to this target reflected this transient interaction (Fig. 28). Octane retention during breakthrough experiments was significant for several of the sorbents evaluated. The fluorescence response of the sorbents to this target reflect an interaction between the target and the porphyrin as well as the observed retention of octane during sorbent purge (Fig. 29).

Table 8 — Calculated Target Loading Capacities* – Cyanogen Chloride, Sulfur Dioxide, and Octane

		Cyanogen Chloride			Sulfur Dioxide			Octane		
		Mass	Sat. Load	Post-Purge	Mass	Sat. Load	Post-Purge	Mass	Sat. Load	Post-Purge
Sample	RH	mg	mol/kg	mol/kg	mg	mol/kg	mol/kg	mg	mol/kg	mol/kg
BPL/Zn/TEDA	0/0	21.8	1.2	0.7	23.6	0.3	0.0	29.3	3.3	2.7
	80/80	20.9	2.1	2.0	20.1	0.8	0.5	18.1	2.9	2.2
E50	0/0	8.6	0.5	0.1	7.8	0.1	0.0	6.9	3.8	1.8
	80/80	5.3	0.2	0.1	5.9	0.1	0.0	8.5	0.4	0.3
E50-A	0/0	4.7	2.0	1.8	7.1	1.0	0.0	6.0	1.6	0.5
	80/80	5.0	2.8	2.7	6.3	1.1	0.0	2.8	1.0	0.8
EA5-CuD	0/0	13.9	0.4	0.3	14.9	0.4	0.2	10.8	0.9	0.4
	80/80	9.1	0.5	0.3	12.8	0.7	0.6	10.3	0.2	0.2
E50A5-CuD	0/0	6.9	0.7	0.3	5.3	0.1	0.0	9.7	1.7	0.6
	80/80	5.3	0.4	0.4	5.4	0.2	0.0	3.4	0.0	0.8
E50A-CuD	0/0	10.0	0.5	0.1	6.6	0.2	0.0	10.9	1.6	0.1
	80/80	4.1	0.3	0.1	9.5	0.1	0.0	8.5	0.1	0.4
E50A1-CuD	0/0	6.4	0.5	0.2	8.6	0.1	0.0	6.0	1.1	0.3
	80/80	5.8	0.9	0.8	7.9	0.2	0.0	2.8	0.1	0.3
EA2-CuC	0/0	15.8	0.3	0.0	13.5	0.0	0.0	12.9	1.1	0
	80/80	11.0	0.1	0.0	13.0	0.0	0.0	9.8	0.1	0.1
E50A5-CuC	0/0	11.5	0.3	0.0	9.4	0.0	0.0	8.6	1.6	0.4
	80/80	14.1	0.1	0.0	11.1	0.0	0.0	11.6	0.1	0.1
E50A10-CuC	0/0	12.6	0.5	0.2	13.2	0.0	0.0	6.4	1.7	0.5
	80/80	11.0	0.1	0.1	8.1	0.1	0.0	9.4	0.1	0.0
E50-I	0/0	4.7	0.9	0.7	4.2	0.1	0.0	6.8	9.2	7.6
	80/80	5.5	0.4	0.3	4.6	0.1	0.0	4.3	0.8	0.6
E50I10-CuN	0/0	6.7	0.9	0.4	7.0	0.1	0.0	8.5	1.9	0.7
	80/80	11.8	0.2	0.1	9.4	0.2	0.1	7.7	0.2	0.2
E50I5-CuN	0/0	6.9	1.3	0.9	8.1	0.1	0.0	5.1	2.4	0.8
	80/80	9.9	0.1	0.0	3.7	0.2	0.0	6.6	0.2	0.0
E50I-CuN	0/0	6.4	1.0	0.5	8.3	0.1	0.0	8.6	1.9	0.6

* Capacity values are calculated to sorbent saturation (Sat. Loading) and after purging the column with air (Post-Purge).

Table 8 — Calculated Target Loading Capacities (continued)*

	80/80	10.1	0.4	0.3	5.4	0.1	0.0	7.3	0.2	0.1
EA5-CoC1	0/0	13.6	0.5	0.2	10.1	0.1	0.0	15.9	0.9	0.4
	80/80	14.2	0.2	0.1	16.7	0.0	0.0	10.3	0.2	0.2
EB-Cu2D	0/0	12.5	0.6	0.1	9.7	0.1	0.0	--	--	--
	80/80	5.1	0.2	0.1	19.5	0.0	0.0	--	--	--
EB-Cu1D	0/0	13.7	0.4	0.1	11.8	0.0	0.0	--	--	--
	80/80	7.5	0.4	0.3	12.4	0.1	0.0	--	--	--
EC-Cu2D	0/0	11.0	0.5	0.1	8.6	0.0	0.0	--	--	--
	80/80	5.7	0.3	0.1	14.0	0.1	0.0	--	--	--
EC-Cu1D	0/0	12.5	0.4	0.1	11.8	0.0	0.0	--	--	--
	80/80	16.9	0.1	0.1	17.8	0.1	0.0	--	--	--
NiC1S3-ED13	0/0	7.1	0.3	0.2	4.8	0.0	0.0	5.1	0.9	0.3
	80/80	5.4	0.1	0.0	1.4	0.3	0.0	5.7	0.5	0.2

* Capacity values are calculated to sorbent saturation (Sat. Loading) and after purging the column with air (Post-Purge).

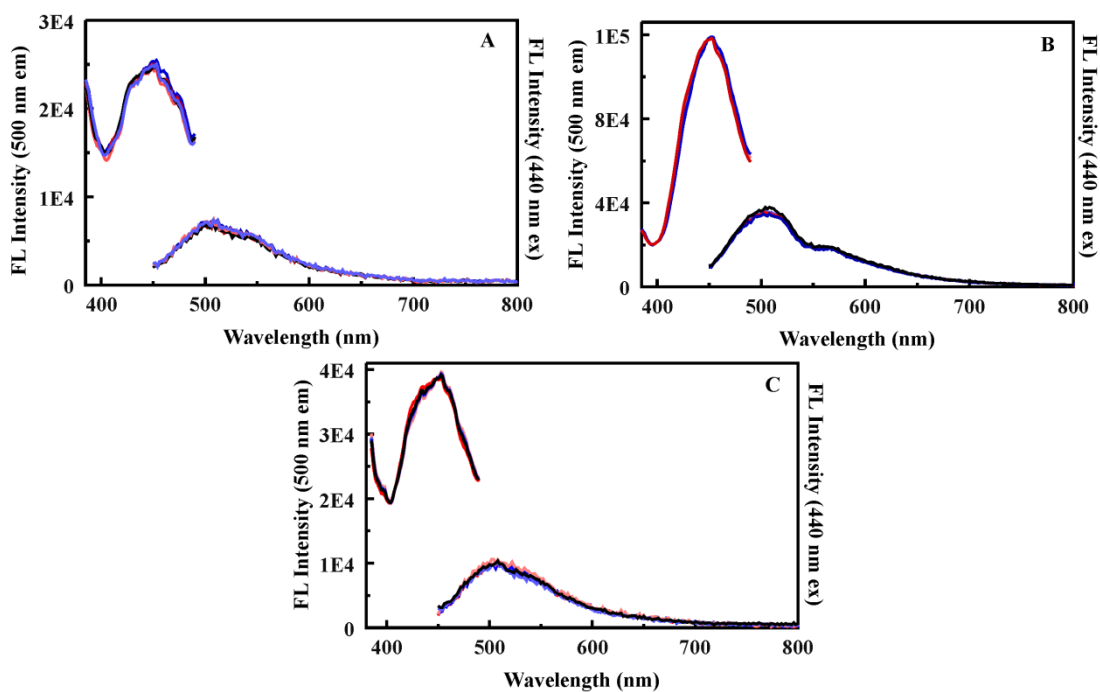


Fig. 28 — Fluorescence excitation (500 nm emission) and emission (440 nm excitation) spectra for CuC_4TPP functionalized sorbents prior to (black) and following the first exposure to 50 ppm sulfur dioxide (pink), the first relaxation (red), the second exposure to sulfur dioxide (cyan), and the second relaxation (blue): EA2-CuA (A), E50A5-CuB (B), E50A10-CuC (C).

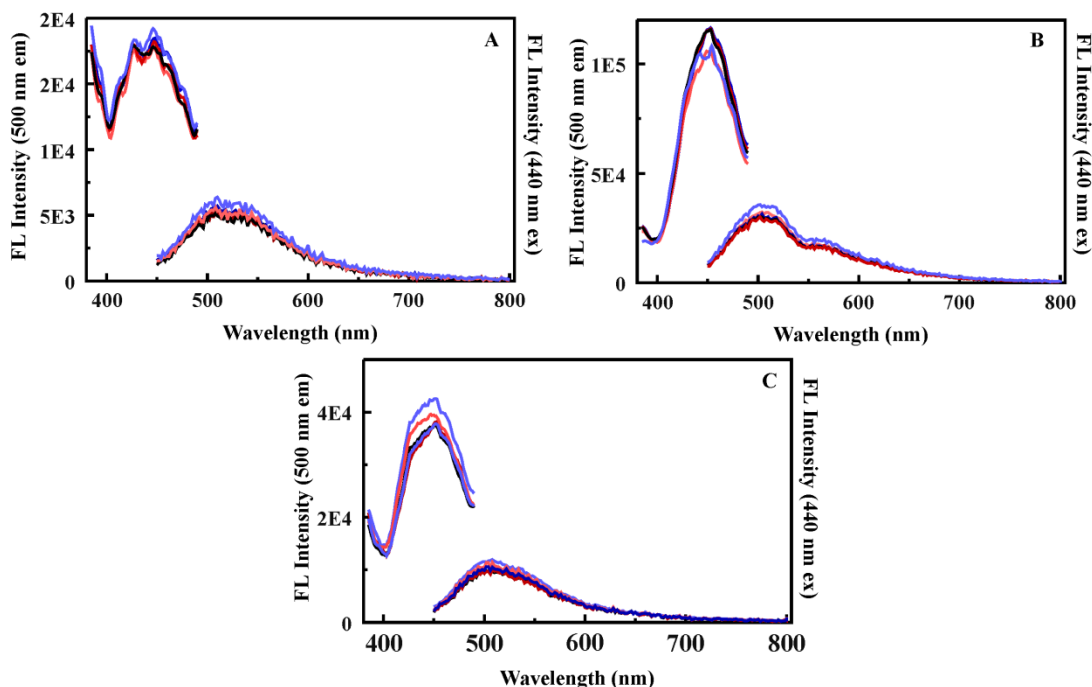


Fig. 29 — Fluorescence spectra for E50A-CuD (A), EA2-CuC (B), and E50I-CuN (C) excitation (500 nm emission) and emission (440 nm excitation) spectra for CuC₄TPP functionalized sorbents prior to (black) and following the first exposure to 50 ppm octane (pink), the first relaxation (red), the second exposure to octane (cyan), and the second relaxation (blue): EA2-CuC (A), E50A5-CuC (B), E50A10-CuC (C).

Breakthrough of chlorine and nitric oxide was evaluated for columns of Cu DIX and Co C₁TPP modified materials (Fig. 30). Chloride retention by the Cu DIX modified material was similar to that of the base scaffold (E50-A). The co-condensed sorbent retained little of either target. Retention of nitric oxide was significantly improved in the Co C₁TPP modified material (Table 9). This retention is the result of the metalloporphyrin used as the same scaffold modified using Cu DIX (EA5-CuD) did not retain significant amounts of nitric oxide. Here, both the porphyrin structure and the incorporated metal have been changed. It is not clear whether one or the other or both of these modifications is responsible for the improvement.

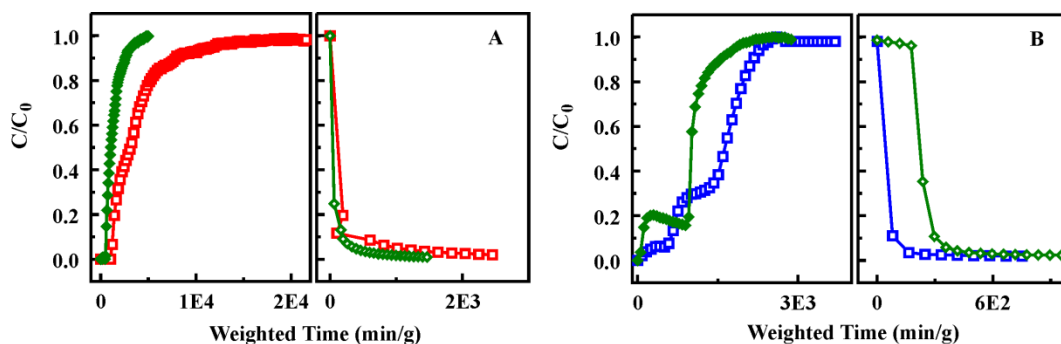


Fig. 30 — Chlorine (A) and nitric oxide breakthrough for organosilicates under dry conditions: EA5-CuD (green), E50A-CuD (red), EA5-CoC1 (blue).

Table 9 — Calculated Target Loading Capacities* – Chlorine and Nitric Oxide

		Chlorine			Nitric Oxide		
		Mass	Sat. Load	Post-Purge	Mass	Sat. Load	Post-Purge
Sample	RH	mg	mol/kg	mol/kg	mg	mol/kg	mol/kg
EA5-CuD	0/0	16.0	0.4	0.4	17.8	0.7	0.4
E50A-CuD	0/0	5.2	1.1	1.1	--	--	--
EA5-CoC1	0/0	--	--	--	12.7	2.4	2.4
NiC1S3-ED13	0/0	5.9	2.0	2.0	--	--	--

* Capacity values are calculated to sorbent saturation (Sat. Loading) and after purging the column with air (Post-Purge).

Morphological Considerations

To determine the impact of sorbent morphology on the performance of porphyrin functionalized materials, variants incorporating DIX with copper were prepared. As seen in Fig. 31, the materials offered differences in porosity with EB sorbents showing greater order and a narrower pore size distribution and the EC sorbents providing a wider pore size distribution. Surface areas for the materials were similar at 1,070 m²/g for EB sorbents and 925 m²/g for EC sorbents. Pore volume was larger in the EB sorbents (1 cm³/g vs 0.72 cm³/g), and the pore size of the EC sorbents was smaller than that of the EB sorbents (60 Å vs 76 Å). Due to the discrepancies noted for performance of copper (I) and copper (II) in the phosgene capture experiments, both variants were prepared for this study.

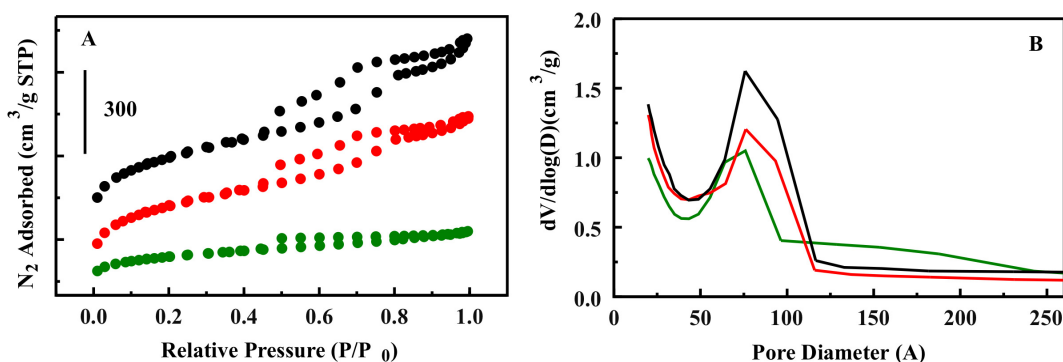


Fig. 31 — Morphological characterization for the EB and EC materials. (A) Nitrogen adsorption/desorption isotherms. (B) Pore size distribution: EB-Cu1D (red), EB-Cu2D (black), and EC-Cu1D and EC-Cu2D (green).

Loading levels for the ammonia, cyanogen chloride, and sulfur dioxide both before and after column purge are summarized in Tables 7 and 8. Figure 32 presents the breakthrough curves for each sorbent challenged by each of the targets under dry and humid (80% RH) conditions. In the absence of morphological contributions, the performance of the four materials would be similar to that observed for the EA5-CuD (Fig. 22; Tables 7 and 8) with possible variations between copper (I) and copper (II). As in

the case of EA5-CuD, the EB and EC materials did not bind or retain significant amounts of cyanogen chloride or sulfur dioxide. Significant ammonia capacity was noted. The CuDIX and other copper metalloporphyrin functionalized sorbents show greater ammonia capacity under dry conditions than under humid conditions. Interestingly, copper (I) sorbents showed greater capacity than those functionalized with copper (II). Unfortunately, there was insufficient material to complete a full evaluation of these sorbents. The high capacity noted for EB-Cu1D under humid conditions, however, indicates the potential for greater capacity than that noted for EA5-CuD.

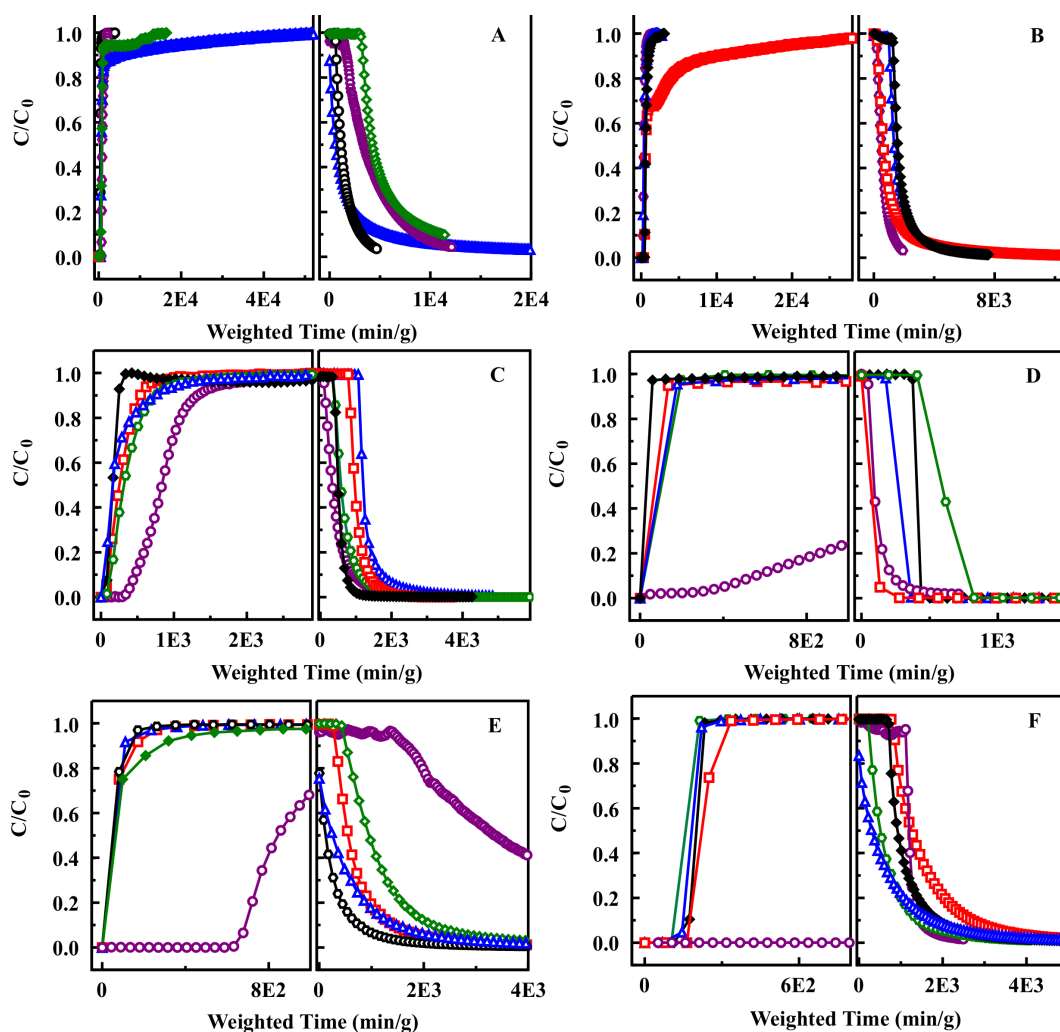


Fig. 32 — Target breakthrough profiles for the ordered and disordered materials: ammonia (A, dry; B, 80% RH), cyanogen chloride (C, dry; D, 80% RH), and sulfur dioxide (E, dry; F, 80% RH) where EB-Cu1D (red), EB-Cu2D (green), EC-Cu1D (black), and EC-Cu2D (blue). The breakthrough for the BPL/Zn/TEDA is shown in purple.

NiC₁S₃TPP on ED13

The ED13 sorbent combines both ethane and diethylbenzene bridging groups. This combination offers advantages in the capture of aromatic compounds such as nitroenergetics [26,27,45] and has been shown to provide binding affinity for organophosphate targets [28,29,43]. Synthesis of the sorbent is

described [above](#). Little retention of ammonia, cyanogen chloride, sulfur dioxide, or octane was noted for the sorbents. Chlorine retention for the sorbent was higher (2 mol/kg) than that noted for other materials. The factors contributing to this result are not clear (Fig. 33). Loading levels for ammonia, cyanogen chloride, sulfur dioxide, octane, and chlorine both before and after column purge are summarized in Tables 7, 8, and 9. Figures 34 and 35 present the breakthrough curves for targets and compare the performance of the NiC₁S₃-ED13 sorbent to that of MM3. The MM3 sorbent offers a similar combination of ethane and diethylbenzene bridging groups with no porphyrin or metal functionality.

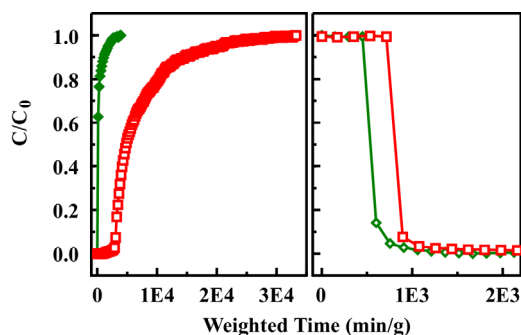


Fig. 33 — Chlorine breakthrough for sorbents under dry conditions: MM3 (green) and NiC₁S₃-ED13 (red).

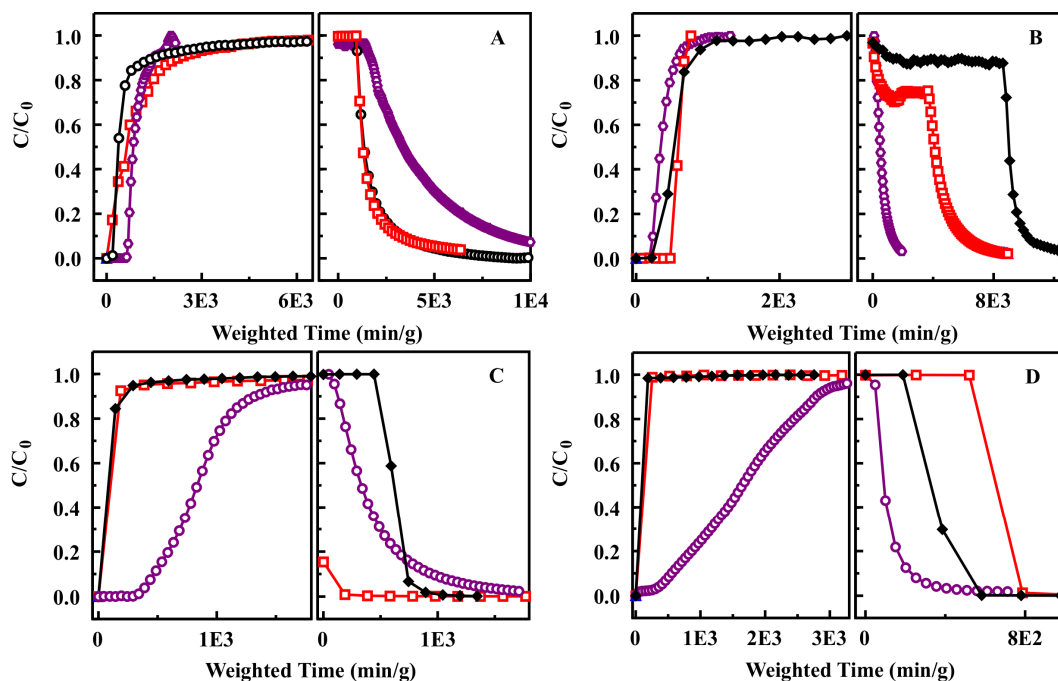


Fig. 34 — Target capture by the NiC₁S₃TPP functionalized sorbent. Breakthrough curves for ammonia (A, dry; B, 80% RH) and cyanogen chloride (C, dry; D, 80% RH): NiC₁S₃-ED13 (black) and MM3 (red). The breakthrough for the BPL/Zn/TEDA is shown in purple.

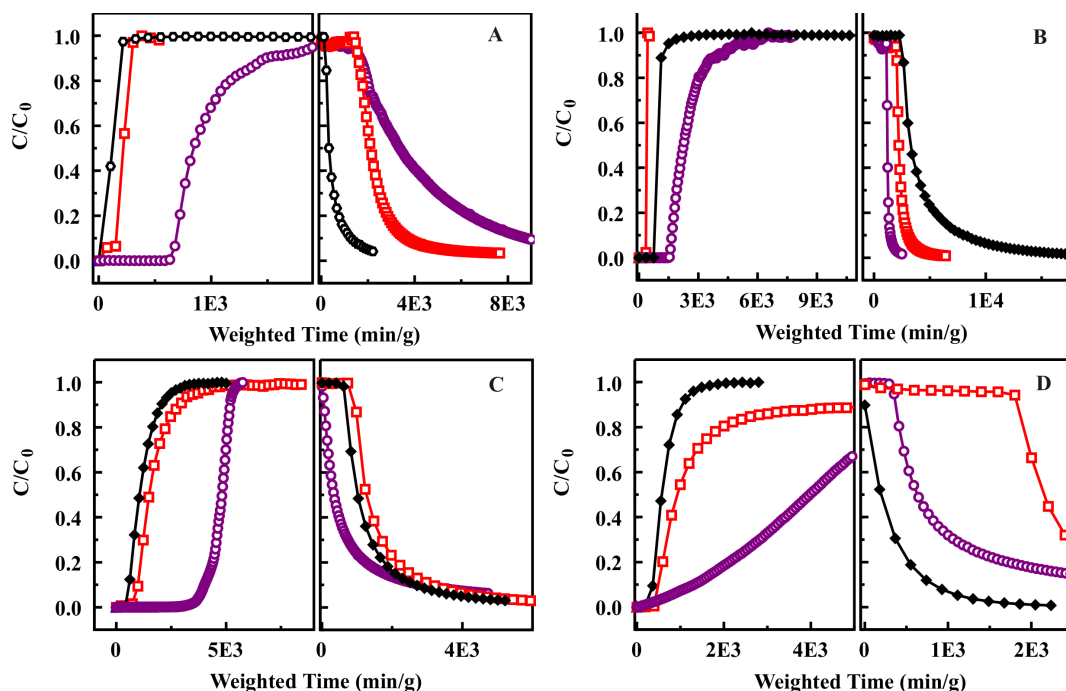


Fig. 35 — Target capture by the $\text{NiC}_1\text{S}_3\text{TPP}$ functionalized sorbent. Breakthrough curves for sulfur dioxide (A, dry; B, 80% RH) and octane (C, dry; D, 80% RH): $\text{NiC}_1\text{S}_3\text{-ED13}$ (black) and MM3 (red). The breakthrough for the BPL/Zn/TEDA is shown in purple.

Zirconium

Mesoporous zirconium-silicate materials were synthesized for their potential in removal of sulfur dioxide. Zirconium hydroxide $[\text{Zr}(\text{OH})_4]$ materials have been shown to provide effective capture of SO_2 from streams of air [40,56]. The $\text{Zr}(\text{OH})_4$ used was a commercially available powder with a measured surface area of $365 \text{ m}^2/\text{g}$ and pore volume of $0.24 \text{ cm}^3/\text{g}$. Investigations determined that terminal hydroxyl groups specifically reacted with SO_2 molecules; bridging hydroxyl and oxide groups did not contribute to removal. Mesoporous silicates containing Zr from a zirconium *n*-propoxide precursor provide the potential for materials with higher surface areas and more accessible mesopores than the commercial $\text{Zr}(\text{OH})_4$ powder.

Materials Synthesis

The Zr-MCM-41-type silicate is synthesized using an adaptation of a published protocol combining zirconium *n*-propoxide and tetraethoxysilane precursors with cetyltrimethylammonium chloride surfactant [57]. A molar ratio of eight Si:Zr was used in the reaction mixture, though this does not necessarily result in a product having the same ratio. Unlike the protocols described in the reference, a relatively low reaction temperature of 90°C was applied, and no post-synthesis calcination was performed. This increases the possibility of forming Zr-OH groups and helps to avoid unwanted crystalline phases. Surfactant was extracted with acidic alcohol. The mesoporous product had a notably greater surface area than that reported for zirconium hydroxide powder and a narrow pore size distribution (Table 2; Fig. 36).

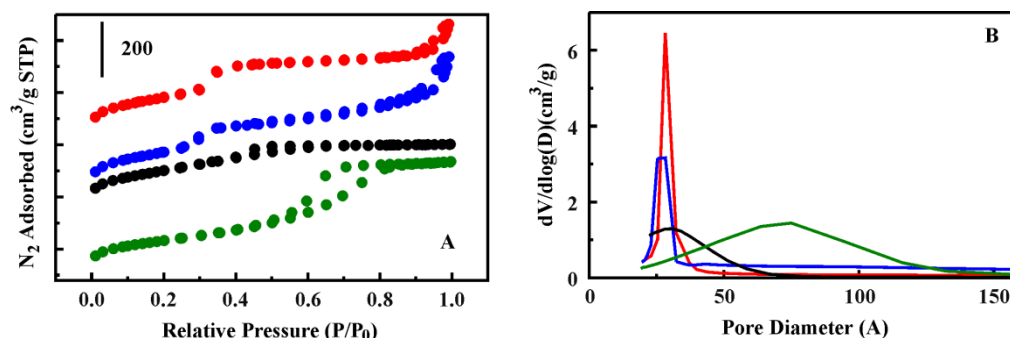


Fig. 36 — Morphological characterization for the Zr materials. (A) Nitrogen adsorption/desorption isotherms. (B) Pore size distribution: ZrM41 (red), ZrM41-A (blue), ZrMP4 (black), and ZrMP4-A (green).

An alternative type of material has also been prepared through adaptation of a synthesis for mesoporous silica monoliths [58]. Zirconium *n*-propoxide is combined with tetramethoxysilane again using a molar ratio of eight for Si:Zr. In this case, the ratio should be retained in the product, initially obtained as a gel. Pluronic P123 is used as the template in combination with the micelle swelling agent, mesitylene. Materials found to be highly mesoporous when synthesized with a pure silica composition were microporous when the zirconium oxide precursor was added. A higher concentration of Pluronic P123 was required to obtain uniform mesopores (6 g rather than 4 g). A product prepared without mesitylene was found to have a greater mesopore size than those that included the swelling agent (Fig. 36). Arene compounds, like mesitylene, can form a complex with Zr. If this occurred during a synthesis, it could interfere with templating of the mesopores.

Target Adsorption

Though sulfur dioxide was the intended target for the zirconium sorbents, adsorption of ammonia, CK, and octane were also evaluated. The materials did not retain significant amounts of any of the targets (Table 10; Figs. 37 and 38). These materials rely on interaction of the target with the zirconium sites. There are two simple possibilities for the failure of the sorbents. First, the zirconium sites may not be available for interaction. If the sites are preferentially incorporated within the pore wall structures rather than on the surfaces, they would be unavailable to the targets. The interaction of targets with the materials in this case would be similar to that observed for E50 (described [above](#)) with differences resulting from morphological variation and hydrophobicity. The Zr sites may alternatively interact tightly with the surface preventing the necessary target interactions. The second possibility is related to the oxidation state of the incorporated zirconium. Treatment with sulfur dioxide was intended to further oxidize the Zr sites, but may not have achieved this goal.

Table 10 — Target Loading Capacities for Zirconium Materials*

Target			BPL/Zn/T	ZrM41	ZrM41-A	ZrMP4	ZrMP4-A
Sulfur dioxide	Dry	Mass (mg)	23.6	6.9	11.1	27.6	24.5
		Sat. Load	0.3	0.8	0	0	0
		Post-Purge	0	0	0	0	0
	80%	Mass (mg)	20.1	6.5	10.0	27.3	25.6
		Sat. Load	0.8	0.1	0.1	0.1	0
		Post-Purge	0.5	0	0	0	0
Ammonia	Dry	Mass (mg)	20.6	9.0	11.4	33.2	20.9
		Sat. Load	0.7	2.8	1.9	2.6	1.5
		Post-Purge	0.4	0.3	0	0	0
	80%	Mass (mg)	22.7	9.8	11.7	32.0	27.1
		Sat. Load	0.5	2.6	1.3	2.6	1.2
		Post-Purge	0	1.1	0	1.5	0.2
Cyanogen chloride	Dry	Mass (mg)	21.8	5.6	9.9	24.4	17.2
		Sat. Load	1.2	0.9	0.6	0.4	0.4
		Post-Purge	0.7	0.3	0.2	0.1	0.1
	80%	Mass (mg)	20.9	8.9	5.2	21.4	19.5
		Sat. Load	2.1	0.1	0.2	0.1	0.1
		Post-Purge	2.0	0	0.1	0.1	0
Octane	Dry	Mass (mg)	29.3	21.9	5.2	21.1	19.6
		Sat. Load	3.3	2.8	1.1	0.9	0.4
		Post-Purge	2.7	2.5	1.1	0.3	0.1
	80%	Mass (mg)	18.1	24.0	7.1	15.0	18.8
		Sat. Load	2.9	2.8	0.2	0.2	0.1
		Post-Purge	2.2	2.8	0.1	0.1	0.0

* Capacity values, provided in mol/kg, are calculated to sorbent saturation (Sat. Load) and after purging the column with air (Post-Purge).

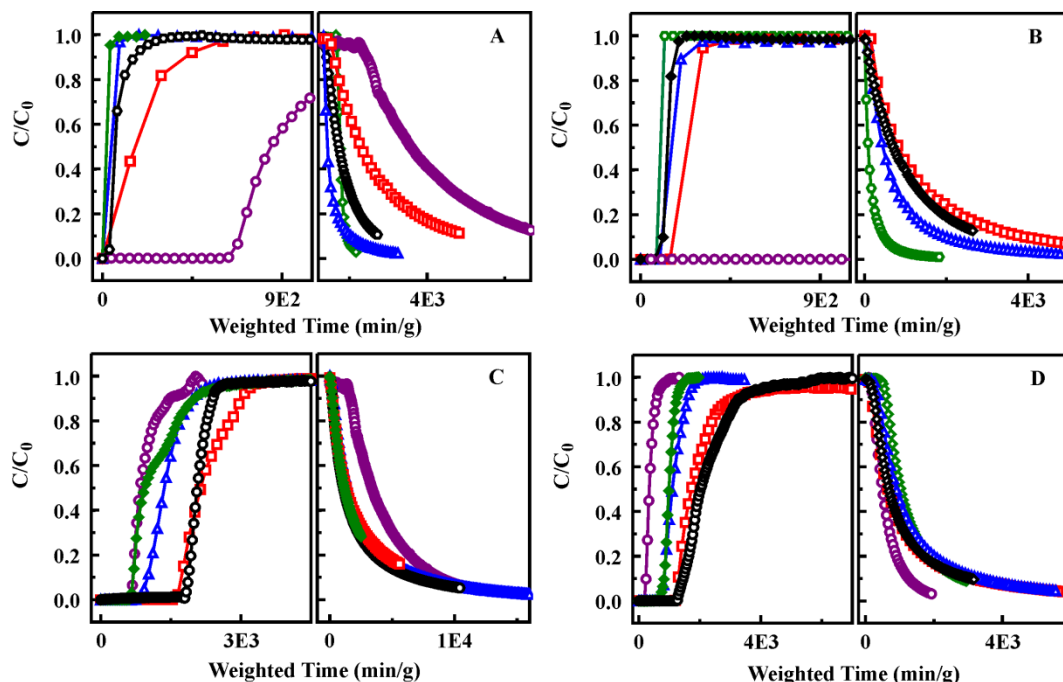


Fig. 37 — Target breakthrough profiles for the Zr materials: sulfur dioxide (A, dry; B, 80% RH) and ammonia (C, dry; D, 80% RH) where ZrM41 (red), ZrM41-A (blue), ZrMP4 (black), and ZrMP4-A (green). The breakthrough for the BPL/Zn/TEDA is shown in purple.

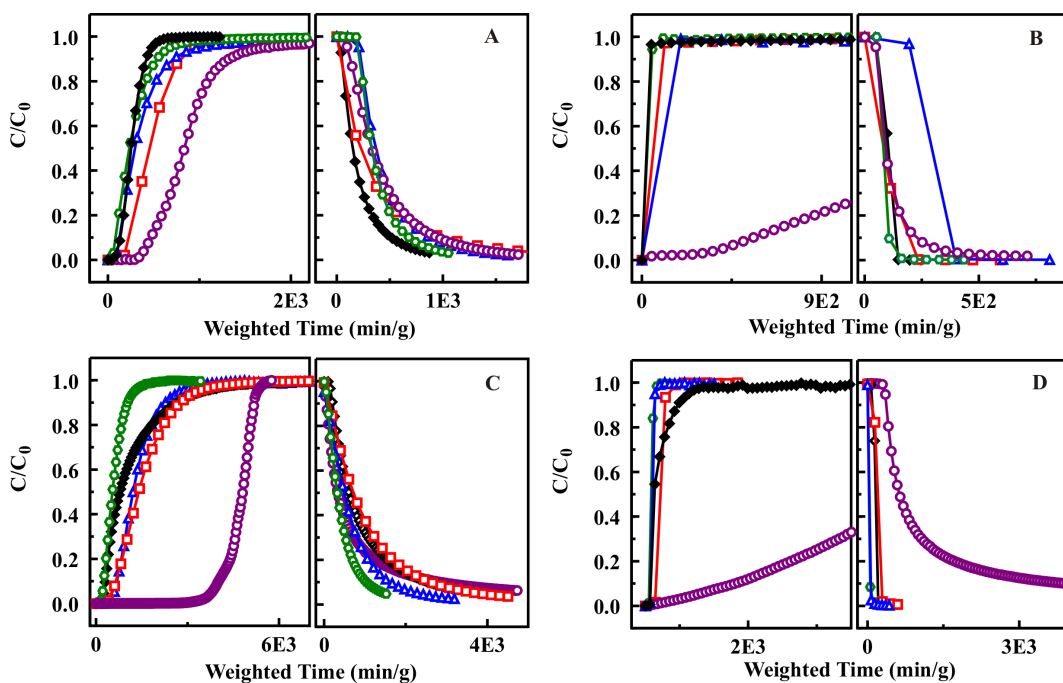


Fig. 38 — Target breakthrough profiles for the Zr materials: cyanogen chloride (E, dry; F, 80% RH) and octane (G, dry; H, 80% RH) where ZrM41 (red), ZrM41-A (blue), ZrMP4 (black), and ZrMP4-A (green). The breakthrough for the BPL/Zn/TEDA is shown in purple.

Metal Incorporation

It was also of interest to evaluate the contributions of metals coordinated with various groups on the surfaces of the sorbents. The hydroxyl groups of the silicates, for example, can interact with metal ions. This has implications both for design of materials and for understanding other materials described here. In the metalloporphyrin materials, for example, metals were incorporated by reflux following the covalent immobilization of the porphyrin within the porous scaffold. During this process, coordination of metals with free hydroxyl sites would also be expected. It is also possible to incorporate metals into the sorbents using coordination sites provided by other functional groups, specifically, N,N'-bis[3-(trimethoxysilyl)propyl]ethylenediamine (EDA) and N-2-(aminoethyl)-3-aminopropyltrimethoxysilane (AEA) were evaluated. EDA provides a diamine group in a bridging capacity in the sorbent material, while AEA provides a pendant diamine group. These sorbents were synthesized with copper and zinc in place to direct the assembly of the materials providing preference for binding of the particular metal [59].

Materials Synthesis

For evaluation of hydroxyl associated metal incorporation, the E50 sorbent described [above](#) was used. The sorbent was reflux in an aqueous solution of 1 M CuCl₂, MgCl₂, or CoCl₂ overnight. It was then collected by vacuum filtration, rinsed, and dried at 110 °C overnight. Synthesis of AEA and EDA sorbents was adapted from published protocols [60]. EDA materials were synthesized by dissolving BTE (3.2 g) in 0.01 M HCl (2, 3, or 4 g). Pluronic P123 (0.65 g) was added to the mixture and allowed to fully dissolve. The metal chelating group, EDA (0.11 g) was then added with either zinc acetate (0.04 g) or copper chloride (0.04 g) and a vacuum was pulled on the solutions for 24 h. The tube was then sealed and placed at 100 °C for 0.5 h followed by 60 °C for 24 h. Sorbents were refluxed twice in acidified ethanol to remove the surfactant and soaked overnight in an ammonium hydroxide solution. After rinsing, metals were reincorporated through refluxing in a 0.1 M solution of either copper chloride or zinc acetate. AEA materials were synthesized using the same protocol in which the EDA precursor was replaced by the AEA precursor (0.07 g). Sorbent naming includes a number indicative of the HCl variation used during synthesis; CuEDA(3) indicates three grams of HCl.

Morphological characteristics for the AEA and EDA sorbents are summarized in Table 2 and nitrogen adsorption behavior is presented in Fig. 39. Pore size distributions were much wider and larger for zinc materials as shown. Average pore diameters ranged from 64 to 250 Å for these materials while pore diameters in the copper materials ranged from 50 to 92 Å. While pore volumes in the copper and zinc materials were similar (0.41 to 0.87 cm³/g), surface area tended to be smaller in the zinc sorbents (190 to 716 m²/g for zinc vs 512 to 716 m²/g for copper).

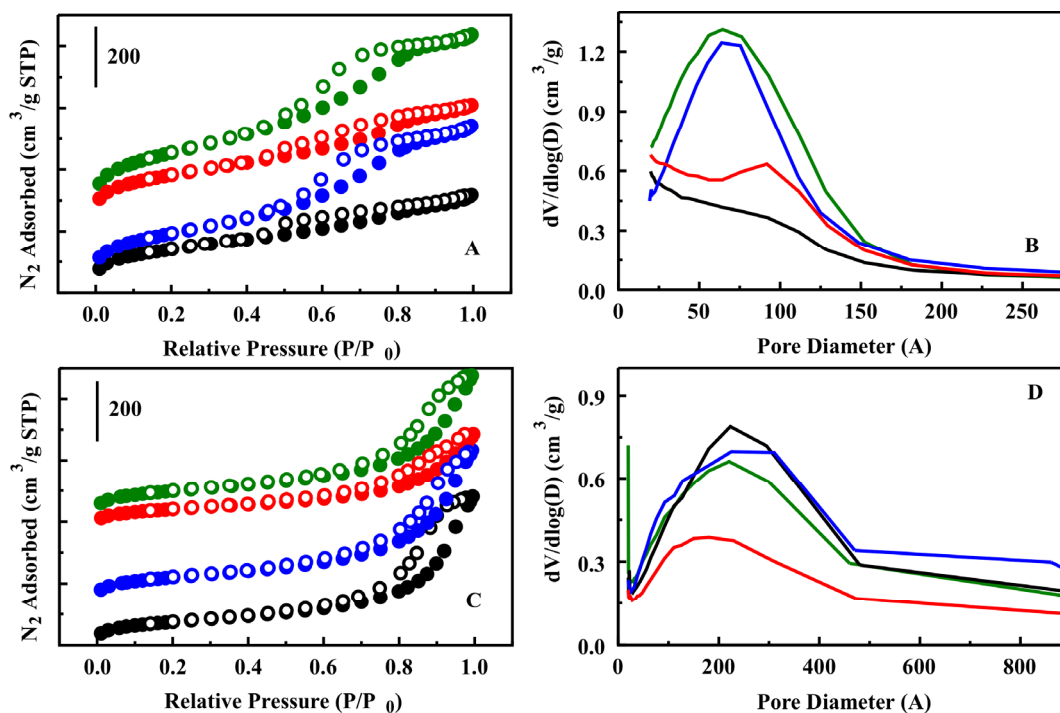


Fig. 39 — Material characteristics for the EDA and AEA materials. (A) Nitrogen sorption isotherms for copper materials (Cu EDA(3), black; Cu EDA(4), blue; Cu AEA(3), red; Cu AEA(4), green. Cu EDA(4) offset by 40; CuAEA(3) offset by 240; CuAEA(4) offset by 260. (B) Pore size distributions for the copper materials. (C) Nitrogen sorption isotherms for the zinc materials (Zn EDA(2), black; Zn EDA(4), blue; Zn AEA(2), red; Zn AEA(4), green). Zn EDA(4) offset by 140; Zn AEA(2) offset by 390; Zn AEA(4) offset by 420. (D) Pore size distributions for the zinc materials.

Target Capture

Copper and zinc were selected based on their known utility and former incorporation into ASZM-TEDA sorbent materials. As shown above, copper was found to provide capture of both ammonia and phosgene when incorporated as a metalloporphyrin construct. Zinc, cobalt, and magnesium were also shown to offer utility in air purification experiments using MOF materials. Association of the metals with hydroxyl groups on the sorbent surfaces resulted in increased initial retention of ammonia, but did not result in post-purge retention of the target (Table 11 and Fig. 40). Similar results were obtained for cyanogen chloride (Fig. 40) and no significant retention of sulfur dioxide was noted (Fig. 41). Octane retention was increased slightly for all of the metal refluxed materials; however, the reasons for this difference are not clear (Fig. 41 and Table 12). Incorporation of zinc and copper through the use of EDA and AEA chelating groups did not result in performance improvements over the base E50 sorbent for any of the evaluated targets (Table 11 and Figs. 42 through 44). It is possible that the coordination geometry in these materials was unfavorable for binding of an additional ligand or that the metals were interacting with both the coordination site and the hydroxyl groups on the sorbent surfaces. The molar concentrations of the metals within the final materials may also be insufficient to cause a significant impact.

Table 11 — Calculated Target Loading Capacities for Metal Modified Materials*

		Ammonia			Cyanogen Chloride			Sulfur Dioxide		
		Mass	Sat. Load	Post-Purge	Mass	Sat. Load	Post-Purge	Mass	Sat. Load	Post-Purge
Sample	RH	mg	mol/kg	mol/kg	mg	mol/kg	mol/kg	mg	mol/kg	mol/kg
BPL/Zn/TEDA	0/0	20.6	0.7	0.4	21.8	1.2	0.7	23.6	0.3	0.0
	80/80	22.7	0.5	0.0	20.9	2.1	2.0	20.1	0.8	0.5
E50	0/0	6.6	4.0	1.9	8.6	0.5	0.1	7.8	0.1	0.0
	80/80	7.3	0.5	0.0	5.3	0.2	0.1	5.9	0.1	0.0
Co E50	0/0	6.4	4.2	1.0	5.8	1.0	0.6	8.5	0.1	0.0
	80/80	8.2	1.1	0.0	11.8	0.1	0.1	9.1	0.3	0.2
Cu E50	0/0	5.0	2.7	0.0	8.8	1.0	0.6	4.2	0.1	0.0
	80/80	5.6	1.2	0.0	8.6	0.2	0.1	6.5	0.3	0.1
Mg E50	0/0	7.1	1.7	0.0	6.6	1.0	0.5	10.4	0.0	0.0
	80/80	7.3	1.6	0.0	8.8	0.0	0.0	7.1	0.1	0.0
Cu EDA(3)	0/0	11.3	1.1	0.0	9.2	0.4	0.1	13.2	0.1	0.0
	80/80	--	--	--	6.6	0.3	0.3	13.5	0.1	0.0
Cu EDA(4)	0/0	9.7	0.8	0.0	12.1	0.4	0.2	11.6	0.0	0.0
	80/80	--	--	--	7.4	0.3	0.2	10.8	0.1	0.0
Cu AEA(3)	0/0	11.9	1.5	0.0	14.9	0.4	0.2	12.4	0.0	0.0
	80/80	--	--	--	5.6	0.2	0.2	14.3	0.1	0.0
Cu AEA(4)	0/0	7.2	1.3	0.0	7.2	0.4	0.2	11.0	0.0	0.0
	80/80	--	--	--	6.7	0.2	0.1	--	--	--
Zn EDA(2)	0/0	8.4	1.3	0.0	9.8	0.4	0.1	10.0	0.1	0.0
	80/80	--	--	--	7.1	0.2	0.2	12.8	0.2	0.0
Zn EDA(4)	0/0	10.3	0.7	0.0	13.6	0.4	0.2	10.6	0.1	0.0
	80/80	--	--	--	9.7	0.4	0.4	13.0	0.2	0.0
Zn AEA(2)	0/0	11.4	0.8	0.0	15.5	0.3	0.1	12.4	0.1	0.0
	80/80	12.8	1.0	0.4	9.4	0.4	0.4	14.5	0.4	0.0
Zn AEA(4)	0/0	10.1	1.1	0.0	12.5	0.5	0.2	12.	0.1	0.0
	80/80	8.7	2.5	1.6	9.3	0.2	0.2	15.8	0.3	0.0

* Capacity values are calculated to sorbent saturation (Sat. Load) and after purging the column with air (Post-Purge).

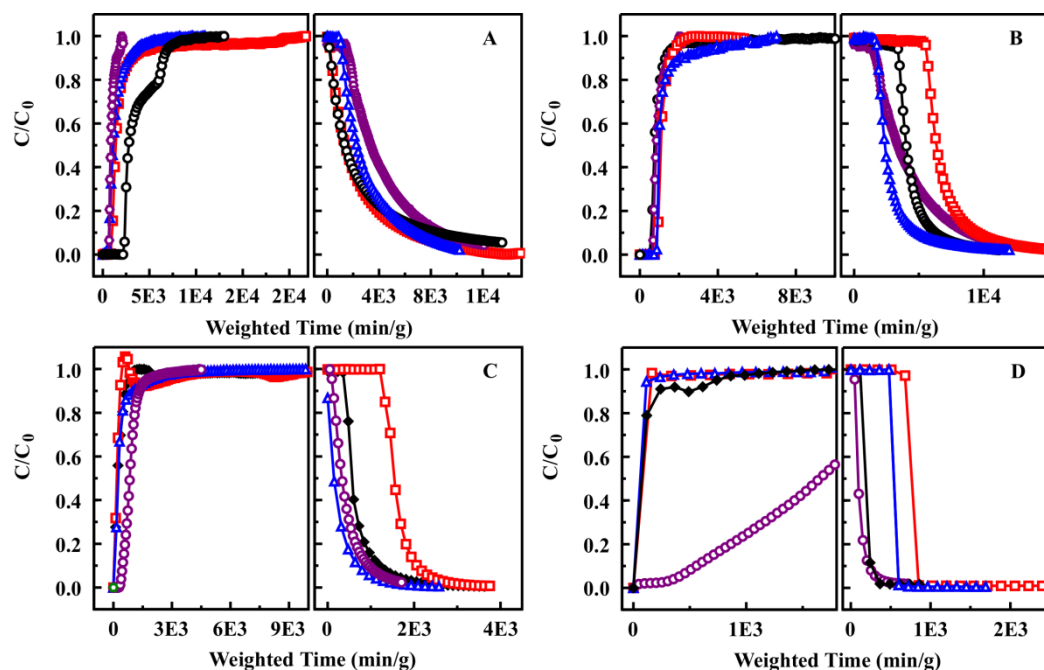


Fig. 40 — Target capture by the materials with hydroxyl associated metals. Breakthrough curves for ammonia (A, dry; B, 80% RH) and cyanogen chloride (C, dry; D, 80% RH): Co (black), Cu (red), Mg (blue). The breakthrough for the BPL/Zn/TEDA is shown in purple.

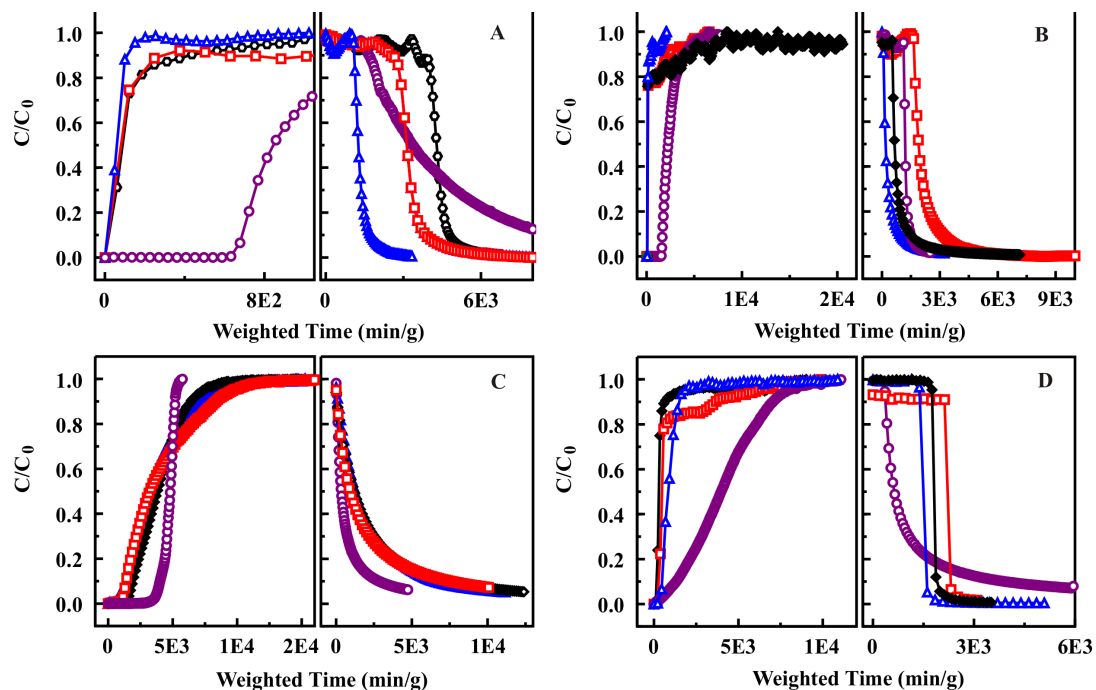


Fig. 41 — Target capture by the materials with hydroxyl associated metals. Breakthrough curves for sulfur dioxide (A, dry; B, 80% RH) and octane (C, dry; D, 80% RH): Co (black), Cu (red), Mg (blue). The breakthrough for the BPL/Zn/TEDA is shown in purple.

Table 12 — Calculated Octane Loading Capacities for Metal Reflux Materials*

		Octane		
		Mass	Sat. Load	Post-Purge
Sample	RH	mg	mol/kg	mol/kg
BPL/Zn/TEDA	0/0	29.3	3.3	2.7
	80/80	18.1	2.9	2.2
E50	0/0	6.0	1.6	0.5
	80/80	2.8	1.0	0.8
Co E50	0/0	8.6	2.9	1.0
	80/80	9.1	0.3	0.2
Cu E50	0/0	7.4	2.9	1.3
	80/80	5.5	0.8	0.0
Mg E50	0/0	10.2	2.8	1.0
	80/80	4.6	0.6	0.5

* Capacity values are calculated to sorbent saturation (Sat. Load) and after purging the column with air (Post-Purge).

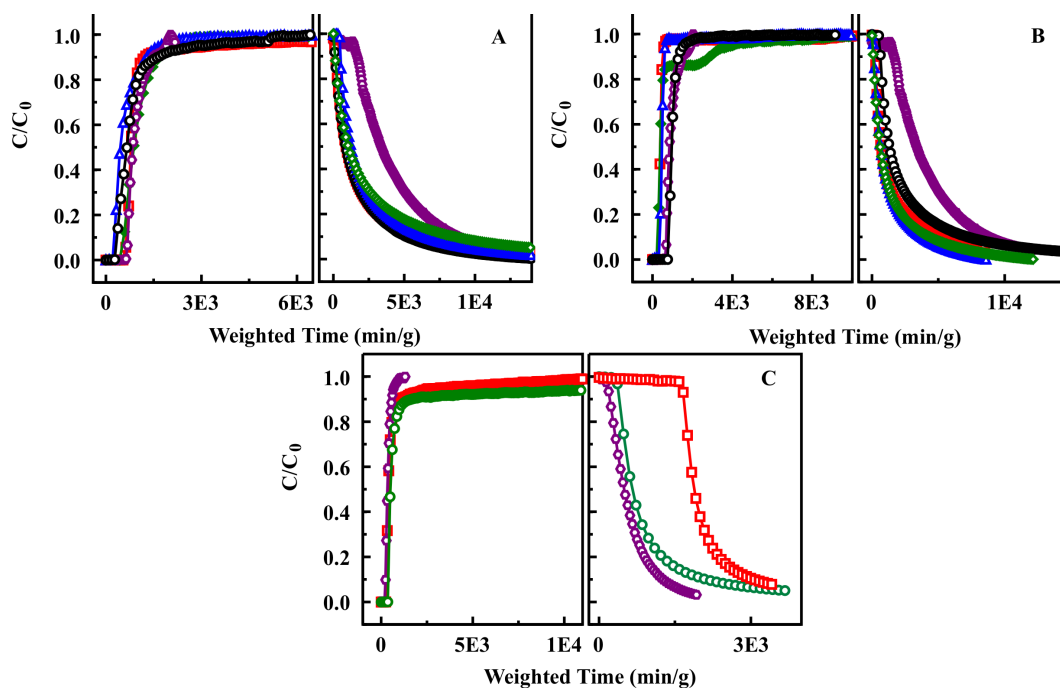


Fig. 42 — Ammonia capture by the EDA and AEA materials. Copper materials (A, dry): Cu EDA(3), black; Cu EDA (4), blue; Cu AEA(3), red; Cu AEA(4), green. Cu EDA(4). Zinc materials (B, dry; C 80% RH): Zn EDA(2), black; Zn EDA(4), blue; Zn AEA(2), red; Zn AEA(4), green. The breakthrough for the BPL/Zn/TEDA is shown in purple.

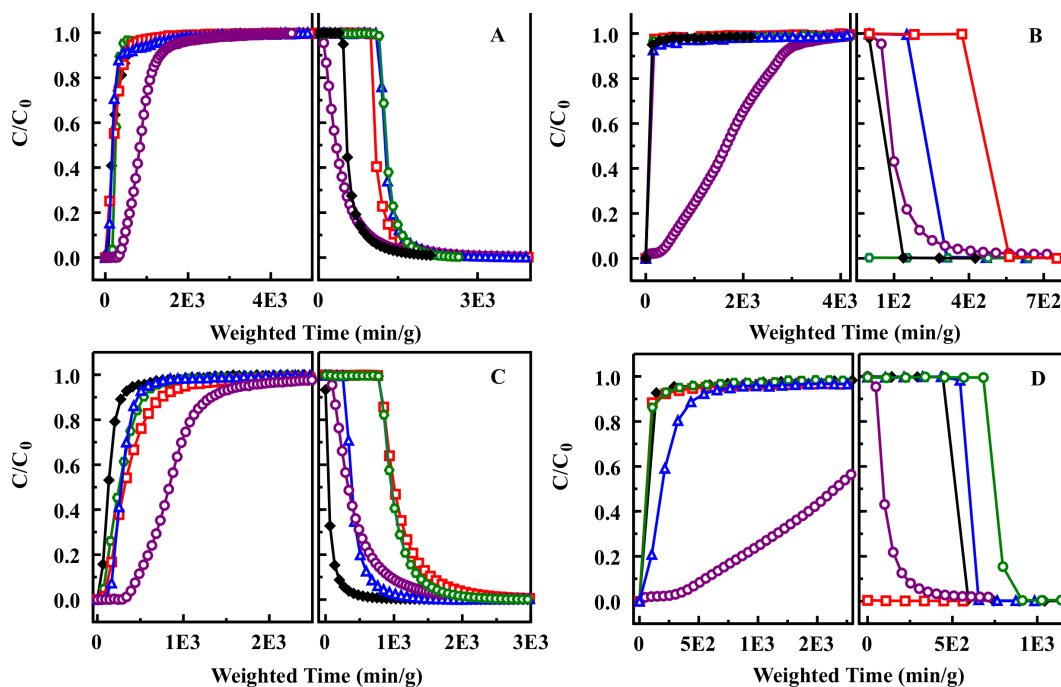


Fig. 43 — Cyanogen chloride capture by the EDA and AEA materials. Copper materials (A, dry; B, 80% RH): Cu EDA(3), black; Cu EDA(4), blue; Cu AEA(3), red; Cu AEA(4), green. Cu EDA(4). Zinc materials (C, dry; D 80% RH): Zn EDA(2), black; Zn EDA(4), blue; Zn AEA(2), red; Zn AEA(4), green. The breakthrough for the BPL/Zn/TEDA is shown in purple.

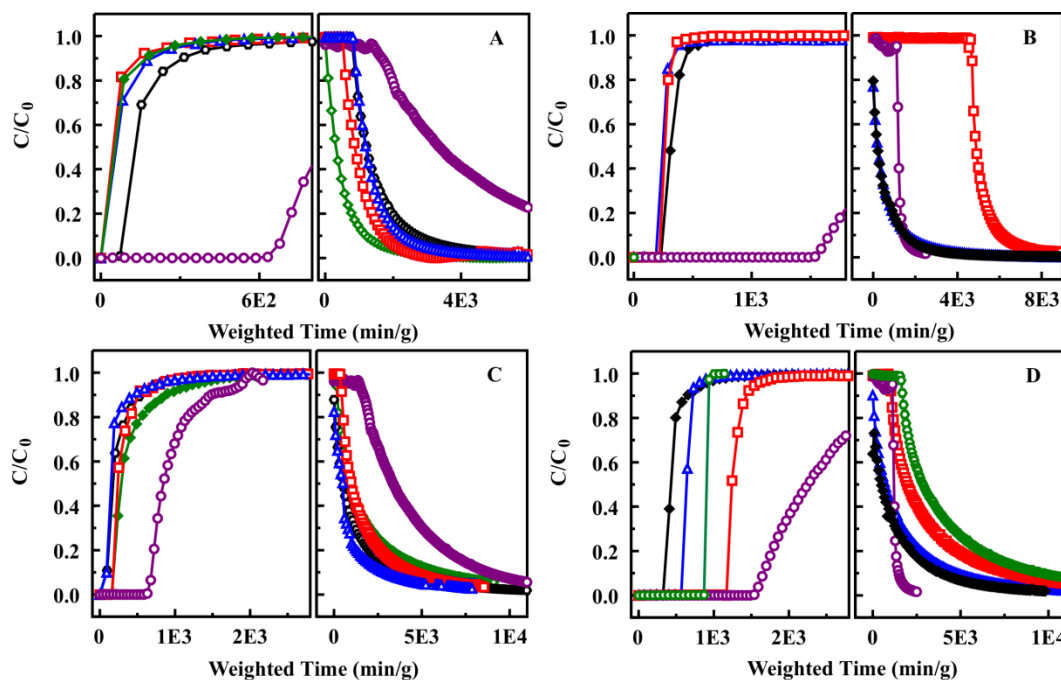


Fig. 44 — Sulfur dioxide capture by the EDA and AEA materials. Copper materials (A, dry; B, 80% RH): Cu EDA(3), black; Cu EDA(4), blue; Cu AEA(3), red; Cu AEA(4), green. Cu EDA(4). Zinc materials (C, dry; D 80% RH): Zn EDA(2), black; Zn EDA(4), blue; Zn AEA(2), red; Zn AEA(4), green. The breakthrough for the BPL/Zn/TEDA is shown in purple.

Physisorbed TEDA

Triethylenediamine (TEDA; 1,4-diazabicyclo[2.2.2]octane) is used as an additive in ASZM-TEDA sorbents to extend the functional lifetime of the materials. This additive interacts with light gases such as hydrogen cyanide, phosgene, and cyanogen chloride and appears to act as a source of OH⁻ during hydrolysis of the targets [61]. Here, ethane bridged (E50) and diethylbenzene bridged sorbents (MM3) were functionalized post-synthesis by adsorbing TEDA onto the material surfaces. TEDA (10% w/w sorbent) was physisorbed into the pore structure of the sorbent materials through incubation at 75 °C overnight on a rotisserie type mixer. The impact on performance of the sorbents against the light gas targets was evaluated (Tables 13 and 14). The presence of TEDA in the MM3 sorbent resulted in increased cyanogen chloride removal but had little impact on capture or retention of the other targets (Figs. 45 and 46). Addition of TEDA to the E50 sorbent also resulted in increased cyanogen chloride removal with reductions in ammonia and octane retention.

Table 13 – Calculated Target Loading Capacities for TEDA Functionalized Sorbents* – Ammonia and Cyanogen Chloride

		Ammonia			Cyanogen Chloride		
		Sorbent Mass	Sat. Loading	Post-Purge	Sorbent Mass	Sat. Loading	Post-Purge
Sample	RH	mg	mol/kg	mol/kg	mg	mol/kg	mol/kg
BPL/Zn/TEDA	0/0	20.6	0.7	0.4	21.8	1.2	0.7
	80/80	22.7	0.5	0.0	20.9	2.1	2.0
E50	0/0	6.6	4.0	1.9	8.6	0.5	0.1
	80/80	7.3	0.5	0.0	5.3	0.2	0.1
E50-TEDA	0/0	7.2	0.8	0.0	6.3	1.2	1.1
	80/80	10.5	1.2	0.0	9.5	2.7	2.6
MM3	0/0	5.7	1.3	0.4	5.4	0.4	0.4
	80/80	11.1	0.7	0.0	4.0	0.2	0.0
MM3-TEDA	0/0	10.0	0.6	0.1	4.8	0.9	0.8
	80/80	5.2	1.9	0.0	7.2	0.6	0.5

* Capacity values are calculated to sorbent saturation (Sat. Loading) and after purging the column with air (Post-Purge).

Table 14 – Calculated Target Loading Capacities for TEDA Functionalized Sorbents* – Sulfur Dioxide, Octane, and Chlorine

		Sulfur Dioxide			Octane			Chlorine		
		Mass	Sat. Load	Post-Purge	Mass	Sat. Load	Post-Purge	Mass	Sat. Load	Post-Purge
Sample	RH	mg	mol/kg	mol/kg	mg	mol/kg	mol/kg	mg	mol/kg	mol/kg
BPL/Zn/TEDA	0/0	23.6	0.3	0.0	29.3	3.3	2.7	--	--	--
	80/80	20.1	0.8	0.5	18.1	2.9	2.2	--	--	--
E50	0/0	7.8	0.1	0.0	6.9	3.8	1.8	7.0	0.1	0.1
	80/80	5.9	0.1	0.0	8.5	0.4	0.3	--	--	--
E50-TEDA	0/0	8.8	0.3	0.0	6.9	1.8	0.7	9.6	0.5	0.4
	80/80	9.4	0.2	0.0	10.4	0.6	0.0	--	--	--
MM3	0/0	6.9	0.1	0.0	4.3	1.2	0.6	--	--	--
	80/80	6.0	0.1	0.0	5.3	2.0	0.2	--	--	--
MM3-TEDA	0/0	5.0	0.2	0.0	6.9	0.9	0.4	--	--	--
	80/80	7.1	0.2	0.0	8.4	0.7	0.4	--	--	--

* Capacity values are calculated to sorbent saturation (Sat. Loading) and after purging the column with air (Post-Purge).

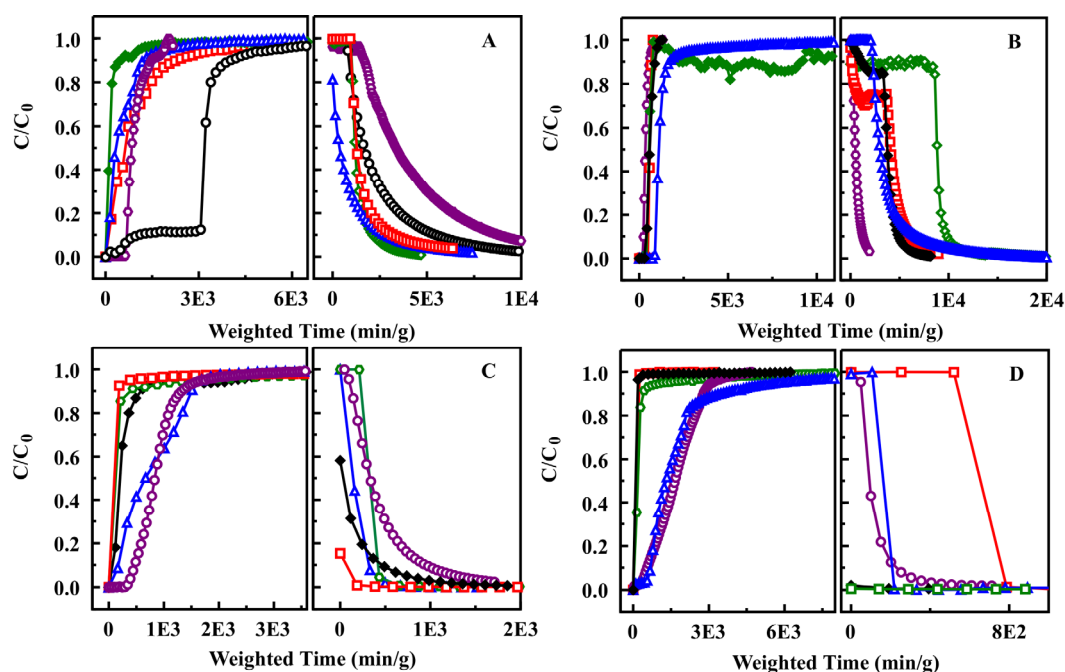


Fig. 45 — Target capture by the TEDA functionalized sorbents. Ammonia (A, dry; B, 80% RH) and cyanogen chloride (C, dry; D, 80% RH): E50 (black), E50-TEDA (blue), MM3 (red), MM3-TEDA (green). The breakthrough for the BPL/Zn/TEDA is shown in purple.

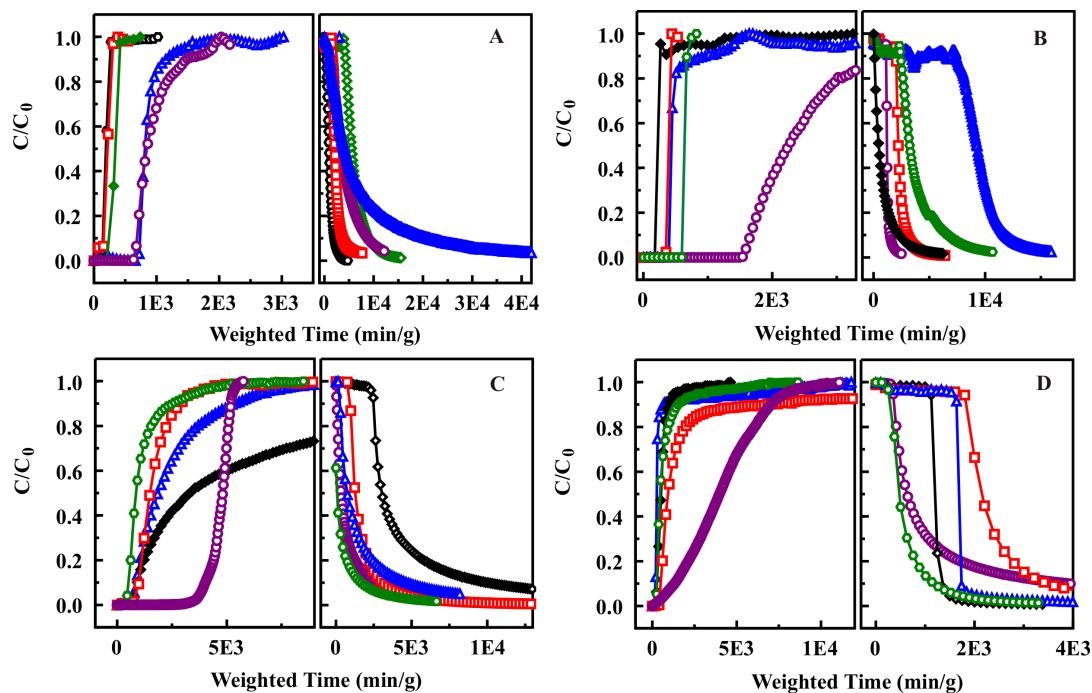


Fig. 46 — Target capture by the TEDA functionalized sorbents. Sulfur dioxide (A, dry; B, 80% RH) and octane (C, dry; D, 80% RH): E50 (black), E50-TEDA (blue), MM3 (red), MM3-TEDA (green). The breakthrough for the BPL/Zn/TEDA is shown in purple.

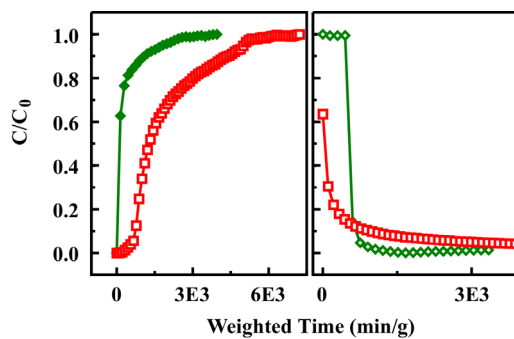


Fig. 47 — Chlorine breakthrough for organosilicates under dry conditions. E50 as synthesized (green) and E50-TEDA (red) materials.

Other Functionalizations

Two additional types of materials were synthesized for reactive capture of targets. ADC-10 focused on incorporation of carbonyls for reactive removal of ammonia. CAR-40 focused on incorporation of reactive chemistries directed at removal of formaldehyde. These materials have not been evaluated in microbreakthrough experiments.

ADC-10

The enolate anion form of carbonyl compounds with hydrogen atoms in the α position can react readily with formaldehyde. While carbonyl compounds are at equilibrium, the keto- form typically dominates making the reaction with formaldehyde unfavorable. The presence of a base can result in abstraction of α proton forming an enolate anion. Dicarboxyls such as diketones or keto esters have more acidic α protons allowing for use of a weak base in this process. The driving force behind the presence of the enolate anion is a base of sufficient strength for α -proton abstraction. Under ambient conditions on a solid surface, additional considerations arise. The pK_a of the proton to be abstracted from the keto form must be less than that of water, and the base must be stable on the surface. Incorporation of dicarbonyls into a porous material could be accomplished using a polymer with the dicarbonyl groups extending from the backbone. The sorbent itself might be engineered to act as the base for α proton abstraction.

The material designed in an attempt to use this approach was ADC-10. The base material was synthesized using a Pluronic P123 preparation method in acidic media [17,37]. Briefly, Pluronic P123 (4.0 g) and TMB (0.91 g) were dissolved in 0.1 M HNO_3 (12.02 g) with stirring at $\sim 60^\circ C$. The solution was allowed to cool to room temperature and silane precursor (5.15 g TMOS) was added drop-wise. The reaction mixture was stirred until homogeneous and then sealed tightly and heated at $60^\circ C$ overnight. The solution was unsealed and heated at $60^\circ C$ for 2 d. The product was then calcined with an increasing temperature from $25^\circ C$ to $650^\circ C$ by $1^\circ C$ per min after which it was soaked at $650^\circ C$ for 5 h. The base sorbent (1 g; $469\text{ m}^2/\text{g}$; $0.45\text{ cm}^3/\text{g}$; 40 \AA) was refluxed with APS (1 mL) in 250 mL toluene overnight to functionalize with pendant amine groups. 1,3-Acetonedicarboxylic acid (ACA) was then attached to this surface using EDC chemistry. The amine functionalized sorbent (1 g) was incubated with 2 g ACA and 21 mg EDC in 100 mM MES buffer (50 mL) on a rotisserie mixer overnight. The sorbent was then rinsed with ethanol and water and dried at $110^\circ C$ overnight. The fully functionalized sorbent had a BET surface area of $310\text{ m}^2/\text{g}$, pore volume $0.56\text{ cm}^3/\text{g}$, and pore size 75 \AA (Fig. 48). A variant of this sorbent was also prepared using SBA-15 as the base material.

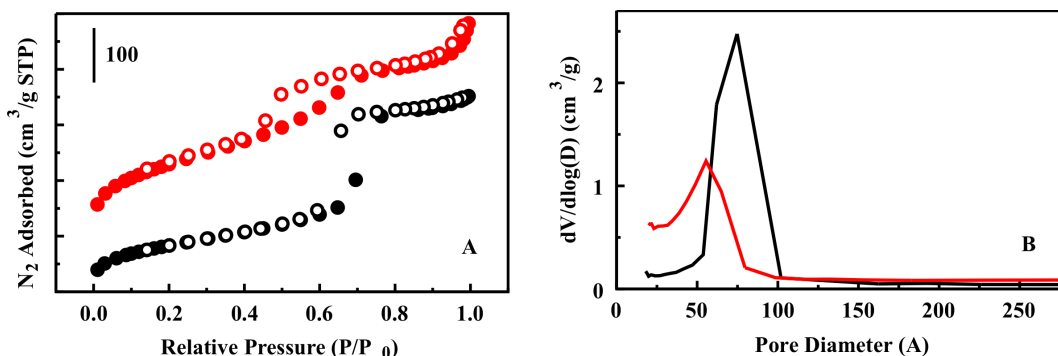


Fig. 48 — Material characteristics for ADC-10 (black) and CAR-40 (red). (A) Nitrogen sorption isotherms: CAR-40 offset by 100. (B) Pore size distributions for the materials.

CAR-40

Nucleophilic carbonyl chemistry is driven by the ability of the group located β to the carbonyl to leave upon attack by a nucleophile, in the case of this effort, ammonia (a weak base). This leaving group should have a pK_a less than that of ammonia in order for the reaction to proceed. When designing a sorbent, it is also necessary to consider the reactivity of other species such as water. Based on the relevant

pKa considerations, an ester would provide a favorable leaving group for the reaction of ammonia while not reacting with water in the air. The choice of isopropyl esters, offering an alkoxy group whose conjugate acid is that at least 10 times more basic than water, provides a good option.

The material designed in an attempt to use this approach was CAR-40. The base material was synthesized using a Pluronic P123 preparation method in acidic media [17,37]. Briefly, Pluronic P123 (1.0 g) was dissolved in 1.9 M HCl (31.25 g) with stirring at $\sim 40^\circ\text{C}$. The silane precursors, a mixture of CES (2.86 g) and TEOS (1.29 g) were then added drop-wise. The reaction mixture was stirred at 40°C for 24 h and then sealed for incubation at 100°C for 24 h. The product was refluxed in 2M HCl to remove the surfactant, rinsed, and dried at 80°C . At this point, the sorbent had a BET surface area of $633\text{ m}^2/\text{g}$, pore volume $0.94\text{ cm}^3/\text{g}$, and pore size 55 \AA . Final functionalization of the sorbent was completed by refluxing the base sorbent (0.6 g) with zinc acetate (0.5 g) in 2-propanol for 24 h. The fully functionalized sorbent had a BET surface area of $487\text{ m}^2/\text{g}$, pore volume $0.53\text{ cm}^3/\text{g}$, and pore size 55 \AA (Fig. 48). Variants of this sorbent were also prepared using differing ratios of CES to TEOS: CAR-30 = 2.15 g CES and 1.50 g TEOS; CAR-50 = 3.57 g CES and 1.07 g TEOS.

Scale-up and Relevant Formats

In order for the materials developed here to be applied in air purification applications, relevant formats must be developed and generation of sorbents in larger quantities is necessary. The protocols described in the above sections were originally developed for synthesis of batches on the scale of hundreds of milligrams. The work described used considerably more sorbent than that of previous studies, so the processes were scaled to deliver larger quantities on the order of 1 to 3 grams. This scaling process required little in the way of synthetic variation. Larger vessels were used; longer times were required for equilibration of temperatures; and addition of precursors in a dropwise manner was necessary. No edge effects were observed to impact the process. Similarly, it is possible to scale the processes from grams to tens of grams through the use of larger vessels and increased materials volumes. Single batches of E50 have been synthesized to produce 12 grams of sorbent. This batch size reaches the limit of the vessel sizes available in the laboratory setting due to the need for temperature maintenance and continual stirring. The single noted caution when scaling to increasingly large batches is that attention should be given to the surface-volume ratio for the stirring solution. Dropwise addition of precursor to the large batches requires significantly more time allowing for evaporation of the water and alcohols used. Simple precautions, such as partial coverage of the surface, address this difference.

Fabrics and Thin Films

The first possible path for generating application relevant formats involves using materials of this type as a surface coating. The advantage here is that all reactive components will be at or near the surface with little or no diffusional limitations. The total surface area available, however, is limited. Coatings of the materials were developed for use on both solid (glass) and fabric type (nylon, cellulose, and cellulose blends) supports. Thin films were generated through dipcoating of the support materials. Modification of the synthetic protocols provided above was necessary to provide porous materials with accessible surface area. The first change made was to the surfactant used. Pluronic P123 has a molecular weight of $\sim 5,800$ while that of Pluronic F127 is $\sim 12,500$. A change the surfactant requires adjustments to the remaining components of the sol mixture.

Thin films containing a mixture of DEB and BTE bridging groups were synthesized as follows: Pluronic F127 (3.5 g) was dissolved in methanol (6 g) with BTE and DEB at room temperature with magnetic stirring in a closed vessel. For a 50/50 sorbent, 2.62 g BTE and 1.56 g DEB were used. For a 70/30 sorbent, 1.87 g BTE and 2.59 g DEB were used. To this mixture, 0.05 M HCl (1.5 g) was added. The resulting solution was stirred overnight and could be stored for many days prior to use. For sorbents

comprised of 100% BTE groups, Pluronic P123 (1.9 g) was dissolved in methanol (2.0 g) with mesitylene (0.5 g) and BTE (2.12 g). When glass slides were used as substrates, they were first cleaned using piranha solution followed by thorough rinsing and drying. The thickness of the films was controlled through adjustment of the speed of dip or spin casting. Dipcoating for the materials described here was completed at a rate of 269 mm/min. Further thinning of the layer was achieved through dilution of the sol with additional methanol. After casting, the films were covered and heated at 60 °C for 24 h followed by curing at 80° to 120 °C for 24 h. A higher curing temperature provided improved durability and adhesion. Extraction of the surfactant was accomplished by immersing the thin films in 1 M HCl at 65 °C for 48 h. The materials were then rinsed with ethanol and dried at 110 °C. Morphological characteristics were evaluated *in situ* on the glass slides. Comparison of the surface area and weight prior to and following functionalization indicates deposition of approximately 5 mg of the sorbent material offering a surface area of 267 m²/g (Fig. 49). Once synthesized, these materials were functionalized following the protocols outlined for monolithic sorbents described above (Fig. 50).

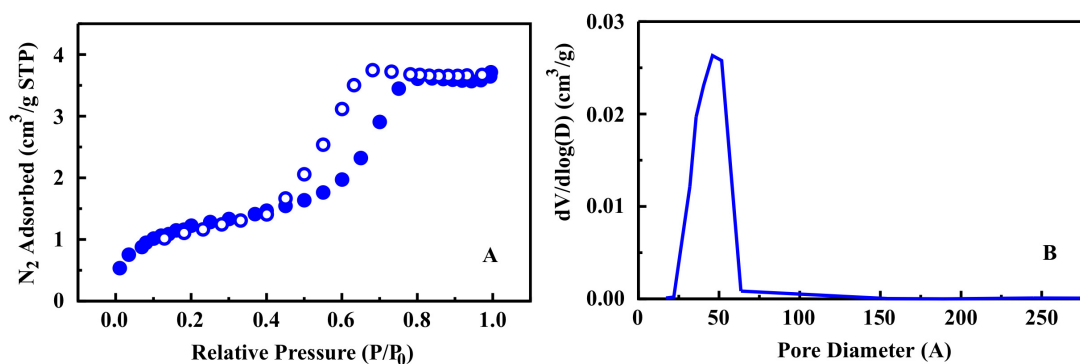


Fig. 49 — Material characteristics for thin film. (A) Nitrogen sorption isotherm collected *in situ* on glass slide. (B) Pore size distribution for the material.

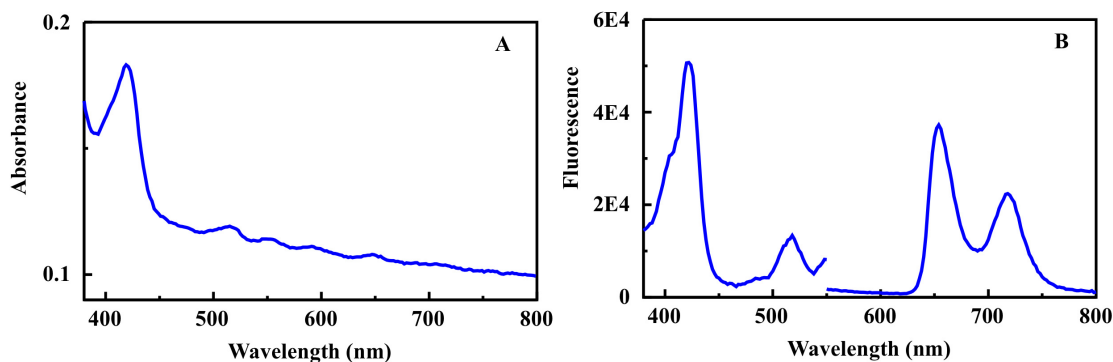


Fig. 50 — Absorbance (A) and fluorescence (B) characteristics for porphyrin functionalized thin film. These measurements are based on the average of 10 individual spots collected over four films.

Synthesis of films on fabrics was completed similarly to thin film generation; however, preparation of the fabric was required prior to dipcoating. To provide sites for binding of the sol during condensation, TEOS was deposited on the fabrics using a microwave-based process [62]. A solution was prepared by addition ammonium hydroxide (10 mL) to isopropanol (184 mL). To this solution, TEOS was added (3.6

mL). Fabric samples were submerged fully in this solution and then removed to a glass dish for microwave treatment (30 s; 1,200 W). The process was repeated three times. Following the final microwave treatment, samples were dried fully in the oven (110 °C). At this point, dipcoating could proceed as described for the glass slides. This procedure was completed on unbleached cotton as well as on representative military fabrics such as that of the standard Army combat uniform (ACU) and MultiCam. Morphological characteristics were evaluated *in situ* on the fabrics. Comparison of the surface area and weight prior to and following functionalization indicates a sorbent material offering a surface area of 365 m²/g (Fig. 51). Once synthesized, these materials were functionalized following the protocols outlined for monolithic sorbents described above. Both fluorescence and target capture characteristics were as expected based on the performance of the monolithic materials (Fig. 52).

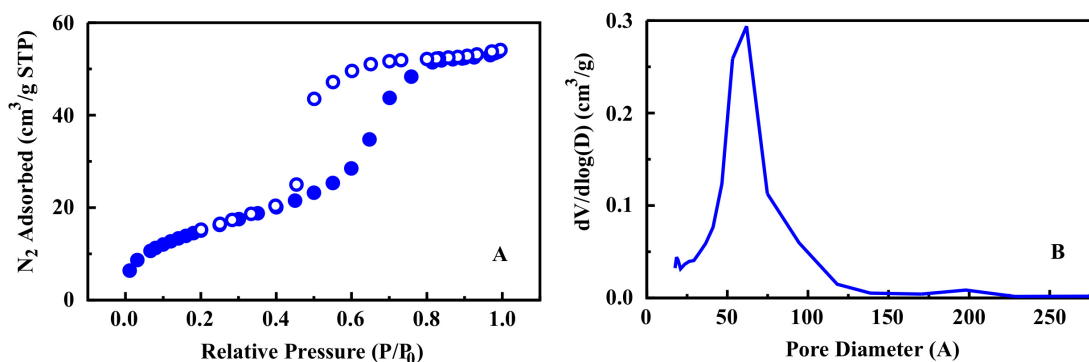


Fig. 51 — Material characteristics for coated fabric. (A) Nitrogen sorption isotherm collected *in situ* on cotton fabric. (B) Pore size distribution for the material.

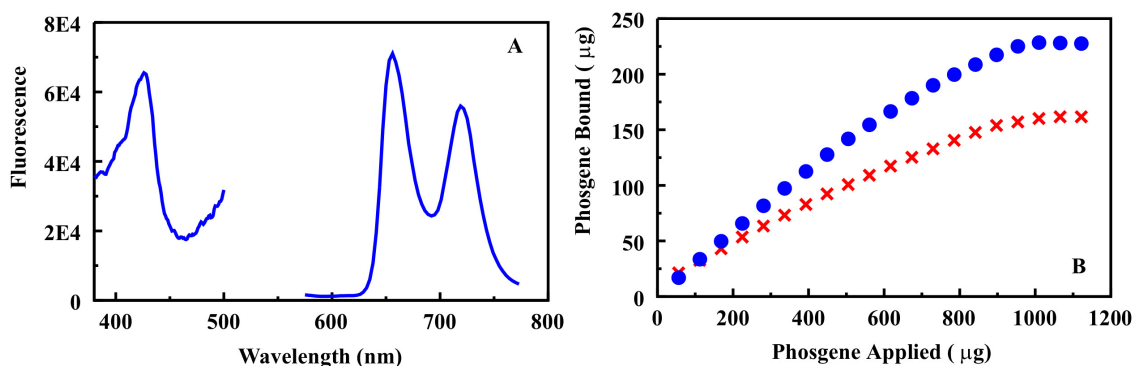


Fig. 52 — Performance of functionalized coated fabric samples. Fluorescence characteristics for porphyrin functionalized coating on cotton (A). Capture of phosgene by stacked layers (12) of the ACU fabric functionalized with CuDIX (B).

A Thermolyne incubator (Compact Series 5000) was modified to conduct water vapor transport studies based on guidance provided by the ASTM E 96 protocol [63]. Water vapor transport through a material is determined by measuring the rate of water loss through the material over a period of time. For our implementation, a scintillation vial (20 mL) was filled with 16.9 mL deionized water (± 0.1 mL) over which the sample material was sealed with parafilm (water 1.27 cm from sample surface). The sample

was weighed and placed in the incubator. Drierite was used to lower the humidity in the incubator and a dry nitrogen stream was flowed across the surface of the sample (250 sccm). Weight measurements were collected at 30 to 45 min intervals using an analytical balance. The temperature of the incubator was 25 °C (± 1 °C). This instrument was used to evaluate permeation of water through the various functionalized fabrics (Fig. 53). Permeation of water through coated and functionalized fabric samples was found to be similar to that of permeation through the unmodified fabrics.

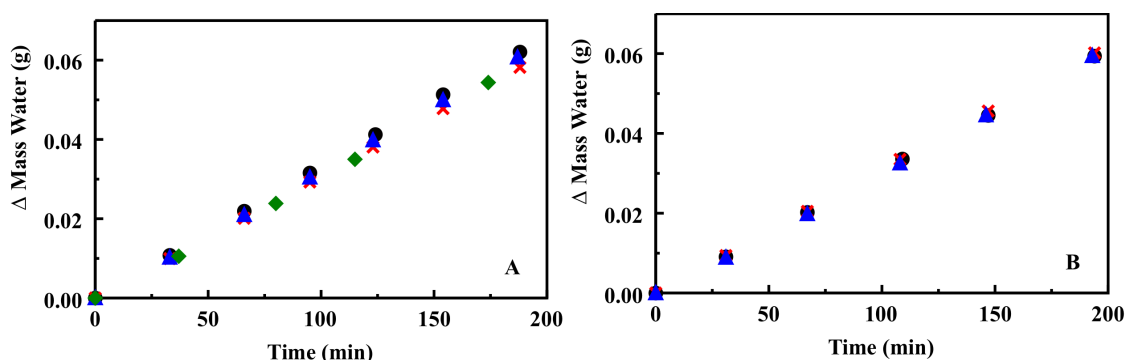


Fig. 53 — Water vapor permeation through functionalized fabrics. (A) Comparison of cotton only (black) to cotton coated with E50 (red), cotton coated with E50 and functionalized with CuDIX (green), and cotton coated with ED13 and functionalized with C₄TPP (blue). (B) Comparison of ACU (black) to ACU coated with ED13 (red) and ACU coated with ED13 and functionalized with C₄TPP (blue).

The apparatus for evaluation of target vapor permeation through fabric samples was based on the stations employed by the Chemical Technology Team (CTT) at Natick Soldier Research Development and Engineering Center (NSRDEC). A schematic is provided in Fig. 54. The temperature in the custom environmental chamber is controlled using a probe inside the chamber which adjusts an Air-Therm ATX heater (World Precision Instruments). Mass flow controllers, regulated by an inline Vaisala humidity probe, govern the ratio of humid to dry air entering the chamber. An Aerosol Vapor Liquid Assessment Group (AVLAG) test cell is used for these evaluations. These cells are stainless steel and hold the sample horizontally with O-ring seals (refer to TOP 8-2-501). The ALVAG cell is set up for single flow diffusive penetration testing using a single air or nitrogen stream (Fig. 54). The “headspace” above the swatch is stagnant, and the differential pressure above and below the swatch is zero. A sample (2.54×2.54 cm) is sandwiched between two supports with 0.64 cm^2 circular openings. The sample assembly is placed in the AVLAG cell and equilibrated to the desired humidity for 2 h. Target is introduced by placing liquid drops on top of glass wool using a repeating dispenser. Glass wool is used to help increase the volatility of the simulant. Challenge is applied to the surface of the sample in the static region of the AVLAG cell; therefore, evaporation is not a significant consideration. A direct line from the permeation cell to a dedicated FID (SRI model 110) allows for continuous monitoring of target concentrations (1,000 min). The FID uses Peak Simple, six-channel data acquisition software (SRI) for signal capture and peak integration. Excess flow from the direct line (above 50 mL/min) is filtered through a carbon scrubber.

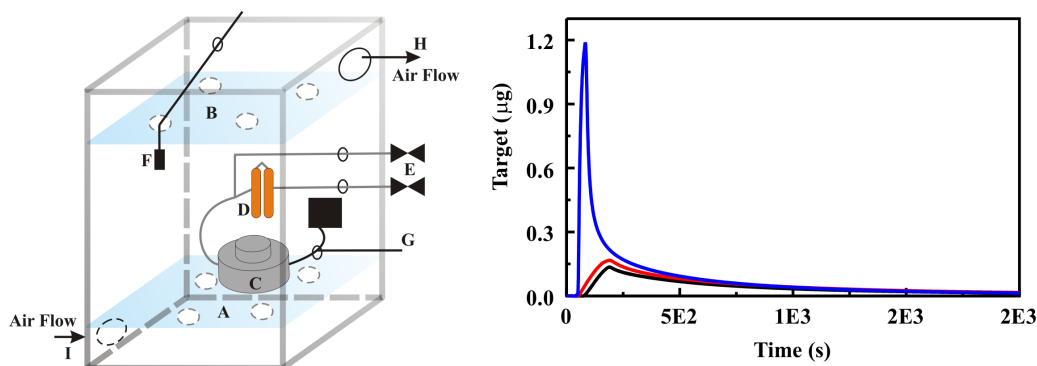


Fig. 54 — Schematic of the vapor permeation chamber and apparatus: (A and B) shelves, (C) AVLAG test cell, (D) water bubblers for humidity, (E) mass flow controllers for adjustment of sample humidity levels, (F) temperature probe, (G) line out to FID, (H and I) heated air in and out ports for temperature control. The graph shows permeation of CEES through cotton (blue), E50 coated cotton (red), and E50 coated cotton functionalized with CuDIX (black).

Fabric samples were evaluated using the permeation system with 2-chloroethyl ethyl sulfide (half-mustard; CEES) as the target (Fig. 54). The peak CEES concentration observed through the cotton fabric was $1.19 \mu\text{g/s}$ with $214 \mu\text{g}$ of target recovered in total. Under identical evaluation conditions, the peak CEES concentration through the E50 coated cotton was $0.17 \mu\text{g/s}$ with $78 \mu\text{g}$ total target recovered. When the coated surface was functionalized with CuDIX, the peak concentration was reduced to $0.14 \mu\text{g/s}$ with $61 \mu\text{g}$ total target recovered. This experiment was completed in the dark. Illumination of the fabric would be expected to produce additional target removal by the porphyrin functionalized material.

Pellets

A supported bed of sorbent material can also be used for air filtration applications. This is the type of format used for carbon based mask filters. Often, generation of pellets as fill for this type of filter requires the use of binders to provide structural stability. Two approaches were considered for generation of sorbents of the materials under this study. First, sorbent materials were generated as monoliths (Fig. 55). Typical extraction processes include crushing this material into a fine powder; however, Soxhlet extraction can be used without the need for crushing. These monoliths may provide sufficient structural character for use in filtration applications. Unfortunately, extraction is much more time consuming (5 days vs 1.5) and further functionalization of these structures is impeded by diffusion considerations; liquid diffusion is significantly hindered.



Fig. 55 — Photographs of 50% DEB monolith as-synthesized (top) and following Soxhlet extraction with 1 M HCl in ethanol for 5 days (bottom)

The second approach was to press pellets of the sorbent following final functionalization. An Imperial 2000 hydraulic press was used to apply pressures ranging from 0.5 to 9 metric ton. The time that samples were held under pressure was also varied from 10 min to 1 h; no differences were observed. Samples developed using pressures of less than 4.5 metric ton were found to be fragile and often broke apart with any amount of handling. At 6 metric ton, pellets were significantly more stable and resisted agitation in a glass vial. Table 15 and Fig. 56 present the morphological characteristics for sorbents subjected to varied pressures. Results were verified using an additional sorbent for which a 1.5 g of pressed pellets were generated.

Table 15 – Morphological Characteristics for Sorbent Materials Pressed into Pellets

Material	Pressure (metric ton)	Surface area (m ² /g)	Pore volume (cm ³ /g)	Pore Diameter (Å)
MM9	0.0	404	0.45	50
	3.0	412	0.434	48
	4.5	259	0.276	48
	5.0	398	0.426	48
	5.5	371	0.391	48
	6.0	382	0.412	47
	7.0	302	0.313	48
	8.0	317	0.327	48
	9.0	269	0.267	48
	10.0	260	0.257	48
MM12*	0.0	423	0.46	50
	9.0	310	0.39	48

*based on average of eight measurements for the 1.5 g batch

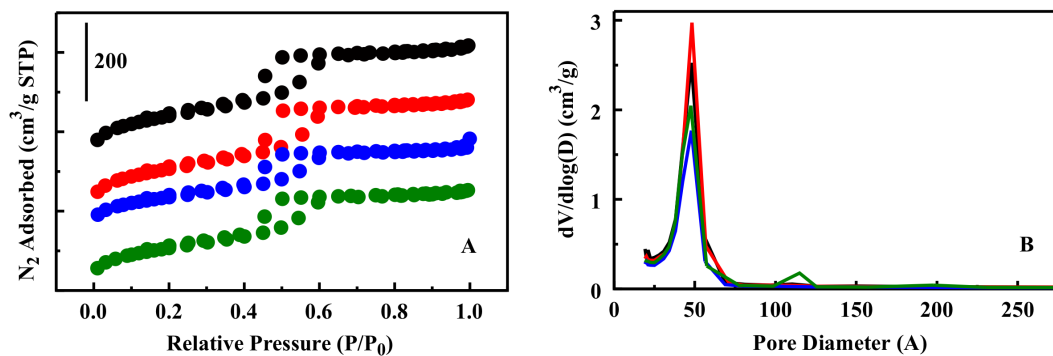


Fig. 56 — Material characteristics for pressed pellets. (A) Nitrogen sorption isotherms for pellets pressed at 3.0 (black), 5.0 (red), 7.0 (blue), and 9.0 (green) metric ton. (B) Pore size distribution for the materials; colored as in (A).

CONCLUSIONS

The studies presented here demonstrate the potential of organosilicate sorbents in gas target capture and the impact of functionalization on sorbent performance. The sorbents developed cover a wide range of functionalities offering a number of potential interactions with targets of interest. We have shown that it is possible to significantly alter interactions between irritant gases and the sorbents through modification of the surface chemistry both during synthesis and through post-synthesis grafting. The data also illustrates the complexity related to design of an air purification sorbent. While the altered surface chemistry had an impact on performance, the porosity characteristics and available surface area in the materials also affected the binding capacity. The materials developed offer an organized and interconnected pore network allowing access to all of the functional surface area. This is in stark contrast to carbon materials, which tend to have slit-shaped pores with little organization. While the macroporous texture of the materials studied here reduces the need for ordered porosity in providing access to the available pore volume, it does not address the presence of narrowed regions in the pores (bottle necks). The materials also offer flexibility in their application with simple approaches to production scale-up and adaptability for use as a supported bed or as a surface coating.

ACKNOWLEDGMENTS

Bryan J. Schindler (SAIC) and Paulette Jones (SAIC) provided evaluation of microbreakthrough performance. Iwona A. Leska (NOVA Research, Inc) provided HPLC and UV/vis analysis. Jenna R. Taft (formerly NOVA Research, Inc.) contributed to materials synthesis and morphological characterization. Martin Moore (NRL, Code 6930) was responsible for fabric permeation studies. Ross Russell was a student at NRL supported through NREIP during the summers of 2011 and 2012. His efforts focused on fabrics and thin films. Michael A. Dinderman (formerly NRL, Code 6930) provided SEM/TEM analysis. Jeffrey R. Deschamps (NRL, Code 6930) and Syed B. Qadri (NRL, Code 6366) provided assistance with X-ray diffraction measurements. Jared DeCoste (SAIC) provided insight into carbonyl chemistries. This research was sponsored by the Defense Threat Reduction Agency (DTRA, BA08PRO015). The views expressed here are those of the authors and do not represent those of the U.S. Navy, the U.S. Department of Defense, or the U.S. Government.

REFERENCES

1. TIC/TIM Task Force, *Toxic Industrial Chemical / Toxic Industrial Material Task Force Prioritization & Application Recommendations*; Joint Program Executive Office for Chemical and Biological Defense (JPEO-CBD): Memorandum for Record #1, 2009.
2. C.T. Carey, *U.S. Chemical and Biological Defense Respirators: An Illustrated History* (Schiffer Publishing, Ltd, Atglen, PA, 1998).
3. S. Bashkova and T.J. Bandosz, "Adsorption/reduction of NO₂ on Graphite Oxide/Iron Composites," *Ind. Eng. Chem. Res.* **48**(24), 10884-10891 (2009).
4. M. Seredych, S. Bashkova, R. Pietrzak, and T.J. Bandosz, "Interactions of NO₂ and NO with Carbonaceous Adsorbents Containing Silver Nanoparticles," *Langmuir* **26**(12), 9457-9464 (2010).
5. T.G. Glover, G.W. Peterson, B.J. Schindler, D. Britt, and O.Yaghi, "MOF-74 Building Unit Has a Direct Impact on Toxic Gas Adsorption," *Chem. Eng. Sci.* **66**(2), 163-170 (2011).

6. Y.S. Bae, A.M. Spokoyny, O.K. Farha, R.Q. Snurr, J.T. Hupp, and C.A. Mirkin, "Separation of Gas Mixtures Using Co(II) Carborane-Based Porous Coordination Polymers," *Chem. Commun.* **46**(20), 3478-3480 (2010).
7. B. Mu, P.M. Schoenecker, and K.S. Walton, "Gas Adsorption Study on Mesoporous Metal-Organic Framework UMCM-1," *J. Phys. Chem. C* **114**(14), 6464-6471 (2010).
8. K.L. Mulfort, O.K. Farha, C.D. Malliakas, M.G. Kanatzidis, and J.T. Hupp, "An Interpenetrated Framework Material with Hysteretic CO₂ Uptake," *Chem-Eur. J.* **16**, 276-281 (2010).
9. A.O. Yazaydin, R.Q. Snurr, T.H. Park, K. Koh, J. Liu, M.D. LeVan, A.I. Benin, P. Jakubczak, M. Lanuza, D.B. Galloway, J.J. Low, and R.R. Willis, "Screening of Metal-Organic Frameworks for Carbon Dioxide Capture from Flue Gas Using a Combined Experimental and Modeling Approach," *J. Am. Chem. Soc.* **131**(51), 18198-18199 (2009).
10. F. Hoffmann, M. Cornelius, J. Morell, and M. Fröba, "Silica-based Mesoporous Organic-Inorganic Hybrid Materials," *Angew Chem. Int. Edit.* **45**(20), 3216-3251 (2006).
11. J. Weitkamp, M. Hunger, and U. Ryma, "Base Catalysis on Microporous and Mesoporous Materials: Recent Progress and Perspectives," *Micropor. Mesopor. Mat.* **48**(1-3), 255-270 (2001).
12. B.J. Melde, B.J. Johnson, and P.T. Charles, "Mesoporous Silicate Materials in Sensing," *Sensors* **8**(8), 5202-5228 (2008).
13. S. Inagaki, S. Guan, Y. Fukushima, T. Ohsuna, and O. Terasaki, "Novel Mesoporous Materials with a Uniform Distribution of Organic Groups and Inorganic Oxide in their Frameworks," *J. Am. Chem. Soc.* **121**(41), 9611-9614 (1999).
14. C. Yohsina-Ishii, T. Asefa, N. Coombs, M.J. MacLachlan, and G.A. Ozin, "Periodic Mesoporous Organosilicas, PMOs: Fusion of Organic and Inorganic Chemistry 'Inside' the Channel Walls of Hexagonal Mesoporous Silica," *Chem. Commun.* **24**, 2539-2540 (1999).
15. F. Hoffmann, M. Cornelius, J. Morell, and M. Froba, "Periodic Mesoporous Organosilicas (PMOs): Past, Present, and Future," *J. Nanosci. Nanotech.* **6**(2), 265-288 (2006).
16. D. Brandhuber, H. Peterlik, and N. Huesing, "Facile Self-Assembly Processes to Phenylene-Bridged Silica Monoliths with Four Levels of Hierarchy," *Small* **2**(4), 503-506 (2006).
17. B.J. Melde, B.J. Johnson, M.A. Dinderman, and J.R. Deschamps, "Macroporous Periodic Mesoporous Organosilicas with Diethylbenzene Bridging Groups," *Micropor. Mesopor. Mat.* **130**(1-3), 180-188 (2010).
18. K. Nakanishi, "Pore Structure Control Of Silica Gels Based On Phase Separation," *J Porous Mater.* **4**(2), 67-112 (1997).
19. A. Palaniappan, S. Moochhala, F.E.H. Tay, X. Su, and N.C.L. Phua, "Phthalocyanine/silica Hybrid Films on QCM for Enhanced Nitric Oxide Sensing," *Sensor. Actuat. B-Chem.* **129**(1), 184-187 (2008).
20. A. Palaniappan, X.D. Su, and F.E.H. Tay, "Four-channel QCA Using Mesoporous Silica Films for Gas Sensing Applications," *IEEE Sens. J.* **6**(6), 1676-1682 (2006).

21. A. Palaniappan, X. Li, F.E.H. Tay, J. Li, and X. Su, "Cyclodextrin Functionalized Mesoporous Silica Films on Quartz Crystal Microbalance for Enhanced Gas Sensing," *Sensor. Actuat. B-Chem.* **119**(1), 220-226 (2006).
22. A. Palaniappan, X. Su, and F.E.H. Tay, "Functionalized Mesoporous Silica Films for Gas Sensing Applications," *J. Electroceram.* **16**(4), 503-505 (2006).
23. A. Palaniappan, S. Mookhala, F.E.H. Tay, N.C.L. Phua, and X. Su, "Selective and Enhanced Nitric Oxide Detection Using Hemoprotein/Silica Hybrids," *Sensor. Actuat. B-Chem.* **133**(1), 241-243 (2008).
24. S. Jansat, K. Pelzer, J. García-Antón, R. Raucoles, K. Philippot, A. Maisonnat, B. Chaudret, Y. Guari, A. Mehdi, C. Reyé, and R.J.P. Corriu., "Synthesis of New $\text{RuO}_2\text{-SiO}_2$ Composite Nanomaterials and their Application as Catalytic Filters for Selective Gas Detection," *Adv. Funct. Mater.* **17**(16), 3339-3347 (2007).
25. B. Yuliarto, Y. Kumai, S. Inagaki, and H. Zhou, "Enhanced Benzene Selectivity of Mesoporous Silica SPV Sensors by Incorporating Phenylene Groups in the Silica Framework," *Sensor. Actuat. B-Chem.* **138**(2), 417-421 (2009).
26. B.J. Johnson, B.J. Melde, P.T. Charles, D.C. Cardona, M.A. Dinderman, A.P. Malanoski, and S.B. Qadri, "Imprinted Nanoporous Organosilicas for Selective Adsorption of Nitroenergetic Targets," *Langmuir* **24**(16), 9024-9029 (2008).
27. B.J. Johnson, B.J. Melde, P.T. Charles, M.A. Dinderman, A.P. Malanoski, I.A. Leska, and S.A. Qadri, "Macroporous Silica for Concentration of Nitroenergetic Targets," *Talanta* **81**(4-6), 1454-1460 (2010).
28. B.J. Johnson, N.E. Anderson, P.T. Charles, A.P. Malanoski, B.J. Melde, M. Nasir, and J.R. Deschamps, "Porphyrin-embedded Silicate Materials for Detection of Hydrocarbon Solvents," *Sensors* **11**, 886-904 (2011), doi: 10.3390/s110100886.
29. B.J. Johnson, B.J. Melde, C. Thomas, A.P. Malanoski, I.A. Leska, P.T. Charles, D.A. Parrish, and J.R. Deschamps, "Fluorescent Silicate Materials for the Detection of Paraoxon," *Sensors* **10**, 2315-2331 (2010), doi:10.3390/s100302315.
30. M.A. Goldshtrakh, N.N. Kononov, S.G. Dorofeev, and A.A. Ischenko, "Gas Sensitivity of Etioporphyrin Metal Complexes in Thin Films," *J. Anal. Chem.* **64**(12), 1247-1251 (2009).
31. B. Wang, X. Zuo, Y.Q. Wu, Z.M. Chen, C.Y. He, and W.B. Duan, "Comparative Gas Sensing in Copper Porphyrin and Copper Phthalocyanine Spin-Coating Films," *Sensor. Actuat. B-Chem.* **152**(2), 191-195 (2011).
32. B.J. Johnson, G.W. Peterson, P. Jones, B.J. Melde, J.R. Taft, and B.J. Schindler, "Porphyrin-embedded Organosilicate Materials for Ammonia Adsorption," *J. Porphyr. Phthalocya.* **16**(12), 1-10 (2012).
33. H. Seki, K. Okada, Y. Iimura, and M. Hoshino, "Photochemical Reactions of Nitrocobalt(III) Tetraphenylporphyrin and its Pyridine Complex Studied by Laser Flash Photolysis," *J. Phys. Chem. A* **101**(44), 8174-8178 (1997).

34. S. Vilakazi and T. Nyokong, "Interaction of Nitric Oxide with Cobalt(II) Tetrasulfophthalocyanine," *Polyhedron* **19**(2), 229-234 (2000).
35. B. Johnson-White, M. Zeinali, K.M. Shaffer, C.H. Patterson, Jr., P.T. Charles, and M.A. Markowitz, "Detection of Organics Using Porphyrin Embedded Nanoporous Organosilicas," *Biosens. Bioelectron.* **22**(6), 1154-1162 (2007).
36. B.J. Johnson, I.A. Leska, B.J. Melde, and J.R. Taft, "Removal of Phosgene by Metalloporphyrin-Functionalized Porous Organosilicates," *Catal. Commun.* **27**, 105-108 (2012).
37. B.J. Johnson, B.J. Melde, G.W. Peterson, B.J. Schindler, and P. Jones, "Functionalized Organosilicate Materials for Irritant Gas Removal," *Chem. Eng. Sci.* **68**(1), 376-382 (2012).
38. K. Nakanishi, T. Amatani, S. Yano, and T. Kodaira, "Multiscale Templating of Siloxane Gels via Polymerization-Induced Phase Separation," *Chem. Mater.* **20**(3), 1108-1115 (2008).
39. K. Nakanishi, Y. Kobayashi, T. Amatani, K. Hirao, and T. Kodaira, "Spontaneous Formation of Hierarchical Macro-Mesoporous Ethane-Silica Monolith," *Chem. Mater.* **16**(19), 3652-3658 (2004).
40. G.W. Peterson, C.J. Karwacki, W.B. Feaver, and J.A. Rossin, "Zirconium Hydroxide as a Reactive Substrate for the Removal of Sulfur Dioxide," *Indust. & Engin. Chem. Res.* **48**(4), 1694-1698 (2009).
41. G.W. Peterson, G.W. Wagner, A. Balboa, J. Mahle, T. Sewell, and C.J. Karwacki, "Ammonia Vapor Removal by $\text{Cu}_3(\text{BTC})_2$ and its Characterization by MAS NMR," *J. Phys. Chem. C* **113**(31), 13906-13917 (2009).
42. W.S. Wu and V.S. Gaid, "Determination of Phosgene (Carbonyl Chloride) in Air by High-Performance Liquid Chromatography with a Dual Selective Detection System," *Analyst* **118**(10), 1285-1287 (1993).
43. B.J. Johnson, A.P. Malanoski, I.A. Leska, B.J. Melde, J.A. Taft, M.A. Dinderman, and J.R. Deschamps, "Adsorption of Organophosphates by Porous Organosilicates: Capillary Phase-Separation," *Micropor. Mesopor. Mat.*, submitted 2013.
44. B.J. Johnson, B.J. Melde, P.T. Charles, and A.P. Malanoski, "Porphyrin-embedded Organosilicas for Detection and Decontamination," SPIE Proceedings **7306**, 2009 SPIE International Defense, Security and Sensing Symposium, Orlando, FL, 2009.
45. B.J. Johnson, B.J. Melde, I.A. Leska, P.T. Charles, and A.D. Hewitt, "Solid-phase Extraction Using Hierarchical Organosilicates for Enhanced Detection of Nitroenergetic Targets," *J. Environ. Monitor* **13**(5), 1404-1409 (2011).
46. M. Kruk and M. Jaroniec, "Gas Adsorption Characterization of Ordered Organic-Inorganic Nanocomposite Materials," *Chem. Mater.* **13**(10), 3169-3183 (2001).
47. S. Raunier, T. Chiavassa, F. Marinelli, A. Allouche, and J.P. Aycard, "Reactivity of HNCO with NH_3 at Low Temperature Monitored by FTIR Spectroscopy: Formation of $\text{NH}_4^+\text{OCN}^-$," *Chem. Phys. Lett.* **368**(5-6), 594-600 (2003).

48. G.W. Peterson, G.W. Wagner, J.H. Keller, and J.A. Rossin, "Enhanced Cyanogen Chloride Removal by the Reactive Zirconium Hydroxide Substrate," *Ind. Eng. Chem. Res.* **49**(22), 11182-11187 (2010).
49. C. Sass and B.S. Ault, "Matrix Isolation Infrared Spectroscopic Study of Sulfur Dioxide-Amine Complexes," *J. Phys. Chem.* **88**(3), 432-440 (1984).
50. B.J. Johnson, I.A. Leska, B.J. Melde, and J.R. Taft, "Self-reporting Materials: Dual Use for Porphyrin-Embedded Sorbents," *Sensor Actuat. B-Chem.* **176**, 399-404 (2012).
51. T.J. Bandoz and C. Petit, "Mof/graphite oxide hybrid materials: Exploring the New Concept of Adsorbents and Catalysts," *Adsorption* **17**(1), 5-16 (2011).
52. T. Watanabe and D.S. Sholl, "Molecular Chemisorption on Open Metal Sites in Cu₃ (Benzenetricarboxylate)₂: A Spatially Periodic Density Functional Theory Study," *J. Chem. Phys.* **133**(9), (2010).
53. D. Britt, D. Tranchemontagne, and O.M. Yaghi, "Metal-Organic Frameworks with High Capacity and Selectivity for Harmful Gases," *Proceedings of the National Academy of Sciences of the United States of America* **105**(33), 11623-11627 (2008).
54. C. Petit and T.J. Bandoz, "Mof-graphite Oxide Composites: Combining the Uniqueness of Graphene Layers and Metal-Organic Frameworks," *Adv. Mat.* **21**(46), 4753-4757 (2009).
55. C. Petit and T.J. Bandoz, "Enhanced Adsorption of Ammonia on Metal-Organic Framework/Graphite Oxide Composites: Analysis of Surface Interactions," *Adv. Func. Mat.* **20**(1), 111-118 (2010).
56. G.W. Peterson, J.A. Rossin, C.J. Karwacki, and T.G. Glover, "Surface Chemistry and Morphology of Zirconia Polymorphs and the Influence on Sulfur Dioxide Removal," *J. Phys.Chem. C* **115**(19), 9644-9650 (2011).
57. L.F. Chen, X.L. Zhou, L.E. Norena, J.A. Wang, J. Navarrete, P. Salas, A. Montoya, P. Del Angel, and M.E. Llanos, "Comparative Studies of Zr-Based MCM-41 and MCM-48 Mesoporous Molecular Sieves: Synthesis and Physicochemical Properties," *Appl. Surf. Sci.* **253**(5), 2443-2451 (2006).
58. T. Amatani, K. Nakanishi, K. Hirao, and T. Kodaira, "Monolithic Periodic Mesoporous Silica with Well-Defined Macropores," *Chem. Mater.* **17**(8), 2114-2119 (2005).
59. M.C. Burleigh, S. Dai, E.W. Hagaman, and J.S. Lin, "Imprinted Polysilsesquioxanes for the Enhanced Recognition of Metal Ions," *Chem. Mater.* **13**(8), 2537-2546 (2001).
60. H.G. Zhu, D.J. Jones, J. Zajac, R. Dutartre, M. Rhomari, and J. Roziere, "Synthesis of Periodic Large Mesoporous Organosilicas and Functionalization by Incorporation of Ligands into the Framework Wall," *Chem. Mater.* **14**(12), 4886-4894 (2002).
61. J.J. Mahle, G.W. Peterson, B.J. Schindler, P.B. Smith, J.A. Rossin, and G.W. Wagner, "Role of Teda as an Activated Carbon Impregnant for the Removal of Cyanogen Chloride from Air Streams: Synergistic Effect with Cu(II)," *J. Phys. Chem. C* **114**(47), 20083-20090 (2010).

62. R.A. Hayn, J.R. Owens, S.A. Boyer, R.S. McDonald, and H.J. Lee, "Preparation of Highly Hydrophobic And Oleophobic Textile Surfaces Using Microwave-Promoted Silane Coupling," *J. Mat. Sci.* **46**(8), 2503-2509 (2011).
63. ASTM designation E 96 / E 96M - 05 Standard Test Methods for Water Vapor Transmission of Materials; <https://law.resource.org/pub/us/cfr/ibr/003/astm.e96.1995.pdf> (1996).